

REPORT DOCUMENTATION PAGE			Form Approved OMB No. 0704-0188		
Public reporting burden for this collection of information is estimated to average 1 hour per response, including the time for reviewing instructions, searching existing data sources, gathering and maintaining the data needed, and completing and reviewing this collection of information. Send comments regarding this burden estimate or any other aspect of this collection of information, including suggestions for reducing this burden to Department of Defense, Washington Headquarters Services, Directorate for Information Operations and Reports (0704-0188), 1215 Jefferson Davis Highway, Suite 1204, Arlington, VA 22202-4302. Respondents should be aware that notwithstanding any other provision of law, no person shall be subject to any penalty for failing to comply with a collection of information if it does not display a currently valid OMB control number. PLEASE DO NOT RETURN YOUR FORM TO THE ABOVE ADDRESS.					
1. REPORT DATE (DD-MM-YYYY) January 6, 2011		2. REPORT TYPE Final		3. DATES COVERED (From - To) 1 February 2008 to 30 November 2010	
4. TITLE AND SUBTITLE Unsteady Flow Structure on Low Aspect Ratio Wings		5a. CONTRACT NUMBER			
		5b. GRANT NUMBER FA9550-08-1-0022, P00002			
		5c. PROGRAM ELEMENT NUMBER			
6. AUTHOR(S) Donald Rockwell		5d. PROJECT NUMBER			
		5e. TASK NUMBER			
		5f. WORK UNIT NUMBER			
7. PERFORMING ORGANIZATION NAME(S) AND ADDRESS(ES) Professor Donald Rockwell Department of Mechanical Engineering and Mechanics 356 Packard Laboratory, 19 Memorial Drive West Lehigh University Bethlehem, PA 18015		8. PERFORMING ORGANIZATION REPORT NUMBER			
9. SPONSORING / MONITORING AGENCY NAME(S) AND ADDRESS(ES) Dr. Douglas Smith Air Force Office of Scientific Research 875 N Randolph St, Suite 325, Room 3112 Arlington, VA 22203		10. SPONSOR/MONITOR'S ACRONYM(S) AFOSR/NA			
		11. SPONSOR/MONITOR'S REPORT NUMBER(S) AFRL-OSR-VA-TR-2012-0045			
12. DISTRIBUTION / AVAILABILITY STATEMENT A					
13. SUPPLEMENTARY NOTES					
14. ABSTRACT The overall objective of this investigation was to determine the quantitative flow structure on low aspect ratio wings subjected to basic classes of maneuvers, in order to provide a basis for interpretation of induced forces. Techniques of particle image velocimetry were employed for critical planes of the flow field, and a technique of stereo particle image velocimetry was developed for water-based systems. Post-processing of the acquired images allowed determination of the vorticity and streamline topology, and construction of space-time volumes of the flow structure. These approaches led to characterization of the three-dimensional flow structure on flapping wings, as well as wings in rectilinear motion, and determination of patterns of spanwise- and streamwise-oriented vorticity. Passive control in the form of a sinusoidal leading-edge, which mimics the protuberances on the flipper of the humpback whale, and active open-loop control, in the form of small-amplitude perturbations of a wing can effectively can effectively manipulate the structure of the classes of flows investigated herein.					
15. SUBJECT TERMS Vortex, flow separation, unsteady aerodynamics					
16. SECURITY CLASSIFICATION OF:			17. LIMITATION OF ABSTRACT	18. NUMBER OF PAGES	
a. REPORT Approved for public release; distribution is unlimited	b. ABSTRACT Approved for public release; distribution is unlimited	c. THIS PAGE Approved for public release; distribution is unlimited			19a. NAME OF RESPONSIBLE PERSON Donald Rockwell
					19b. TELEPHONE NUMBER (include area code) 610-758-4641

UNSTEADY FLOW STRUCTURE ON LOW ASPECT RATIO WINGS

AFOSR GRANT FA9550-08-1-0022, P00002

1 February 2008 to 30 November 2010

Donald Rockwell

Department of Mechanical Engineering and Mechanics

356 Packard Laboratory, 19 Memorial Drive West

Lehigh University

Bethlehem, PA 18015

SUMMARY

The overall objective of this investigation was to determine the quantitative flow structure on wings subjected to basic classes of maneuvers, in order to provide a basis for interpretation of induced forces. Techniques of particle image velocimetry were employed for critical planes of the flow field, including streamwise and spanwise oriented planes, and near-surface planes. In addition, a technique of stereo particle image velocimetry was developed for water-based systems, including methods for minimizing mismatch of indices of refraction. Post-processing of the acquired images allowed determination of the vorticity and streamline topology, and construction of space-time volumes of the flow structure.

The three-dimensional flow structure on flapping wings, as well as wings in rectilinear motion, involves streamwise-oriented vorticity, located well inboard of the tip vortices. These vortical structures are associated with pronounced spanwise flow along the surface of the wing. Time resolved image acquisition allows insight into the unsteady separation and vortex development associated with generic classes of the flow structure.

Control techniques were employed to modify the flow structure. Passive control in the form of a sinusoidal leading-edge, which mimics the protuberances on the flipper of the humpback whale, can effectively eliminate streamwise vortices located inboard of the tip of a flapping wing. Furthermore, this type of control can minimize the extent of three-dimensional separation and stall on a wing with swept leading edges, which maneuvers to high angle of attack. Active open-loop control, in the form of small-amplitude perturbations of a wing at high angle of attack, can lead to major reduction of the spatial extent of stall, via manipulation of the small-scale vortical structures in the separated shear layer.

Synopses of the investigations completed during this program are summarized in the following. These studies resulted in journal publications.

FLOW STRUCTURE ON A THREE-DIMENSIONAL WING SUBJECTED TO SMALL AMPLITUDE PERTURBATIONS

Small amplitude angular perturbations, of the order of one-half degree, can substantially modify the flow structure along a three-dimensional wing configuration, which is quantitatively characterized using a technique of high-image-density particle image velocimetry. Excitation at either the fundamental or the first subharmonic of the spanwise-averaged instability frequency of the separating shear layer from the stationary wing nearly eliminates the large-scale separation zone along the wing at high angle of attack. The physics of the flow is interpreted in terms of time-mean streamlines, vorticity and Reynolds stress, in conjunction with phase-averaged patterns of instantaneous vorticity. Distinctive vorticity patterns occur along the leading edge when the time-averaged separation zone is minimized.

This investigation is described in Appendix A.

THREE-DIMENSIONAL FLOW STRUCTURE ON A MANEUVERING WING

Unsteady plunging (heaving) of a wing in the form of a flat plate can give rise to pronounced axial flow in the small-scale leading-edge vortex, during its initial stage of formation. Opposing axial flows along the vortex interact at the plane of symmetry, giving rise to large-scale patterns of streamwise-oriented vorticity, which can dominate the tip vortices over part of the oscillation cycle.

This investigation is described in Appendix B.

SCALING OF FLOW SEPARATION ON A PITCHING LOW ASPECT RATIO PLATE

We use two different dye injection approaches, in two different water tunnels, to visualize the formation and subsequent evolution of leading-edge vortices and related separated structures, for a pitching low aspect ratio plate. The motion is a smoothed linear pitch ramp from 0° to 40° incidence, brief hold, and return to 0° , executed at reduced pitch rates ranging from 0.1 to 0.35 and about various pivot locations. All cases evidence a leading edge vortex with pronounced axial flow, which leads to formation of large-scale, three-dimensional flow structures, culminating in a large vortical structure centered at the wing symmetry-plane. Pitch is also compared to plunge, whereby the functional form of the plunging motion provides an equivalent variation of angle of attack with time that matches the pitching motion. At successively increasing values of time, represented by the convective time scale C/U , the three-dimensional patterns of the flow structure are remarkably similar for the pitching and plunging motions. The similarity of these patterns persists, though they are shifted in time, for variation of either the location of the pitching axis or the dimensionless pitch rate.

This investigation is described in Appendix C.

CONTROL OF VORTICAL STRUCTURES ON A FLAPPING WING VIA A SINUSOIDAL LEADING-EDGE

The flow structure generated by a flapping wing in the form of a plate is fundamentally altered if the leading-edge has a sinusoidal shape. It is possible to attenuate both the positive and negative spanwise flow along the plate surface, as well as the onset and development of large-scale concentrations of positive and negative streamwise vorticity at inboard locations. These alterations of the inboard flow structure have an insignificant influence on the structure of the tip vortex.

This investigation is described in Appendix D.

VORTICAL STRUCTURES ON A FLAPPING WING

A wing in the form of a rectangular flat plate is subjected to periodic flapping motion. Space-time imaging provides quantitative representations of the flow structure along the wing. Regions of spanwise flow exist along the wing surface, and depending on the location along the span, the flow is either towards, or away from, the tip of the wing. Onset and development of large-scale, streamwise-oriented vortical structures occur at locations inboard of the tip of the wing, and they can attain values of circulation of the order of one-half the circulation of the tip vortex. Time-shifted images indicate that these streamwise vortical structures persist over a major share of the wing chord. Space-time volume constructions define the form and duration of these structures, relative to the tip vortex.

This investigation is described in Appendix E.

FLOW PAST A DELTA WING WITH A SINUSOIDAL LEADING-EDGE: NEAR-SURFACE TOPOLOGY AND FLOW STRUCTURE

The near-surface flow structure and topology on a delta wing of low sweep angle, having sinusoidal leading edges of varying amplitude and wavelength, are investigated using a stereoscopic technique of high-image-density particle image velocimetry at a Reynolds number of 15,000. Identification of critical points, in conjunction with surface-normal vorticity and velocity, provide a basis for determining the effectiveness of a given leading edge. At high angle of attack, where large-scale three-dimensional separation occurs from the wing with a straight leading edge, an amplitude of the leading-edge protuberance as small as one-half of one percent of the chord of the wing can substantially alter the near-surface topology. When the amplitude reaches a value of four percent of the chord, it is possible to completely eradicate the negative focus of large-scale, three-dimensional separation, in favor of a positive focus of attachment. Moreover, alteration of the near-surface topology is most effective when the ratio of the wavelength to amplitude of the sinusoidal leading edge is maintained at a small value.

This investigation is described in Appendix F.

EFFECT OF PITCH RATE ON NEAR-SURFACE TOPOLOGY ON A DELTA WING

The near-surface flow structure and topology on a delta wing of moderate sweep angle are investigated using a technique of high-image-density digital particle image velocimetry (DPIV). The focus is on the time evolution of the surface topology during relaxation of the flow after termination of a pitching maneuver, for a wide range of pitch rates. The near-surface patterns at the instant corresponding to termination of the maneuver are a strong function of the magnitude of pitch rate, and show substantial differences. On the other hand, irrespective of the severity of the flow distortion at the end of the pitching maneuver, the relaxation of the flow involves the same sequence of universal topological states. Furthermore, it is demonstrated that there exists a critical universal state, which marks an abrupt transformation between two distinctly different states of the near-surface topology. Moreover, it is demonstrated that the changes of the topological features observed during the early stages of the relaxation process are analogous to the alterations of the surface patterns obtained for the stationary wing at smaller angles-of-attack.

This investigation is described in Appendix G.

THESES AND DISSERTATIONS*

M.S. Thesis

Yilmaz, Turgut, "Flow Structure on a 1303 UCAV Subjected to Small Amplitude Perturbations", Janaury, 2009.

Ph.D. Dissertation

Goruney, Tunc, "Investigation of Flow Structure on a Pitching Delta Wing of Moderate Sweep Angle using Stereoscopic Particle Image Velocimetry", October, 2008.

* All theses and dissertations are available from the Department of Mechanical Engineering and Mechanics, Lehigh University, Bethlehem, PA 18015

PUBLICATIONS

The following journal articles of the author's research group were published during the period of the research:

- A. Yilmaz, T. O. and Rockwell, D. 2009 "Flow Structure on a Three-Dimensional Wing Subjected to Small Amplitude Perturbations", *Experiments in Fluids*, Vol. 47, No. 4-5, pp. 579-597.
- B. Yilmaz, T. O. and Rockwell, D. 2010 "Three-Dimensional Flow Structure on a Maneuvering Wing", *Experiments in Fluids*, vo. 48, No. 3 (March), pp. 539-544

- C. Yilmaz, T., Ol, M., and Rockwell, D. 2010 “Scaling of flow separation on a pitching low aspect ratio plate” *Journal of Fluids and Structures* vol. N6, pp. 1034–1041
- D. Ozen, C. and Rockwell, D. 2010 “Control of Vortical Structures on a Flapping Wing via a Sinusoidal Leading-Edge” *Physics of Fluids* Vol. 22, Issue 2
- E. Ozen, C. and Rockwell, D. 2010 “Vortical Structures on a Flapping Wing” *Experiments in Fluids* Published on line May 9
- F. Goruney, T. and Rockwell, D. 2009 "Flow Past A Delta Wing With A Sinusoidal Leading-Edge: Near-Surface Topology and Flow Structure", *Experiments in Fluids*, Vol. 47, Issue 2, pp. 321-331.
- G. Goruney, T. and Rockwell, D. 2010 “Effect of Pitch Rate on Near-Surface Topology on a Delta Wing” *AIAA Journal* Vol. 48, No. 6, June, pp.1207-1220

APPENDIX A

FLOW STRUCTURE ON A THREE-DIMENSIONAL WING SUBJECTED TO SMALL AMPLITUDE PERTURBATIONS

ABSTRACT

Small amplitude angular perturbations, of the order of one-half degree, can substantially modify the flow structure along a three-dimensional wing configuration, which is quantitatively characterized using a technique of high- image-density particle image velocimetry. Excitation at either the fundamental or the first subharmonic of the inherent instability frequency of the separating shear layer nearly eliminates the large-scale separation zone along the wing at high angle of attack. The physics of the flow is interpreted in terms of time-mean vorticity and Reynolds stress, in conjunction with phase-averaged patterns of vorticity. Distinctive vorticity patterns occur along the leading edge when the time-averaged separation zone is minimized.

1. EXPERIMENTAL SYSTEM AND TECHNIQUES

Experiments were undertaken in a large-scale water facility, in the form of a free-surface water channel. It had a main test section 613 mm wide and 594 mm long, with a length of 5435 mm. A flow conditioning section was located upstream of this test section. It involved an arrangement of honeycomb and a sequence of five screens, in order to attain low turbulence intensities of approximately 0.3%. The free-stream velocity was varied over the range $23.6 \leq U_\infty \leq 251$ mm/sec.

A simplified schematic of the 1303 UCAV arrangement is shown in Figure A1a and b, in conjunction with solids model representations of this type of wing. A half-wing arrangement was mounted on a vertical plate within a water channel, as illustrated in the schematic. The sweep angle was $\Lambda = 47^\circ$ and the semi-span was $S = 300$ mm. In order to preclude the effects of the approach boundary layer, it was, first, maintained very thin by locating the apex of the wing immediately downstream of the leading-edge of the vertical mounting plate. Moreover, the wing model was manufactured in such a way that the plane of symmetry of the wing was away from the vertical plate. The root chord of the wing was $C_{\text{root}} = 355.6$ mm and the displacement of the plane of symmetry of the wing from the vertical mounting plate was $\Delta = 38.1$ mm. The displacement thickness of the approach boundary layer along the vertical plate was an order of magnitude smaller than the gap Δ between the vertical plate and the tip of the wing.

The blockage ratio of the wing was 0.026 and 0.054 at angles-of-attack $\alpha = 0^\circ$ and 12° . Extensive dye visualization experiments and PIV measurements, in conjunction with those on a full model of the 1303 UCAV showed that the type of half-wing model of Figure A1 closely replicates the flow pattern on the full wing. Figure A1c shows a dye pattern due to injection in the apex region, at the Reynolds number $Re_C = 17,927$ and angle of attack $\alpha = 12^\circ$ of interest herein. This instantaneous pattern remains essentially symmetrical along the center body, except for the influence of unsteady distortion due to transitional effects at locations well downstream. Also shown is dye visualization in the critical apex region at higher values of Reynolds number, $Re_C = 29,878$, and $59,757$. For the full wing experiments of Kosoglu (2007), the root chord and freestream velocity were respectively one-half and twice the present values in order to attain the same value of Reynolds number $Re_C = 17,927$. Figure A1d shows strong similarity of the PIV

patterns of contours of constant vorticity, Reynolds stress and streamlines for the present configuration and the full wing of Kosoglu (2007), at a spanwise location $\eta = 0.1$, i.e., a distance of 10% of the span of the half wing, measured from the center body. In addition, dye visualization over the entire semi-span of interest (not shown herein) was compared at $Re_C = 17,927$ for the present configuration and the full wing of Kosoglu (2007). The location of the onset of abrupt expansion of the leading-edge vortex, as well as the location and shape of the interface between the stalled and unstalled regions along the wing were essentially the same.

For the present experiments, the value of Reynolds number based on root chord was $Re_{C_{root}} = 30,000$, corresponding to a Reynolds number based on the mean aerodynamic chord of $Re_C = 17,927$. Preliminary experiments on the stationary (unperturbed) wing were performed at four values of angle-of-attack $\alpha = 6^\circ, 9^\circ, 12^\circ$ and 15° . It was found that an angle-of-attack $\alpha = 12^\circ$ provided a fully-stalled condition, which provided a basis for investigation of the effectiveness of perturbations on altering the stalled flow patterns; this value of α is employed herein. Perturbations of angle-of-attack were induced by a computer-controlled motor system, which was mounted above the water channel, in the manner shown in Figure A1. An adjustable jack provided variations in tension of the belt from the motor system to the axis of rotation of the wing, which was at the mid-chord of the 1303 UCAV model. This system provided perturbation frequencies up to 5 Hz for an amplitude of the pitching motion corresponding to 0.45° .

Ho and Huerre (1984) assess a wide variety of works involving perturbation of a shear layer separating from an edge. Excitation of the convective instability at the fundamental (most unstable) frequency f_o , or one of its subharmonics f_o/n , is particularly effective. This guidance provided the basis for selection of the excitation frequencies employed in this investigation, f_o to $f_o/8$. For the present configuration, the most unstable frequency varies along the span of the stationary leading-edge, and the spanwise-averaged value of f_o is considered. When the wing is perturbed, the frequency of the initial region of development of the instability is constant along the span, as verified with dye visualization. Furthermore, in the limiting case of a linearly evolving disturbance from the leading-edge of the wing, it is known from the inviscid stability calculations of Michalke (1964) that the separating shear layer can effectively amplify disturbances, that is, the magnitude of the amplification factor is large, over a relatively wide band of frequencies.

In accord with the foregoing, the wing was perturbed at the fundamental f_o and subharmonics $f_o/2$, $f_o/4$, and $f_o/8$ of the spanwise-averaged frequency f_o of small-scale vortex formation from the leading-edge of the stationary wing. This vortex formation was clearly prevalent at the spanwise locations $\eta = 0.5$ to 0.9 . The frequency $f_o = 2.5\text{Hz}$ corresponds to a dimensionless frequency $f_o C/U = 6.64$ based on mean aerodynamic chord, and dimensionless frequencies $f_o C^*/U = 4.86, 2.56$ and 1.44 based on values of sectional chord C^* at spanwise locations $\eta = 0.5, 0.7$ and 0.9 , in which $\eta = y/S$, where S is the semi-span of the wing.

A technique of high-image-density particle image velocimetry was employed to characterize the flow patterns. The orientation of the laser sheet is shown in Figure A1. The laser was mounted on a traverse system, allowing images to be acquired at various spanwise locations η .

The water was filtered with a one micron filter system and subsequently seeded with 12 micron diameter metallic coated plastic spheres. The seeding density was sufficiently high that 14 particle images were typically attained within the interrogation window of $32 \text{ pixels} \times 32 \text{ pixels}$ employed for PIV. The laser sheet was generated by a dual pulsed Yag laser system having a maximum output of 90 mJ; approximately one-half of this output was employed during

the current experiments. The pulse rate of the lasers was 29 Hz, which corresponds to the acquisition of 14.5 image pairs per second.

Processing of the patterns of particle images involved a frame-to-frame cross-correlation technique. A 32×32 pixel interrogation window was employed, with a 50% overlap. During the course of the experiments, acquisition of images at various spanwise locations η along the span of the wing required readjustment of the distance from the sensor array of the camera to the physical plane of the laser sheet. This distance ranged from 456 mm to 1052 mm. In turn, this range corresponds to effective values of magnification extending from 19.7 to 4.55, and values of grid size (distance between locations of velocity vectors) in the physical plane of the laser sheet from 1.624 to 7.033 mm. More specifically, at values of $\eta = 0.1, 0.3, 0.5, 0.7$ and 0.9 , the values of magnification were 4.55, 7.07, 9.77, 13.414 and 19.77 pixel/mm, and the effective grid sizes were 7.033, 4.557, 3.275, 2.385 and 1.624 mm. In the present investigation, images were not considered at $\eta = 0.1$. Values of magnification and grid size correspond to fields of view in the physical plane of the laser sheet of 212 mm x 98 mm, 152 mm x 88 mm, 108 mm x 67 mm, and 75 mm x 43 mm at $\eta = 0.3, 0.5, 0.7$, and 0.9 , respectively. Furthermore, the number of pixels of the imaging camera was 1,600 pixels x 1,200 pixels. The overall uncertainty of the velocity measurements is estimated to 1.5%. The PIV technique was also employed to determine the oscillation amplitude of the wing. By considering the time sequence of raw (unprocessed) images, during the oscillation cycle, it was possible to track the surface of the wing, and attain resolution within an uncertainty of 0.015° , in comparison to the oscillation amplitude of 0.45° .

In order to determine the time-averaged patterns of velocity vectors, $\langle \mathbf{V} \rangle$, a total of 200 instantaneous images were averaged. Furthermore, time-averaged representations of the flow structure, involving surface normal vorticity $\langle \omega \rangle$, streamlines $\langle \Psi \rangle$, and contours of constant streamwise velocity $\langle u \rangle$ were calculated from the time-averaged patterns of velocity vectors.

2. TIME-AVERAGED FLOW STRUCTURE

Figures A2a shows overviews of the time-averaged dimensionless vorticity $\langle \omega \rangle C_{ROOT}/U$ and Reynolds stress correlation $\langle u'v' \rangle / U^2$, and Figure A2b provides patterns of the streamwise component of velocity $\langle u \rangle / U$ and streamlines $\langle \Psi \rangle$. In each set of images, the pattern corresponding to the stationary wing is given, then the effects of increasing values of excitation frequency $f_e = f_o/8, f_o/4, f_o/2$, and f_o are illustrated. The frequency f_o is the spanwise-averaged value of the inherent instability frequency of small-scale vortex formation in the separated shear layer, over the regions of the wing, where the flow has a well defined region of separation, namely from $\eta = 0.5$ to 0.9 . This averaged value was $f_o = 2.5$ Hz. Values of frequency f_o^* at each spanwise location η were determined using a global spectral analysis of the unsteady vorticity, whereby the spectrum of the vorticity fluctuation was determined at each of the 3999, 5022, 5096, 5612, and 4876 grid points in the image of the flow field at values of $\eta = 0.3, 0.5, 0.7, 0.8$ and 0.9 . In Figure A2a, the patterns of dimensionless vorticity $\langle \omega \rangle C_{ROOT}/U$, given in the left column indicate that at values of excitation frequency $f_e = f_o/8$ and $f_o/4$, the extent of the peak (red) regions of vorticity successively decrease, relative to the case of the stationary wing. At $f_e = f_o/2$, the initial region of peak (red) vorticity is attached to the leading-edge of the wing, and further downstream, the vorticity layer bifurcates into a higher magnitude region along the surface of the wing, and a lower magnitude along the locus of the separated shear layer. At the highest value of excitation frequency, $f_e = f_o$, this bifurcation occurs earlier, the streamwise extent of the vorticity layer along the surface of the wing is shorter, and the magnitude of vorticity in

the residual region of the separated shear layer is larger, relative to excitation at $f_e = f_o/2$. The flow structure at successive instants during the oscillation cycle, which are associated with the time-averaged patterns at $f_e = f_o/2$ are addressed subsequently in Figure A6.

Figure A2a also shows corresponding patterns of Reynolds stress correlation $\langle u'v' \rangle / U^2$. Values of $f_e = f_o/8$ and $f_o/4$ result in larger regions of large magnitude (dark blue) $\langle u'v' \rangle / U^2$ and, furthermore, advancement of the onset of this high magnitude (dark blue) region towards the leading-edge of the wing, relative to the case of the stationary wing. At higher values of $f_e = f_o/2$ and f_o , alternating patterns of large magnitude negative (dark blue) and positive (dark red) Reynolds stress correlation are generated along the surface of the wing. In the region upstream of the leading-edge of the wing, the increase in the pronounced regions of positive and negative concentration of $\langle u'v' \rangle / U^2$ is due to the correlations of irrotational fluctuations induced by the wing motion.

Figure A2b shows, in the left column, patterns of time-averaged streamwise velocity $\langle u \rangle / U$. The effect of increasing frequency, up to a value of $f_e = f_o/2$ is to decrease the region of negative or very low (dark blue) streamwise velocity, i.e., the flow approaches an attached state along the entire streamwise extent of the wing section at $f_e = f_o/2$. At $f_e = f_o$, the concentration of negative $\langle u \rangle / U$, immediately above the trailing-edge is associated with the vortical motion induced by the trailing-edge, already evident in the pattern of $\langle \omega \rangle C_{ROOT} / U$ at $f_e = f_o$ in Figure A2a.

Patterns of streamlines given in the right column of Figure A2b show a highly stalled region above the wing when it is stationary. At $f_e = f_o/8$, a limit cycle pattern of streamlines is formed and, interior to this limit cycle, an inward spiral towards the focus (center) is clearly evident. At $f_e = f_o/4$, the flow tends toward reattachment along the streamwise extent of the airfoil; a separation bubble is located at approximately mid-chord. At $f_e = f_o/2$, this bubble becomes smaller in magnitude and moves toward the leading-edge. A detectable bubble is still located at the leading-edge at $f_e = f_o$, and the flow is approximately parallel to the surface of the wing until the trailing-edge region is reached, where the time-averaged vortex, induced by the aforementioned trailing-edge motion, is evident in the form of an outward spiraling pattern.

Figure A2c shows superposition of patterns of streamlines and contours of constant streamwise velocity, selected from Figure A2b. The relationship between regions of very low or negative streamwise velocity and patterns of streamlines is directly evident.

Figures A3a and A3b show images of the same parameters as for Figures A2a and A2b, except at a spanwise location $\eta = 0.5$. At this value of η , due to the sweep of the leading-edge of the wing, the dimensionless magnitude of the unsteady displacement of the leading-edge of the wing is $\tilde{y} / C^* = 0.0023$, compared with the previous sets of images at $\eta = 0.9$, for which $\tilde{y} / C^* = 0.036$. In the left column of Figure A3a, at $f_e = f_o/8$, the streamwise extent of the large amplitude (red) vorticity $\langle \omega \rangle C_{ROOT} / U$ decreases substantially, relative to its counterpart on the stationary wing. This reduction persists, for all values of f_e up to $f_e = f_o$. Furthermore, at all values of excitation frequency f_e , there exists a well-defined, yet low magnitude, layer of $\langle \omega \rangle C_{ROOT} / U$ along the surface of the wing.

Patterns of Reynolds stress correlation of $\langle u'v' \rangle / U^2$, shown in the right column of Figure A3a, indicate that the onset of large magnitude negative (dark blue) $\langle u'v' \rangle / U^2$ advances towards the leading-edge of the wing with increasing values of f_e all the way up to $f_e = f_o$. Furthermore, the scale of the region of large negative (dark blue) $\langle u'v' \rangle / U^2$ becomes significantly larger in regions near the leading-edge of the wing at $f_e = f_o/2$ and f_o .

Figure A3b shows, in the left column, patterns of $\langle u \rangle / U$. The general effect of increasing values of excitation frequency is a decrease in the spatial extent of the large negative (dark blue) magnitudes and, in the corresponding streamline patterns, a region of substantial stall on the stationary wing is very significantly attenuated, relative to the case of the stationary wing, even for the lowest excitation frequency $f_e = f_o/8$, and this trend persists up through $f_e = f_o/2$ in the form of a separation bubble along the surface of the wing. At $f_e = f_o$, the flow is nearly attached along the entire extent of the wing.

Taking an overview of the images of Figures A2 and A3, it is evident that the higher values of excitation frequency $f_e = f_o/2$ and f_o are the most effective in altering the flow structure along the sectional chord of the wing, i.e., in promoting reattachment of the flow to the wing surface. At $\eta = 0.9$, deflection of the separated shear layer from the surface of the wing is large, and the corresponding region of separated flow has a large extent; excitation at $f_e = f_o/2$ is effective, while not inducing large regions of separated, vortical motion in the vicinity of the trailing-edge. Moreover, it is important to note that, at $f_e = f_o/2$, the streamwise extent of the higher level of vorticity along the surface of the wing is largest, and the residual vorticity in the trajectory of separated shear layer is smallest. At $\eta = 0.5$, when the separated layer is closer to the surface of the wing, and the spatial extent of separated flow is smaller, excitation at $f_e = f_o/2$ eliminates the zone of separation, except for a separation bubble along the surface of the wing. At $f_e = f_o$, the separated region is nearly eliminated. In the following, the flow structure is addressed in further detail for excitation at $f_e = f_o/2$.

Figures A4a through A4c compare the flow structure on the stationary wing section (left column) with that due to excitation (right column) at five different spanwise sections, extending from $\eta = 0.3$ to 0.9 . As shown in Figure A4a, irrespective of the spanwise location η , the effect of excitation is to substantially decrease the streamwise extent of the high magnitude (red) region of $\langle \omega \rangle C_{ROOT} / U$, while broadening the spanwise extent of the vorticity layer, in comparison with patterns on the stationary wing. At all spanwise locations, the initial region of the separated shear layer is drawn closer to the wing in presence of excitation, relative to its trajectory from the stationary wing. In the limiting case, at $\eta = 0.3$, the leading-edge separation bubble on the stationary wing appears to be eliminated in presence of the perturbation.

Figure A4b compares patterns of Reynolds stress correlation $\langle u'v' \rangle / U^2$. For all spanwise locations η , the effect of excitation is to substantially advance the onset of high magnitude negative (dark blue) $\langle u'v' \rangle / U^2$ towards the leading-edge of the wing, relative to the corresponding patterns on the stationary wing. For the limiting case of the wing section close to the plane of symmetry, at $\eta = 0.3$, where only a small-scale leading-edge separation bubble is formed, high magnitude negative (dark blue) Reynolds stress is not generated.

Patterns of streamlines, given in Figure A4c, indicate that the effect of excitation is to substantially reduce the spatial extent of regions of large-scale flow separation that occur on the stationary wing. At all values of η , regions of upstream-oriented streamlines are eliminated. At values of $\eta = 0.7, 0.8$ and 0.9 , a small-scale, leading-edge separation bubble persists and, at $\eta = 0.5$, the location of this bubble moves downstream along the surface of the wing. At $\eta = 0.3$, the leading-edge separation bubble is eliminated.

3. INSTANTANEOUS AND PHASE-REFERENCED FLOW STRUCTURE

Figure A5 shows patterns of instantaneous and phase-averaged vorticity for the case of the stationary wing. Small-scale vortical structures form in the separated shear layer. Details

regarding the frequencies of formation of these small-scale structures are given in Section 1. The images of Figure A5 provide a basis for interpretation of the wavelength λ between the initially-formed vortices, normalized by the mean aerodynamic chord C , i.e., $\lambda/C = 0.065, 0.072, 0.076$ and 0.11 at values of $\eta = 0.5, 0.7, 0.8$ and 0.9 . These values of wavelength may also be normalized with respect to the sectional chord C^* at each value of η . With this normalization, $\lambda/C^* = 0.11, 0.17, 0.21$ and 0.43 for the respective values of η indicated in the foregoing. These images of the vortex patterns in Figure A5 provide a basis for comparison with corresponding patterns of vorticity for the perturbed wing, which can be fundamentally different.

Figure A6 shows patterns of phase-averaged vorticity over an entire oscillation cycle for the case of the wing perturbed at the most effective frequency $f_o/2$. The instantaneous vertical displacement of the leading-edge of the wing is designated as $h(t)$ in the schematic. The image at the upper left of Figure A6 corresponds to the maximum-positive displacement and that at the upper right represents the maximum-negative displacement. Moreover, each image has a specified value of t/T , in which t is time and T is the period of the wing motion. At $t/T = 0$, an elongated layer of vorticity exists along nearly the entire chord of the wing, and in the vicinity of the leading-edge, high magnitudes are evident. This overall pattern persists at $t/T = 0.1$ and 0.2 , while the previously formed concentration of vorticity, represented by the large (green-yellow) cluster, continues to translate downstream. At $t/T = 0.3$, the elongated layer of high magnitude (red) vorticity in the vicinity of the leading-edge starts to partition into two discrete concentrations, and this process continues at $t/T = 0.4, 0.5$ and 0.6 . At $t/T = 0.7$, the segregation of vorticity concentrations is complete, and the larger-scale concentration starts to move along the trajectory of the separated shear layer, while the concentration in the vicinity of the leading-edge becomes increasingly elongated, and eventually merges into the layer that extends along the entire surface of the wing. The bifurcation of the time-averaged pattern of vorticity shown in Figure A2a therefore involves: the averaged consequence of discrete vortical structures originating from that portion of partitioned vorticity shed from the surface of the wing; and the averaged form of that region of the partitioned vorticity that remains along the surface of the wing. As suggested by a reviewer, it is possible that reattachment in planes located in board of the plane of interest contributes to the wall vorticity layer of Figure A6.

The overview of Figure A7a shows the effect of excitation frequency at $\eta = 0.9$. Images in the left column are phase-referenced according to the appearance of cluster a at the same location. The right column of Figure A7a shows images one-half cycle later. At frequencies f_o and $f_o/2$, in the left column of images at $t = t_r$, an elongated region of high level (red) vorticity is formed along the leading-edge. At f_o , this high level layer becomes part of a lower level layer that exists over approximately one-half chord of the wing. At $f_o/2$, the lower level layer exists over the entire chord of the wing. Moreover, at f_o , a concentration of vorticity exists in the separated layer between the leading-edge and cluster a . On the other hand, at $f_o/2$, no such concentration exists in the separated layer; rather, it appears to remain attached to the surface of the wing as part of the high concentration (red) layer at the leading-edge. Furthermore, the images at $t_e = t_r + T_o/2$ shows that, at frequency f_o , the vorticity concentration leaves the surface at the leading-edge, whereas at $f_o/2$, its departure is delayed until about one-third chord. This delay in departure no doubt contributes to the extension of the surface vorticity layer over the entire chord of the wing section. Finally, at the low value of excitation frequency $f_o/4$ in Figure A7a, well-defined, smaller-scale vorticity concentrations are not formed in the immediate vicinity of the leading-edge. The large-scale concentration a represents an agglomeration of vorticity in the separated shear layer.

Figure A7b shows the patterns of vortex formation at $\eta = 0.5$. As in Figure A7a, concentrations of vorticity designated as a serve as the phase-reference. At all values of excitation frequency, the region of high magnitude (red) vorticity formed at the leading-edge is significantly reduced in spatial extent, relative to the case of the stationary wing. Furthermore, the initially formed concentration a has a significantly reduced value of peak vorticity. These initial concentrations of a in presence of excitation are located closer to the surface of the wing section than for the stationary wing. As represented by the images in the right column of Figure 7b, the vortical activity close to the surface of the wing section is particularly evident at excitation frequencies f_o and $f_o/2$. These observations are associated with a substantial reduction in the extent of the region of flow separation, as indicated in Figure A4c. Furthermore, the initially formed concentration a has a significantly reduced value of peak vorticity. This may be due to jitter or meandering of that vorticity concentration.

In the foregoing, a range of excitation frequency has been considered, and these frequencies are represented by the inherent instability frequency f_o averaged along the span, and its subharmonics. High-frequency excitation of flat delta wings is addressed in the investigation of Vardaki et al. (2008). They found that the most effective frequencies, for inducement of flow reattachment, were in the range $fC/U = 1$ to 2. The present configuration is a substantial departure from a flat delta wing, that is, the existence of the crank configuration of the trailing-edge yields unusual variations of sectional chord C^* as a function of dimensionless spanwise location η . Furthermore, the central portion of the wing is thick and the flow is essentially attached in that region. A well-defined separated shear layer exists at the spanwise locations in the outboard region, $\eta = 0.5, 0.7$, and 0.9 . So, direct comparison of the most effective frequencies of a flat delta wing and the high of the three-dimensional configuration of interest herein should be done with caution. If the fundamental frequency f_o is employed as a basis for comparison, the dimensionless frequencies based on local chord C^* are $f_o C^*/U = 4.86, 2.56$ and 1.44 at $\eta = 0.5, 0.7$, and 0.9 . On the other hand, if one views excitation at the subharmonic component $f_o/2$ as the most effective frequency, then the corresponding dimensionless frequencies are $2.43, 1.28$, and 0.72 at $\eta = 0.5, 0.7$, and 0.9 . These dimensionless frequencies are of the same order as those determined by Vardaki et al. (2008) for the flat delta wing.

4. CONCLUSIONS

The present investigation has focused on modification of the flow structure on a three-dimensional wing at high angle-of-attack. Small amplitude perturbations (0.45°) are applied over a range of frequencies corresponding to the fundamental and subharmonics of the inherent instability frequency of the shear layer that separates from the leading-edge. A technique of high-image-density particle image velocimetry is employed to determine various representations of the instantaneous phase- and time-averaged flow structure. The principal findings are as follows.

1. Time-averaged patterns of streamwise velocity and streamline topology indicate that excitation at either the fundamental or subharmonic of the inherent instability frequency is particularly effective in altering the flow structure at high angle-of-attack. It is possible to nearly eliminate large-scale stalled regions, and attain reattachment of the flow, except for smaller-scale separation bubbles.
2. The foregoing reduction in spatial extent of the separation zone is accompanied by: a substantial reduction in the streamwise extent of the high-magnitude, time-averaged vorticity

in the separating shear layer; and an increase in magnitude of the Reynolds stress, as well as advancement of the regions of high Reynolds stress towards the leading-edge of the wing.

3. The physical mechanisms associated with the preceding changes have been characterized in terms of patterns of phase-averaged vorticity, acquired during the oscillation cycle of the wing perturbation. In essence, a layer of high-magnitude vorticity attached to the leading-edge is partitioned into two regions: one part forms a sequence of discrete clusters of vorticity shed from the surface of the wing; and the other part merges into the vorticity layer along the surface of the wing. For the latter, its streamwise extent is related to the delay in departure of the vorticity concentration from the surface, which is a function of the excitation frequency. Regarding the vorticity layer along the surface of the wing, as suggested by a reviewer, it may be influenced by flow reattachment at a location inboard of the sectional plane of interest. In future investigations, it would be insightful to address this aspect.
4. The foregoing conclusions focus on the response to excitation at the fundamental and first subharmonic of the inherent instability frequency of the separating shear layer. It is possible, however, to induce significant changes of the time-averaged patterns of the flow structure, even when the excitation frequency is well separated from the inherent instability frequency, e.g., a value as low as one-eighth of this frequency and, for transverse displacements of the leading-edge as small as 0.2 percent of the local chord. This finding indicates that very small, self-excited elastic perturbations of the wing, or small perturbations in the inflow, can significantly alter the time-averaged flow structure.

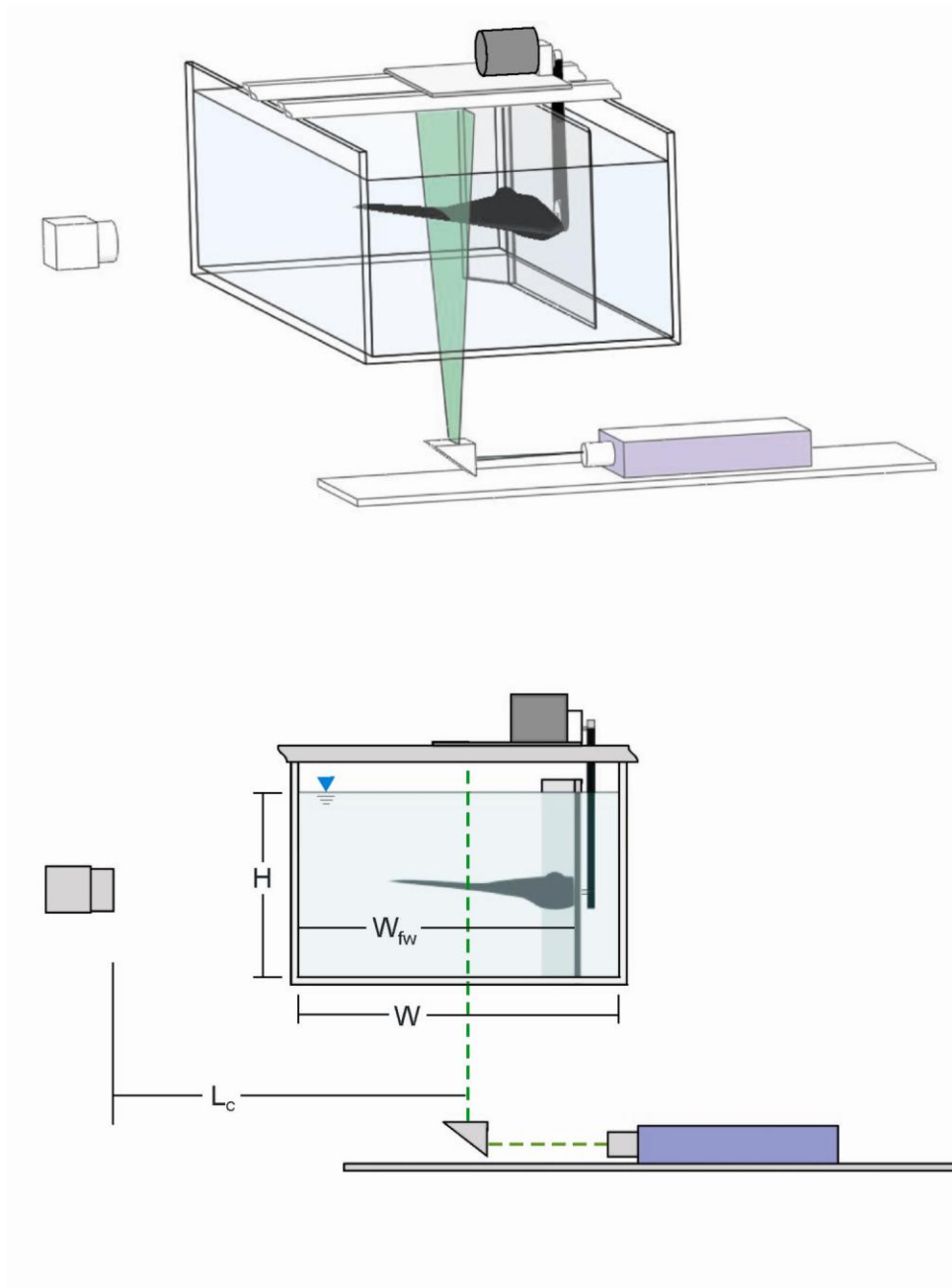


Figure A1a : Overview of experimental system

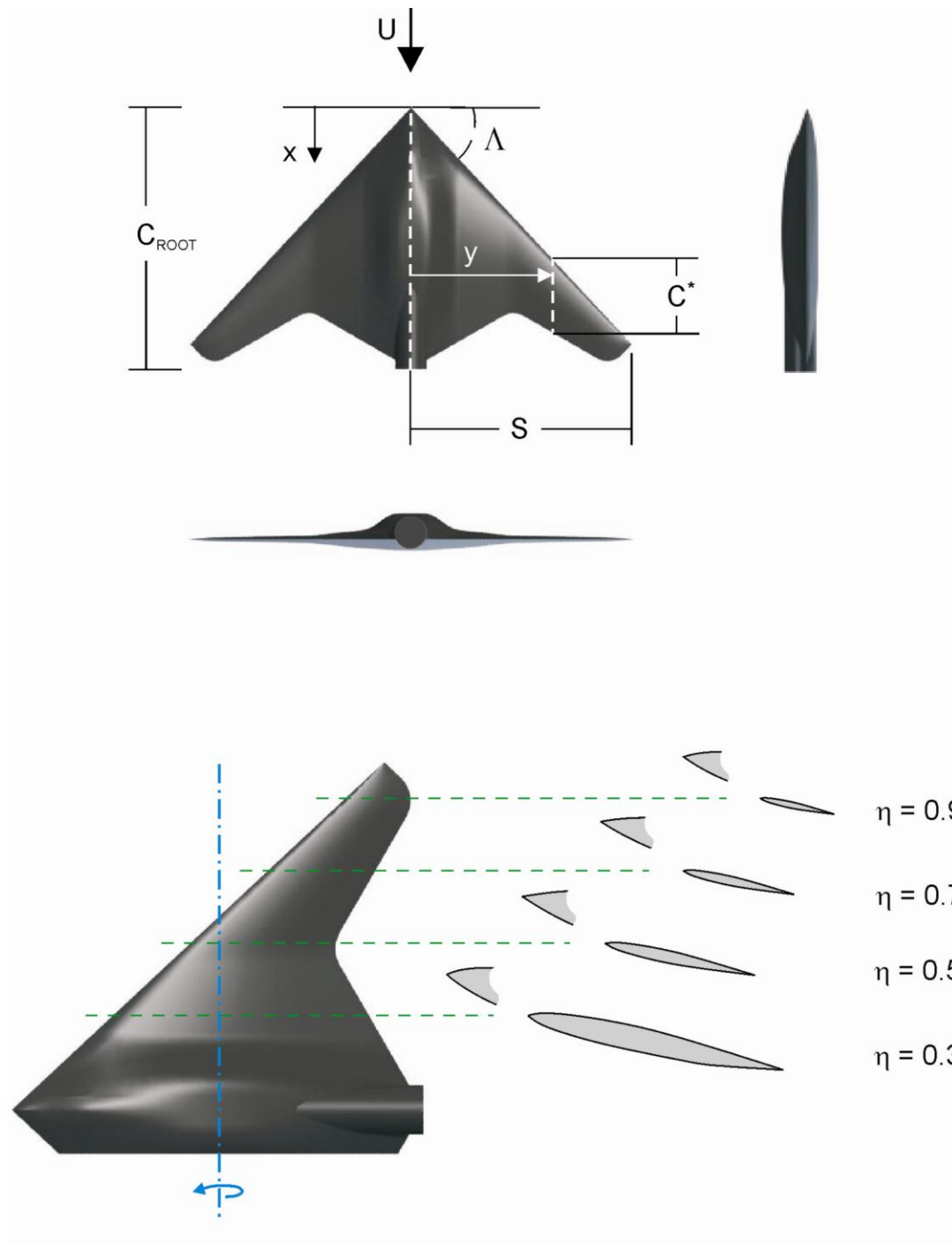


Figure A1b : Definitions of the parameters and zoomed-in views of half wing in relation to full wing

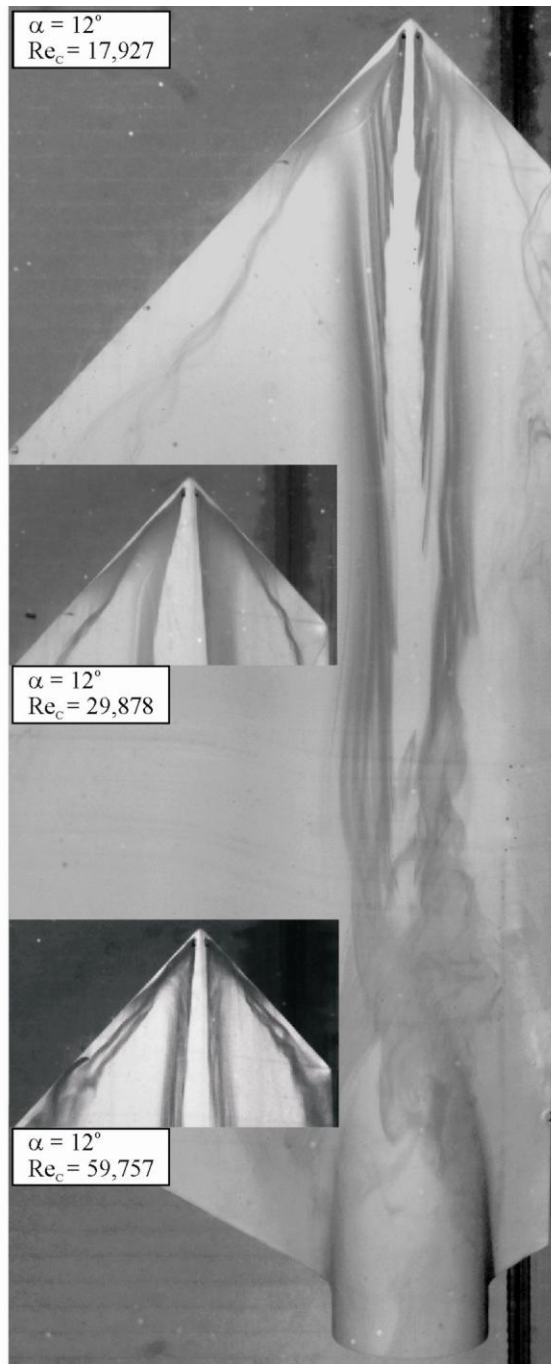


Figure A1c : Dye visualization of flow past apex region and center body of wing

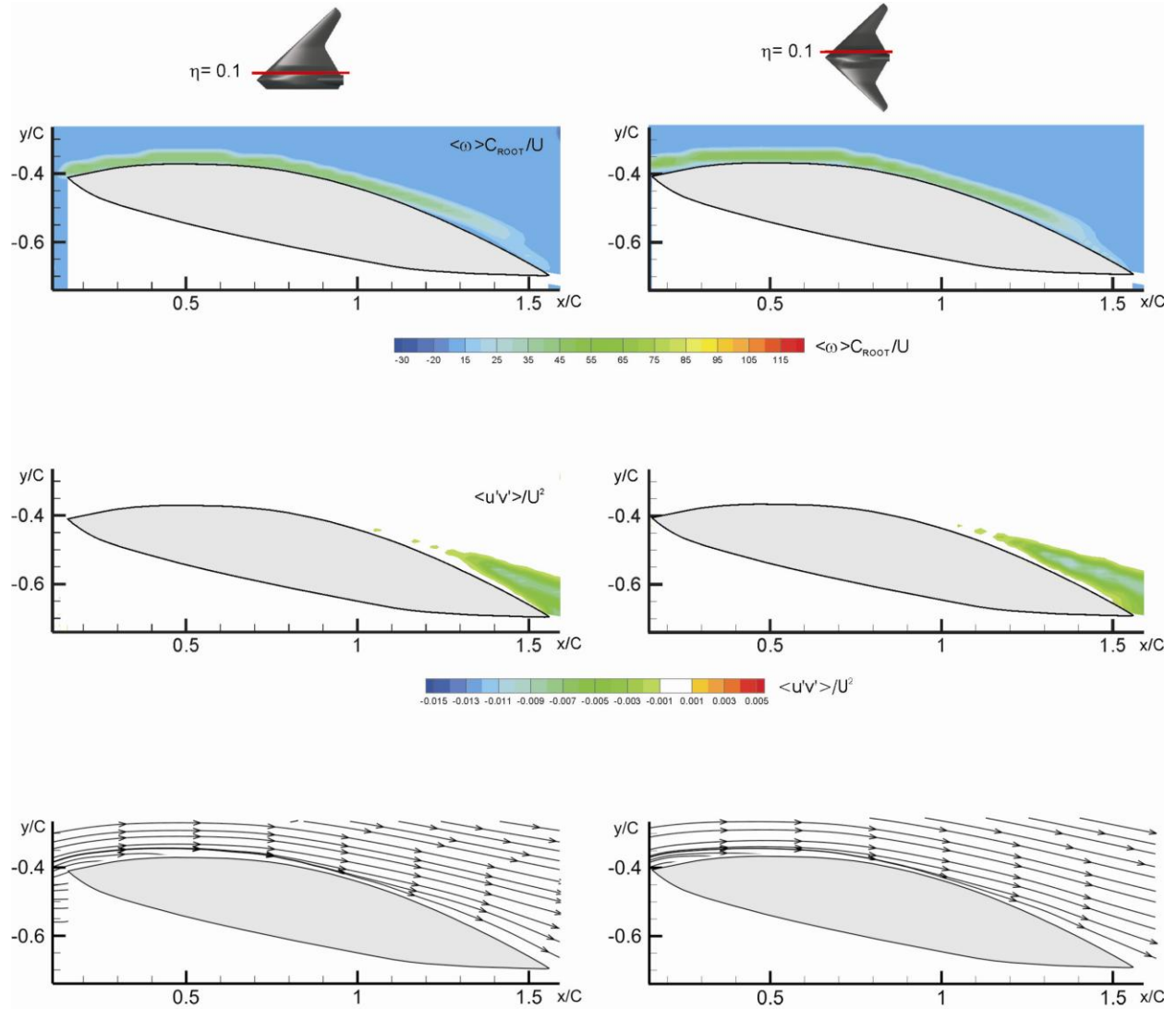


Figure A1d : Comparison of patterns of vorticity, Reynolds stress and streamlines for a half (present investigation) and full wing (Kosoglu 2007) at $\alpha = 6^\circ$ and $Re_c = 29,878$

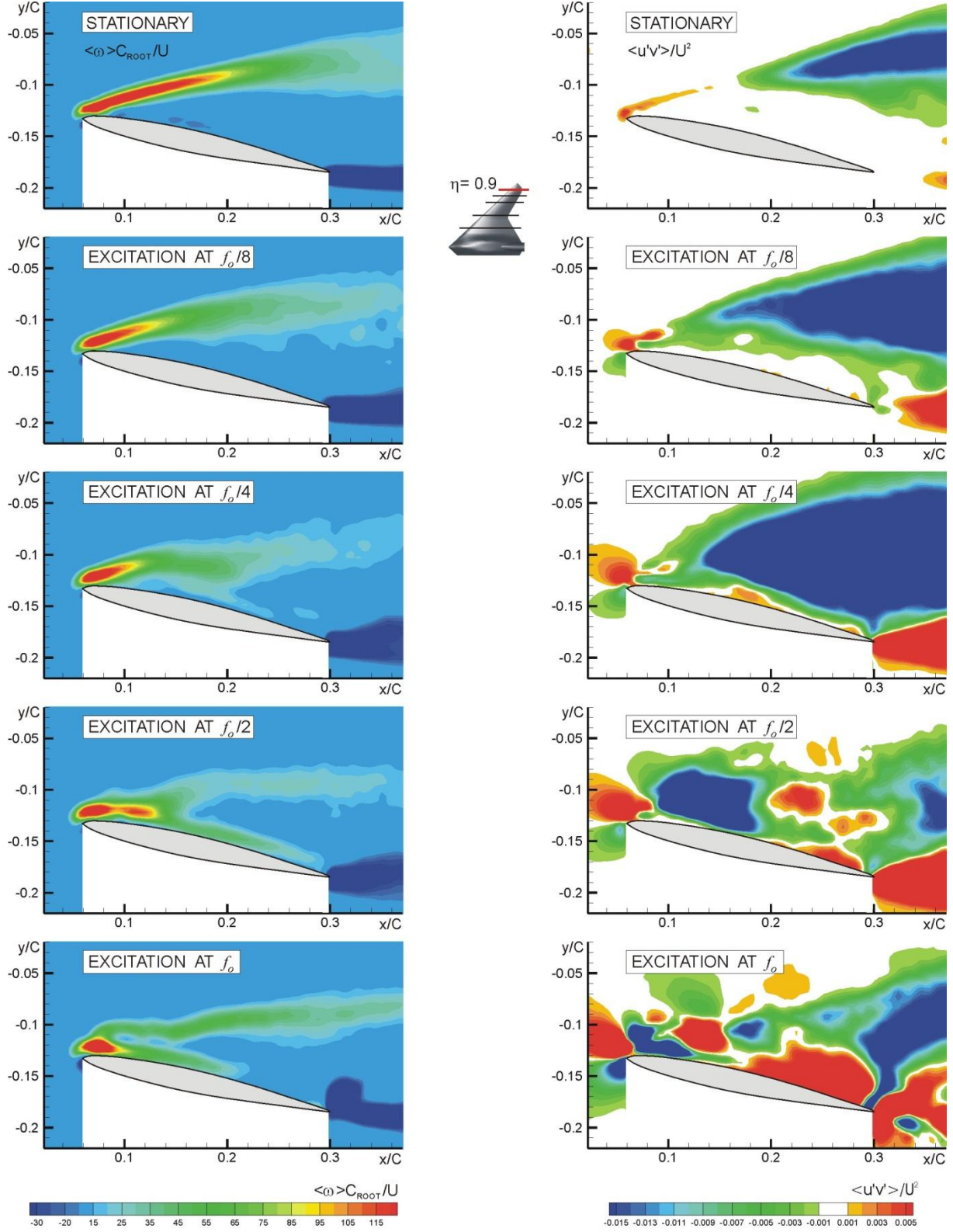


Figure A2a: Time-averaged vorticity and Reynolds stress contours for case of wing subjected to perturbations of angle-of-attack according to $\alpha = \bar{\alpha} + \alpha_e \sin 2\pi f_e t$; $\bar{\alpha} = 12^\circ$, $\alpha_e = 0.45^\circ$ and $f_e = f_o/8, f_o/4, f_o/2$, and f_o where f_o is the inherent instability frequency of separating shear layer. Reynolds number based on mean aerodynamic chord is $Re_c = 17927$

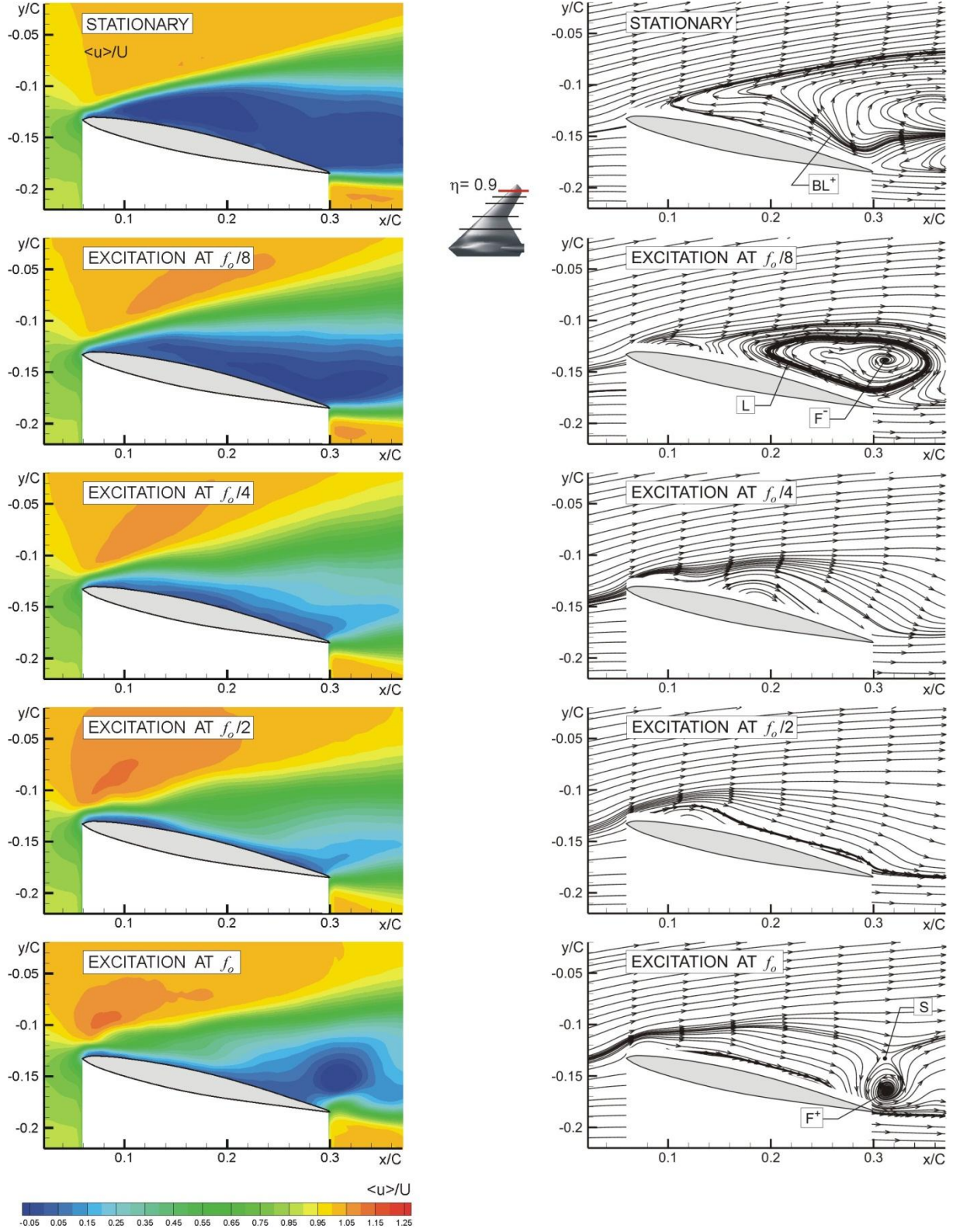


Figure A2b: Time-averaged streamwise velocity contours and streamlines for case of wing subjected to perturbations of angle-of-attack according to $\alpha = \bar{\alpha} + \alpha_e \sin 2\pi f_e t$; $\bar{\alpha} = 12^\circ$, $\alpha_e = 0.45^\circ$ and $f_e = f_o/8, f_o/4, f_o/2$, and f_o where f_o is the inherent instability frequency of separating shear layer. Reynolds number based on mean aerodynamic chord is $Re_c = 17927$

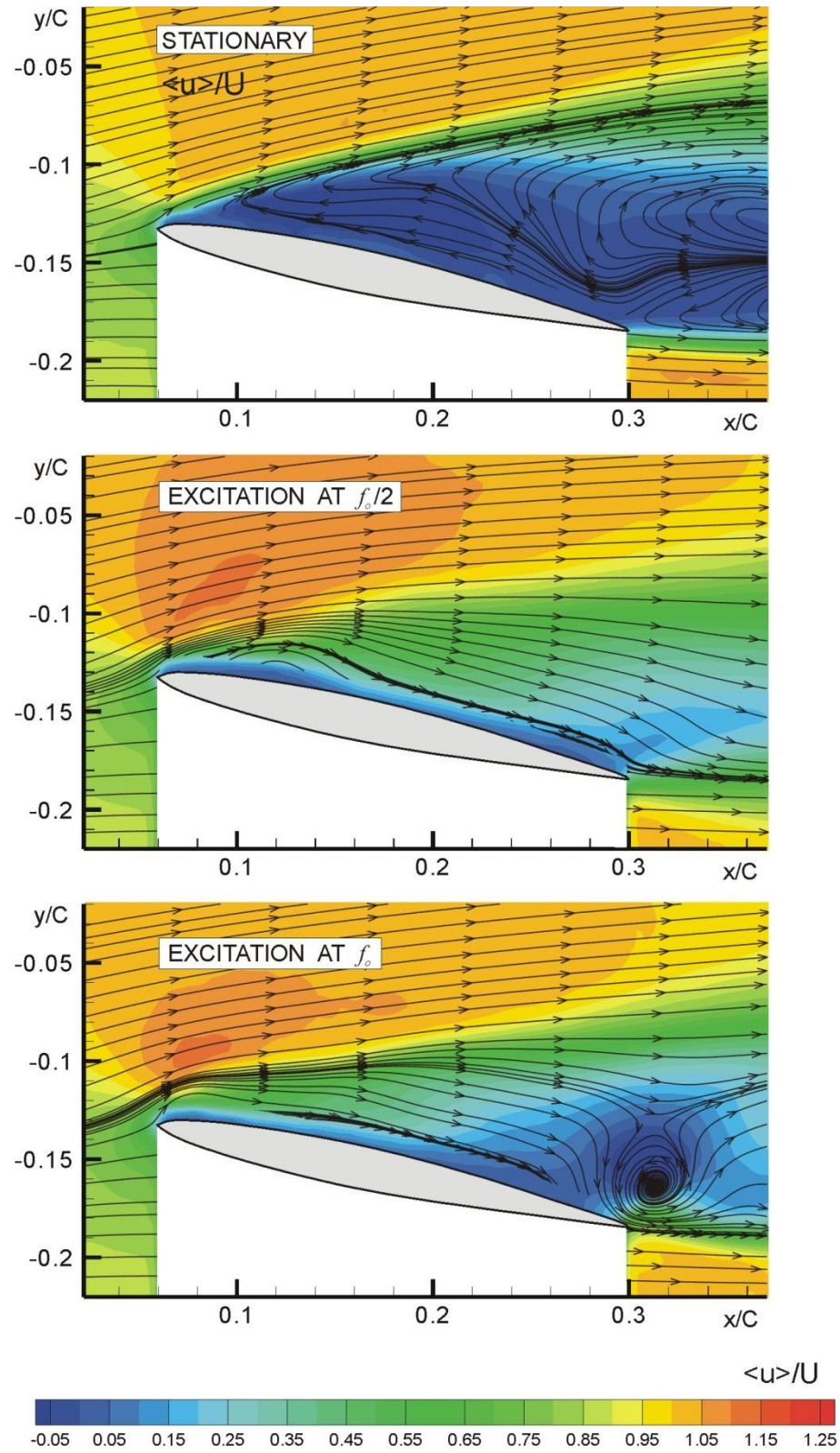


Figure A2c: Superposition of contours of constant time-averaged streamwise velocity and time-averaged streamlines for selected images given in Figure A2b.

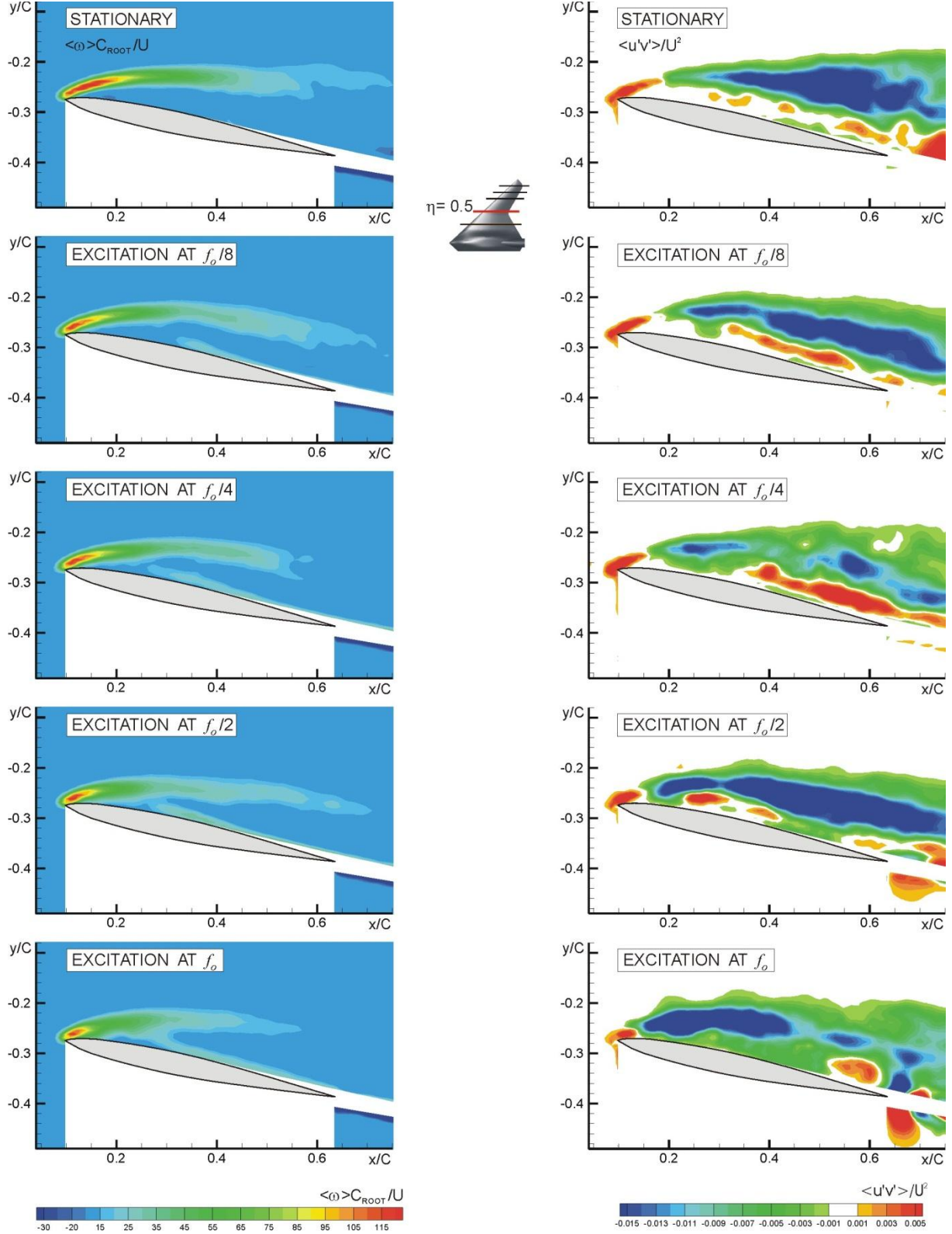


Figure A3a: Time-averaged vorticity and Reynolds stress contours for case of wing subjected to perturbations of angle-of-attack according to $\alpha = \bar{\alpha} + \alpha_e \sin 2\pi f_e t$; $\bar{\alpha} = 12^\circ$, $\alpha_e = 0.45^\circ$ and $f_e = f_o/8, f_o/4, f_o/2$, and f_o where f_o is the inherent instability frequency of separating shear layer. Reynolds number based on mean aerodynamic chord is $Re_c = 17927$

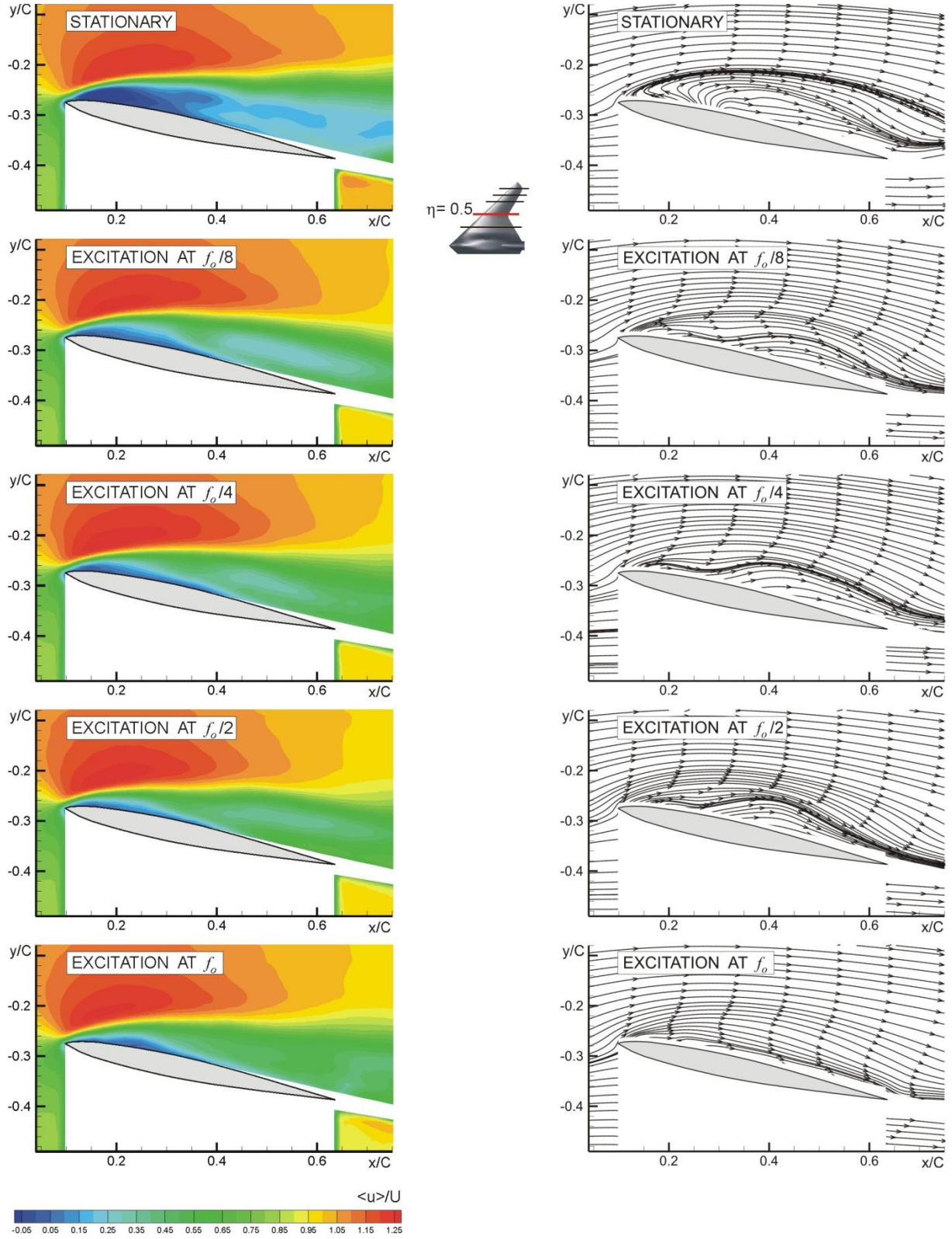


Figure A3b: Time-averaged streamwise velocity contours and streamlines for case of wing subjected to perturbations of angle-of-attack according to $\alpha = \bar{\alpha} + \alpha_e \sin 2\pi f_e t$; $\bar{\alpha} = 12^\circ$, $\alpha_e = 0.45^\circ$ and $f_e = f_o/8, f_o/4, f_o/2$, and f_o where f_o is the inherent instability frequency of separating shear layer. Reynolds number based on mean aerodynamic chord is $Re_c = 17927$

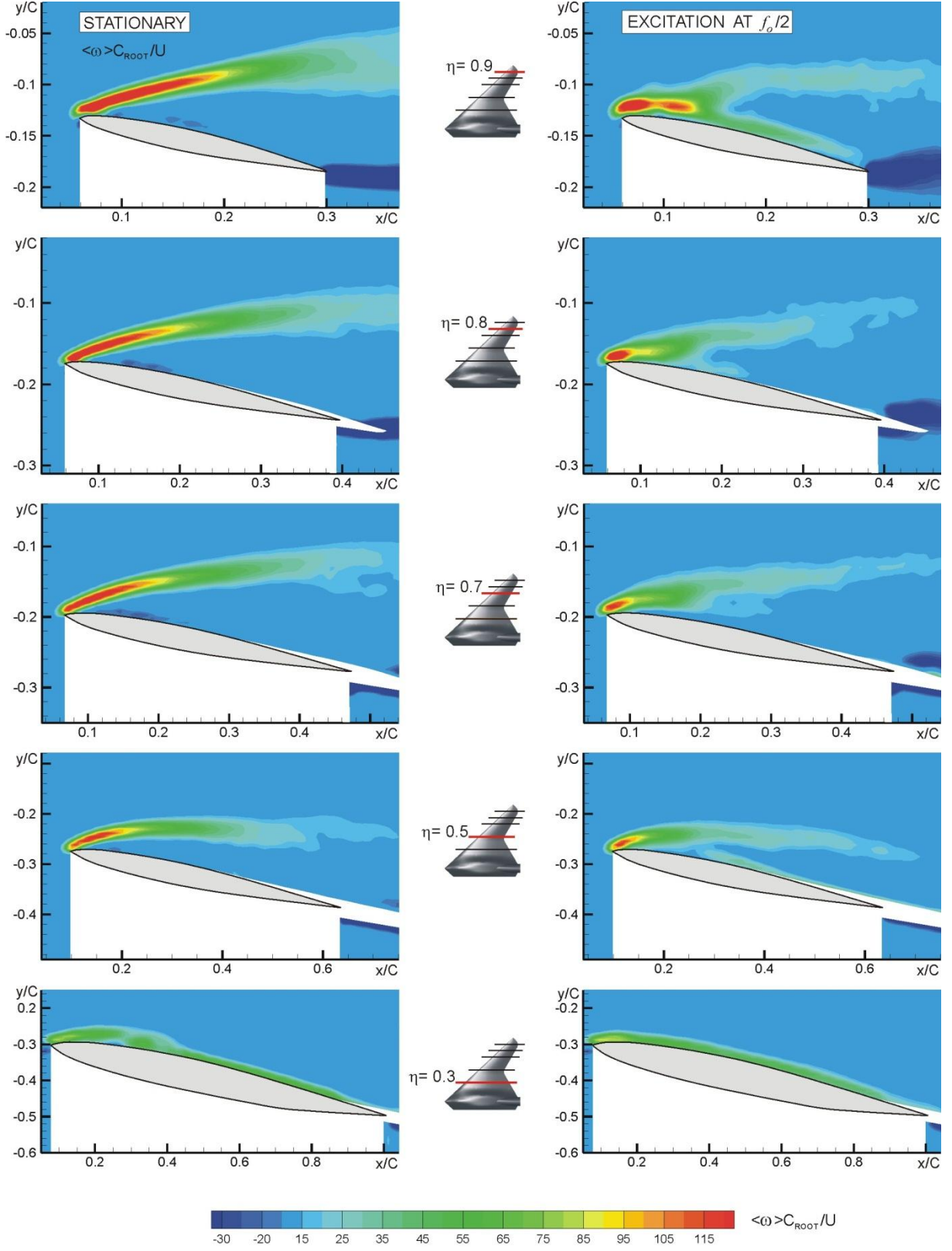


Figure A4a: Time-averaged vorticity contours for case of wing subjected to perturbations of angle-of-attack according to $\alpha = \bar{\alpha} + \alpha_e \sin 2\pi f_e t$; $\bar{\alpha} = 12^\circ$, $\alpha_e = 0.45^\circ$ and $f_e = f_o/2$, where f_o is the inherent instability frequency of separating shear layer. Reynolds number based on mean aerodynamic chord is $Re_c = 17927$

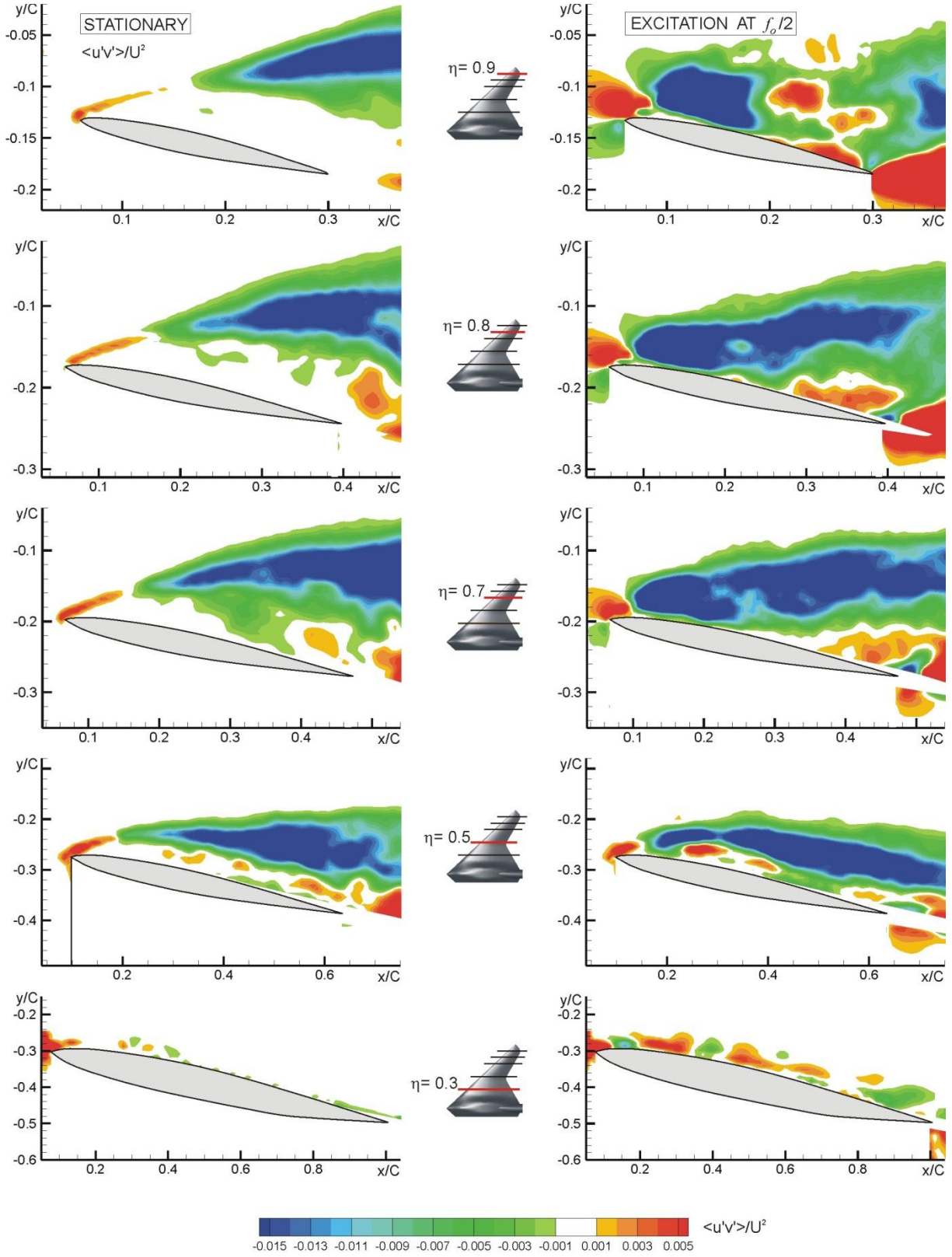


Figure A4b: Time-averaged Reynolds stress contours for case of wing subjected to perturbations of angle-of-attack according to $\alpha = \bar{\alpha} + \alpha_e \sin 2\pi f_e t$; $\bar{\alpha} = 12^\circ$, $\alpha_e = 0.45^\circ$ and $f_e = f_o/2$, where f_o is the inherent instability frequency of separating shear layer. Reynolds number based on mean aerodynamic chord is $Re_c = 17927$

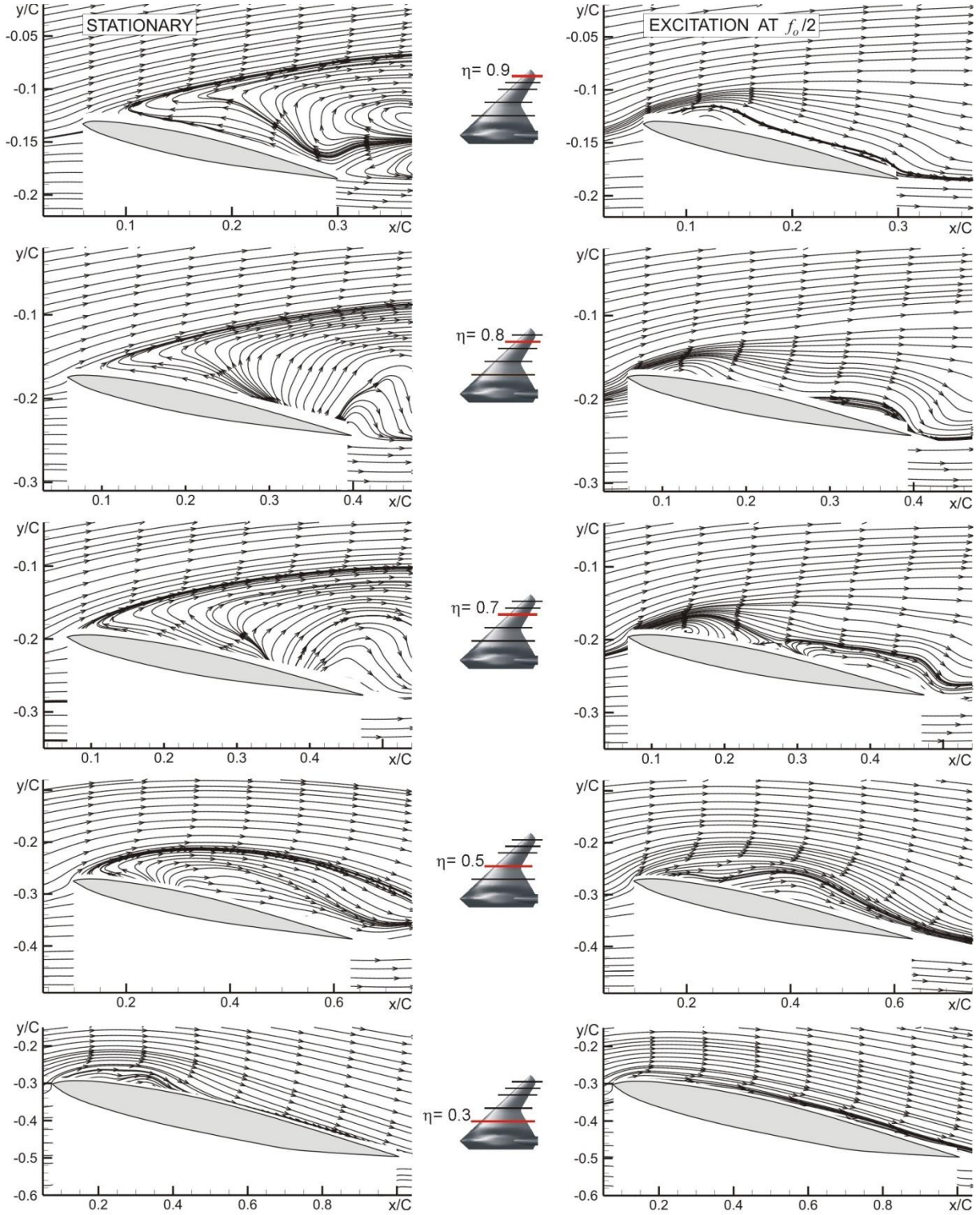


Figure A4c: Time-averaged streamlines for case of wing subjected to perturbations of angle-of-attack according to $\alpha = \bar{\alpha} + \alpha_e \sin 2\pi f_e t$; $\bar{\alpha} = 12^\circ$, $\alpha_e = 0.45^\circ$ and $f_e = f_o/2$, where f_o is the inherent instability frequency of separating shear layer. Reynolds number based on mean aerodynamic chord is $Re_c = 17927$

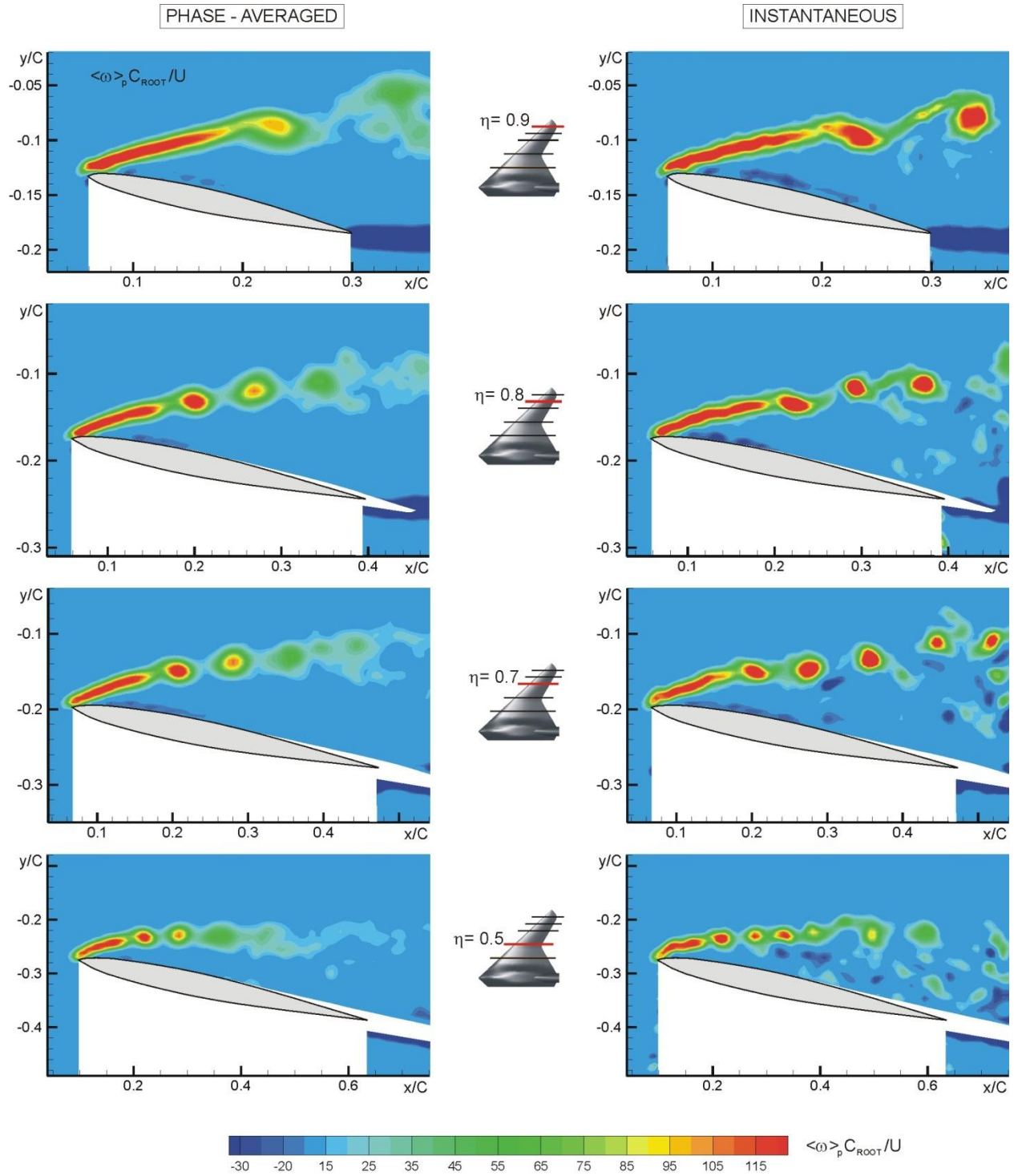


Figure A5: Patterns of phase-averaged and instantaneous vorticity on stationary wing. Reynolds number based on mean aerodynamic chord is $Re_c = 17927$

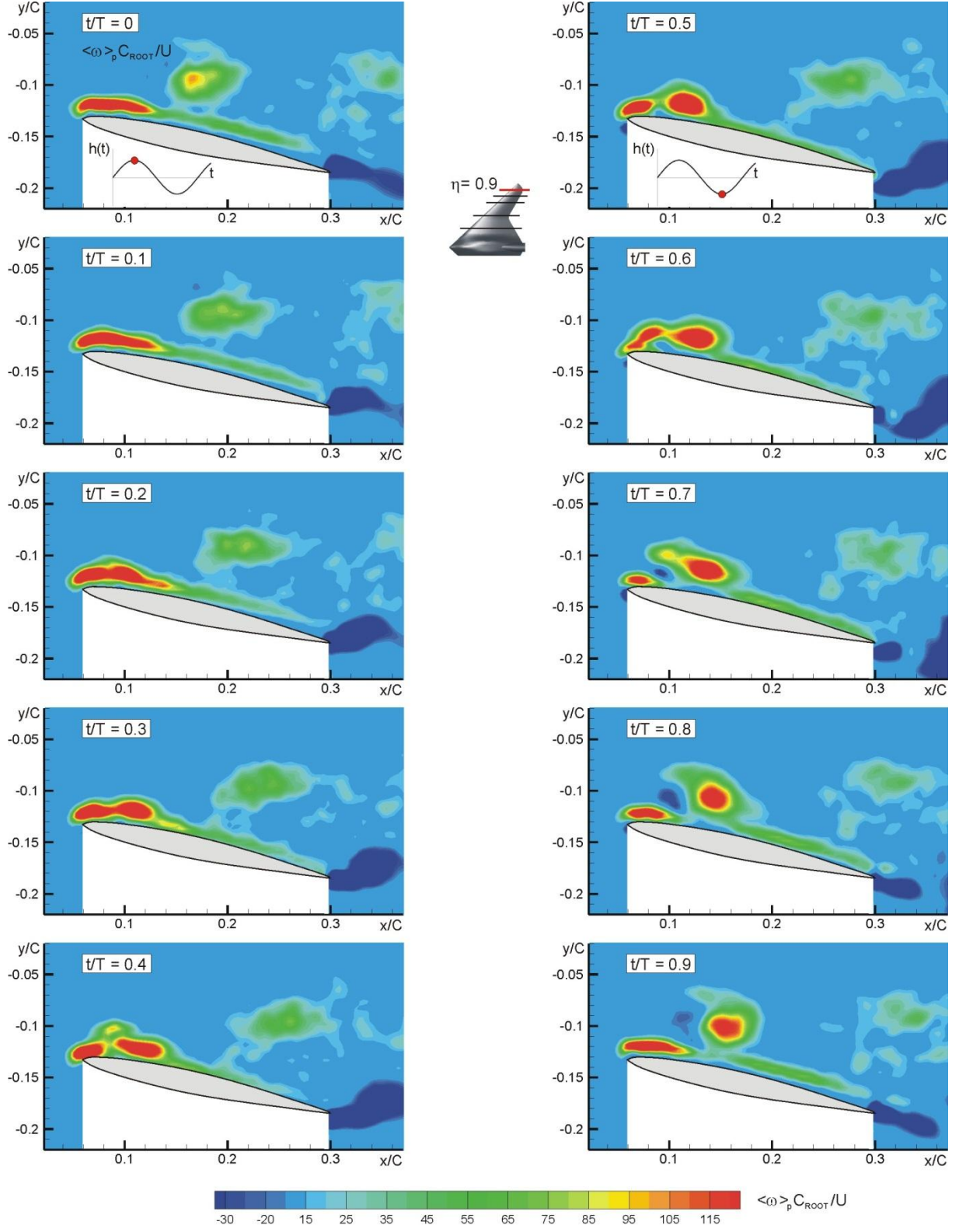


Figure A6: Phase-averaged vorticity contours for case of wing subjected to perturbations of angle-of-attack according to $\alpha = \bar{\alpha} + \alpha_e \sin 2\pi f_e t$; $\bar{\alpha} = 12^\circ$, $\alpha_e = 0.45^\circ$ and $f_e = f_o/2$, where f_o is the inherent instability frequency of separating shear layer. Reynolds number based on mean aerodynamic chord is $Re_c = 17927$

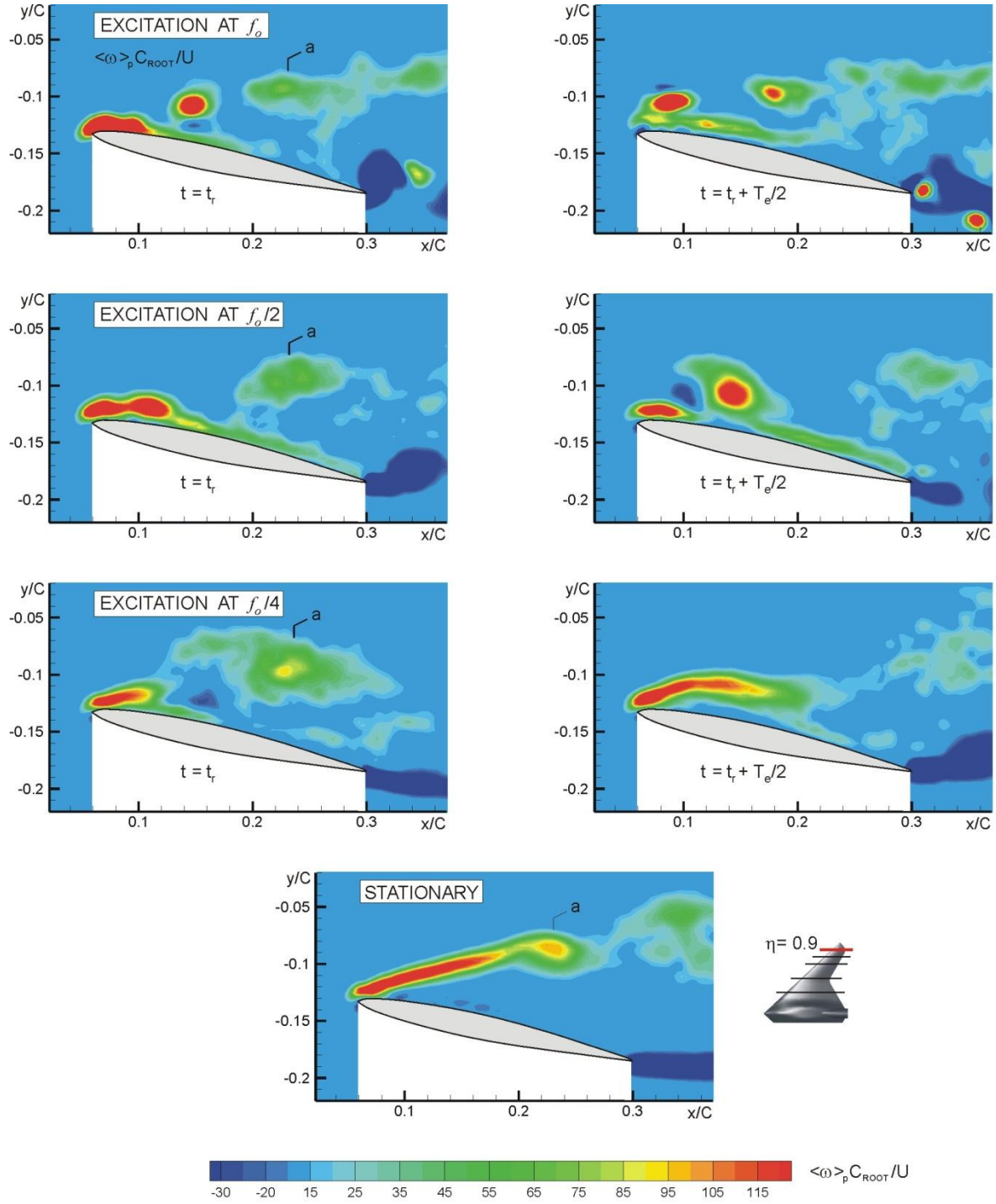


Figure A7a: Phase-averaged vorticity contours for case of wing subjected to perturbations of angle-of-attack according to $\alpha = \bar{\alpha} + \alpha_e \sin 2\pi f_e t$; $\bar{\alpha} = 12^\circ$, $\alpha_e = 0.45^\circ$ and $f_e = f_o/4, f_o/2$, and f_o where f_o is the inherent instability frequency of separating shear layer. Case of stationary wing shown for comparison. Reynolds number based on mean aerodynamic chord is $Re_c = 17927$

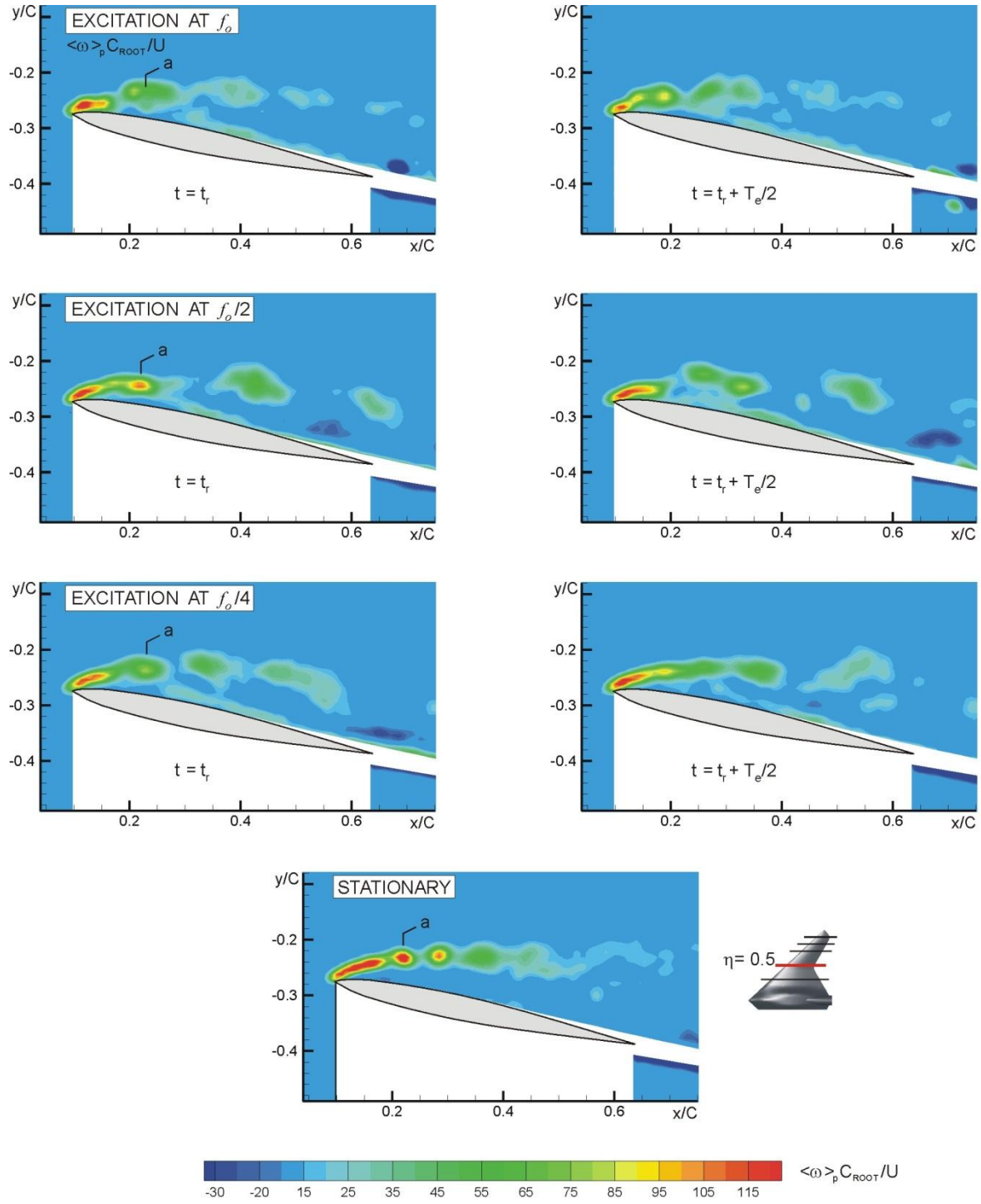


Figure A7b: Phase-averaged vorticity contours for case of wing subjected to perturbations of angle-of-attack according to $\alpha = \bar{\alpha} + \alpha_e \sin 2\pi f_e t$; $\bar{\alpha} = 12^\circ$, $\alpha_e = 0.45^\circ$ and $f_e = f_o/4, f_o/2$, and f_o where f_o is the inherent instability frequency of separating shear layer. Case of stationary wing shown for comparison. Reynolds number based on mean aerodynamic chord is $Re_c = 17927$

APPENDIX B

THREE-DIMENSIONAL FLOW STRUCTURE ON A MANEUVERING WING

ABSTRACT

Unsteady plunging (heaving) of a wing in the form of a flat plate can give rise to pronounced axial flow in the small-scale leading-edge vortex, during its initial stage of formation. Opposing axial flows along the vortex interact at the plane of symmetry, giving rise to large-scale patterns of streamwise-oriented vorticity, which can dominate the tip vortices over part of the oscillation cycle.

1. EXPERIMENTAL SYSTEM AND TECHNIQUES

Experiments were performed in a large-scale, free-surface water channel. The overall length of the test section of the channel was 5,435 mm, with a width of 613 mm and a depth of 594 mm. Upstream of this test section, a flow conditioning arrangement, along with a contraction involving arrangements of honeycomb and a sequence of five screens, provide a maximum turbulence intensity of approximately 0.3%. The freestream velocity was maintained at 90 mm/sec and the Reynolds number based on chord C was 10,000.

The wing had the form of a thin brass plate, with a chord $C = 101.6$ mm and a total span $b = 203.2$ mm, giving an aspect ratio of 2. The thickness of the plate was $t = 1.59$ mm, corresponding to $t/C = 0.016$. The leading- and trailing edges of the plate, as well as the edges of the tips of the plate were sharp and squared-off (not beveled). The plate was held in position by a thin sting mounted at mid-chord and mid-span. The maximum width of the sting was $0.016b$, and its streamwise length was $0.25C$; a cross-sectional view of the sting is given in the plan view of the schematic at the bottom of Figure B1. A complementary experiment was performed with the sting at mid-chord and quarter span; quantitative images of the flow structure across the entire span of the wing were essentially indistinguishable, within experimental uncertainty, from those associated with the mid-span location of the sting. The sting was attached to a vertically-oriented traverse table, which was driven by a high resolution stepping motor. The angle-of-attack of the plate was maintained at $\alpha = 8^\circ$. The pure plunging motion had a triangular form, involving successive positive and negative linear ramps, as illustrated in the schematics of the figures herein. The effective smoothing at the corners of the triangular function had a duration $\Delta t/T \sim 0.005$, where T is the period of the function. Zoomed-in views of the PIV imaging as well as the dye visualization showed no irregularities of the flow structure at the sensitive region of the leading-edge, e.g., generation of small-scale instabilities or vortices was not detectable, when the motion passed through a corner of the triangular function. The effects of this triangular motion are briefly compared with the corresponding sinusoidal motion. For both types of motion, the frequency and reduced frequency were respectively $f = 0.28$ Hz and $k = \pi f C/U = 1.0$. The amplitude was $h = 0.25C$, corresponding to a peak-to-peak amplitude of $0.5C$.

For the PIV experiments, the laser sheet was oriented vertically at a given value of streamwise location x/C along the plate. Independent dye marker visualization was accomplished by dye injection. Dye flowed through channels interior to the plate, then from four 1 mm holes on the leeward side of the plate. These holes were a distance of $0.0098C$ from the leading-edge, and $0.24b$ and $0.48b$ from the plane of symmetry of the plate. Two cameras were employed

simultaneously for recording dye visualization, one in the plan view (z direction) and the other in the side view ($-y$ direction).

Quantitative features of the flow structure were determined using a technique of particle image velocimetry. The location of the laser sheet is indicated in the schematics of Figure B2. The one-micron filtered water was seeded with metallic-coated hollow plastic spheres having a diameter of 12 microns, with sufficiently high density such that the interrogation window of $32 \text{ pixels} \times 32 \text{ pixels}$ typically contained a minimum of 20 particle images. The laser sheet of 1 mm thickness was generated by a dual pulsed Yag laser system having a maximum output of 90 mJ; only one-third of this available power was used during the present experiments. The pulse rate of the lasers was such that image pairs were acquired at a rate of 14.5 Hz. Images were captured using a camera with an array of $1600 \text{ pixels} \times 1200 \text{ pixels}$. The effective magnification of the camera provided a resolution in the plane of the laser sheet between 4.94 and 5.59 pixels/mm. The patterns of particle images were processed using a frame-to-frame cross-correlation technique, and a standard overlap of 50% was employed, in accord with the Nyquist criterion. As a consequence, the spatial sampling separation of the velocity data was 3.2 to 2.8 mm, yielding a maximum of approximately 7,227 velocity vectors within the field of view. The bias error of the peak vorticity of the major vorticity concentrations of interest herein, due to the spatial sampling separation, was between 0.1 to 0.4% prior to smoothing and 4 to 5% when an adaptive Gaussian window was employed, based on the assessment of Fouras and Soria (1998).

In order to determine the phase-averaged patterns shown herein, a total of twenty instantaneous images were averaged. Two cycles of the plate motion elapsed before the start of image acquisition, so these initial cycles were not included in the averaging of images. Since the flow patterns arose from a large-amplitude, controlled forcing, the instantaneous patterns were found to be relatively repetitive from cycle to cycle. Plots of vorticity magnitude versus the number of images averaged, evaluated at selected locations in the flow field, indicated that an average of ten images provided a value of phase-averaged vorticity within 0.4% of the asymptotic value.

2. VISUALIZATION AND QUANTITATIVE IMAGES OF FLOW STRUCTURE

Dye visualization was employed to illustrate the major features of the flow structure during the oscillation cycle. Figure B1 shows side and plan views of dye images at successive times $t'/T = 0$ through 0.58. Side views of the dye visualization are rotated, so that the plate is vertical, as illustrated in the schematic. The first image, at $t'/T = 0$, corresponds to attainment of the maximum positive displacement $Z(t')$. Shortly thereafter, at $t'/T = 0.08$, corresponding to the second image, the occurrence of pronounced axial flow during the initial formation of the small-scale leading-edge vortex is evident. At successively larger instants of time, the fronts of the dye marker move towards the plane of the symmetry, evident at $t'/T = 0.17$, and at $t'/T = 0.25$, there is collision of the dye fronts. Severe distortion of the visualized structures is apparent at a larger value of $t'/T = 0.42$, and at $t'/T = 0.58$, the occurrence of large-scale, elongated dye clusters is evident near the plane of symmetry of the plate; as will be demonstrated, these clusters represent streamwise-oriented vortical structures. At values of $t'/T = 0.67$ to 1.0, dye visualization (not shown herein) indicates that the pattern of streamwise vortical structures moves towards, and eventually past, the trailing-edge of the wing. At $t'/T = 1.0$, only a fraction of the originally - marked dye pattern remains upstream of the trailing-edge. The occurrence of these features can

be related to the effective angle attack $\alpha_e = 8^\circ + \tan^{-1}(\dot{y}/U)$, represented in the schematic of α_e vs. t'/T in Figure B1. At $t'/T = 0$ through 0.42 $\alpha_e = 26.4^\circ$, and at $t'/T = 0.58$, $\alpha_e = -10.4^\circ$.

Figure B2 directly compares patterns of quantitative images in selected crossflow planes with representative dye visualization images. The top set of images of Figure B2 is on the plane at $x/C = 0.2$, at the instant $t'/T = 0.017$. Contours of constant transverse velocity v are normalized by the freestream velocity U , i.e. v/U . The maximum value of $v/U = 0.73$. The bottom set of images are on the plane at $x/C = 0.7$, at the instant $t'/T = 0.58$. The contours of normalized transverse velocity v/U exhibit maxima located closer to the plane of symmetry of the wing, relative to the maxima at $x/C = 0.2$. In addition to the predominant contours of v/U adjacent to the surface of the plate, for which the maximum value of $v/U = 0.67$, secondary contours appear above them, due to the rotational motion of the streamwise-oriented vortices. Corresponding contours of constant vorticity $\omega C/U$ are also shown in the right column of images. At this instant, the scale and circulation of these larger-scale concentrations dominate the tip vortices.

The very rapid evolution with time of the streamwise-oriented vortical structures near the plane of symmetry is shown in the images of Figure B3. These images correspond to the relatively close instants of time $t'/T = 0.5$ and 0.67, located on the plane at $x/C = 0.7$. The abrupt change of the flow structure involves, first of all, a reduction to zero of the scale and strength of the tip vortices, which is evident in the patterns of velocity vectors \underline{V} , contours of constant v/U , and contours of constant vorticity $\omega C/U$ at $t'/T = 0.67$. Moreover, the scale and strength of the counter-rotating vortex system located at the plane of symmetry rapidly increases in going from $t'/T = 0.5$ to 0.67, as indicated by the contours of $\omega C/U$. As shown in the patterns of velocity vectors \underline{V} , the associated swirl increases as well.

Figure B4 provides a comparison of selected aspects of the flow structure for the foregoing motion of the plate and the corresponding sinusoidal motion. The top set of images shows that the form of contours of constant transverse velocity v/U in the region close to the leading- edge is preserved, though it is slightly shifted in time t'/T . Moreover, the bottom row of images indicates that, at a downstream location where the streamwise vortices have developed, the form and location of the pronounced concentrations of streamwise vorticity $\omega C/U$ are similar; sinusoidal motion results in even larger circulation. For the triangular motion, at $t'/T = 0.17$ and 0.67, the effective angle attack $\alpha_e = 8^\circ + \tan^{-1}(\dot{y}/U)$ is 26.4° , and -10.4° respectively, and for the sinusoidal motion at $t'/T = 0.25$ and 0.67, $\alpha_e = 34.7^\circ$, and -16.1° .

In summary, the timewise development of the patterns of dye given in Figure B1 show the transformation from pronounced axial flow in the nascent leading-edge vortex to well-defined, streamwise-oriented vortical structures located near the plane of symmetry of the wing, clarified by the quantitative images of Figure B2. Moreover, the images of Figure B3 emphasize that abrupt changes of the three-dimensional flow structure can occur over a small time scale, i.e., a fraction of the oscillation cycle. Figure B4 shows that the existence and form of principal features of the flow structure are preserved for two basic types of motion: successive positive-negative ramps; and sinusoidal motion. This type of three-dimensional vortex formation is expected to be a generic feature of wings undergoing unsteady rectilinear maneuvers in various modes, where significant accelerations of the leading-edge lead to generation of a pronounced leading-edge vortex.

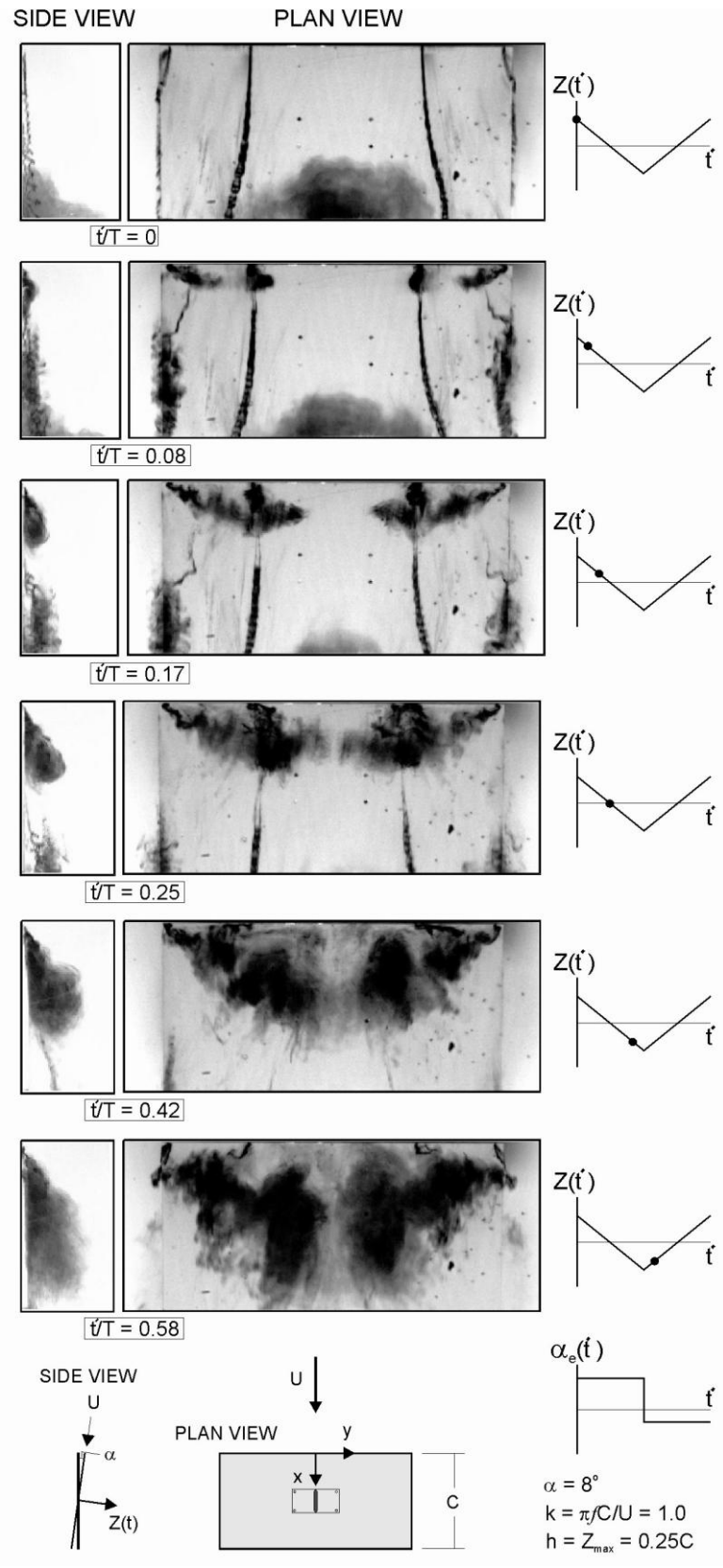


Figure B1 : Dye visualization of three-dimensional vortex formation

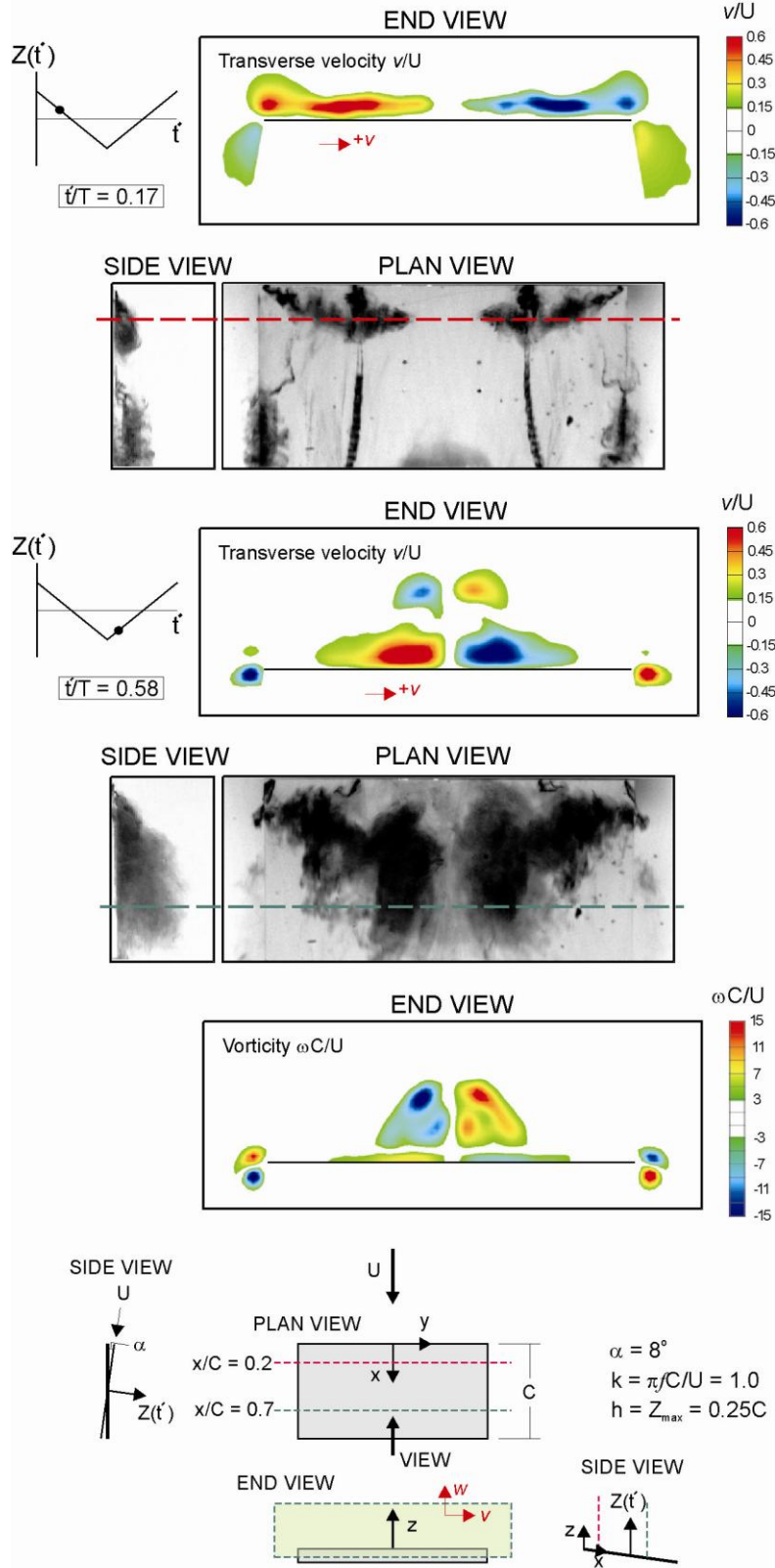


Figure B2 : Dye visualization of three-dimensional vortex formation in relation to images in cross-flow planes

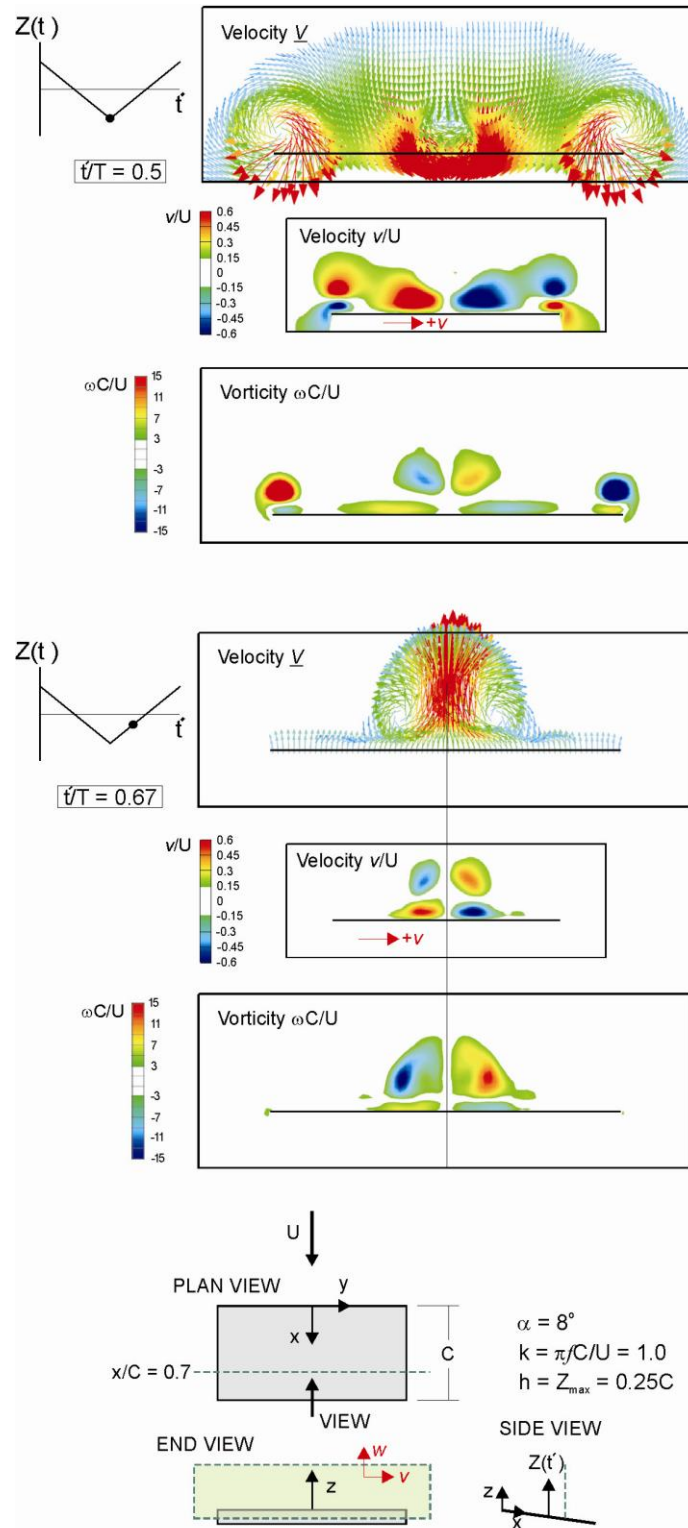


Figure B3 : Images in cross-flow plane at two successive instants of time

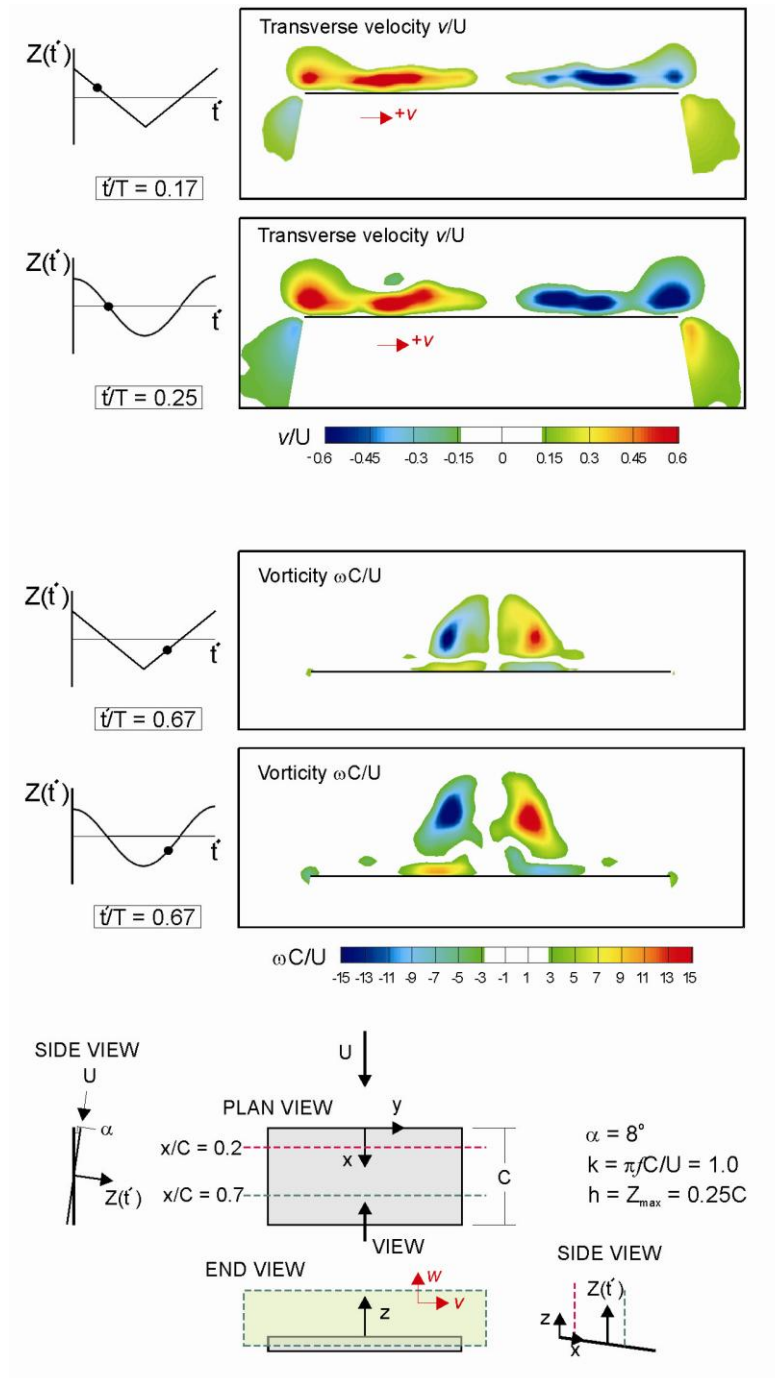


Figure B4 : Effect of type of plunging motion on flow structure

APPENDIX C

SCALING OF FLOW SEPARATION ON A PITCHING LOW ASPECT RATIO PLATE

ABSTRACT

We use two different dye injection approaches, in two different water tunnels, to visualize the formation and subsequent evolution of leading-edge vortices and related separated structures, for a pitching low aspect ratio plate. The motion is a smoothed linear pitch ramp from 0° to 40° incidence, brief hold, and return to 0° , executed at reduced pitch rates ranging from 0.1 to 0.35 and about various pivot locations. All cases evidence a leading edge vortex with pronounced axial flow, which leads to formation of large-scale, three-dimensional flow structures, culminating in a large vortical structure centered at the wing symmetry-plane. Pitch is also compared to plunge, whereby the functional form of the plunging motion provides an equivalent variation of angle of attack with time that matches the pitching motion. At successively increasing values of time, represented by the convective time scale C/U , the three-dimensional patterns of the flow structure are remarkably similar for the pitching and plunging motions. The similarity of these patterns persists, though they are shifted in time, for variation of either the location of the pitching axis or the dimensionless pitch rate.

1. EXPERIMENTAL METHODS

Experiments were performed in free surface water tunnel facilities at Lehigh University and the US Air Force Research Laboratory. Details of these facilities and the associated wing motion rigs are given by Yilmaz and Rockwell (2010) and Ol et al. (2005), respectively. Both used an aspect ratio 2.0 rectangular flat plate with all edges of nominally semicircular contour. A schematic of the wing and definition of related parameters are given in Figure C1a.

The facility at Lehigh University had a test section 508 mm deep and 613 mm wide, and for the present experiments, was operated in the range of freestream velocity of $U = 45$ to 90 mm/s, with a turbulence intensity of 0.2%. The wing had a total span $b = 203.2$ mm, chord $C = 101.6$ mm, and thickness of 1.59 mm. Maximum blockage based on wing streamwise projected area was 4.3% at 40° incidence. The plate was supported by a vertical sting in the form of a thin plate of chordwise length of $0.27 C$ and a thickness of $0.019 b$. The sting was attached to the plate at its mid-span and mid-chord location. Pitching motion was achieved by a small chain of thickness $0.019 b$ about the periphery of the sting plate, and connected to a computer-controlled motor at the top of the sting. Simultaneous horizontal and vertical translation was achieved by computer-controlled traverse tables. An arbitrary streamwise location of the pitch pivot point could therefore be prescribed. Dye (35% blue food coloring and 65% water) was gravity-fed from a single plastic tube connected to the wing surface, then through six channels within the wing. Dye ports of diameter 1 mm were drilled into the leeward side of the wing at spanwise locations ± 48 mm, ± 96 mm, and ± 100.6 mm measured from the plane of symmetry of the wing. These locations correspond respectively to distances from the plane of symmetry of 47%, 94%, and 99% of the semi-span $b/2$. The four inboard dye ports were located at a distance of 1 mm from the leading-edge of the wing, and the two outboard ports, which were essentially coincident with the tip of the wing, were at a distance of 10mm from the leading-edge. Side and plan views of the visualized patterns of the flow were recorded simultaneously using two CCD

cameras. Experiments were performed at freestream velocities of $U = 45$ and 90 mm/s, giving Reynolds numbers based on chord of $Re = 5,000$ and $10,000$.

The facility at the US Air Force Laboratory (AFRL) is a free-surface water tunnel of 4:1 contraction and 46cm wide by 61cm high test section, with turbulence intensity estimated at 0.4%, and a surface skimmer to damp sloshing. The tunnel is fitted with a three degree of freedom electric rig enabling independent control of pitch or rotation, plunge or heave, and “surge” or streamwise-aligned translation. The rig is controlled through a Galil DMC 4040 Ethernet controller. Pitch and plunge are made possible by a pair of motors mounted vertically on a plate above the tunnel test section. Each motor actuates a vertical “plunge rod”, which connects via a bushing to a coupler piece. The upstream plunge rod is constrained to move purely vertically, whereas the downstream plunge rod is allowed to swing in the test section vertical plane of symmetry. The pitch pivot point can be varied by suitable choice of phase and amplitude difference in trajectory of the two vertically-mounted motors. For all cases where the pitch pivot point is not coincident with the bushed end of the front plunge rod, there will be a parasitic streamwise displacement of the model. This is removed using the third degree of freedom, surge, using a larger linear motor mounted horizontally aft of the pitch-plunge carriage.

The model is a carbon-fiber plate of nominally 3mm thickness, 234 mm span and 117 mm chord and rounded (semicircular) edges. It was supported by an aft-mount sting with nominal diameter of 0.085C; in essence, this sting was an extension of the trailing-edge of the plate, which was centered at the plane of symmetry of the plate. Dye is injected from four 0.5mm-diameter steel-tube probes running along the model surface and exiting at the leading edge, firing in the spanwise direction. The probes exiting at the spanwise centerplane and the spanwise 87.5% plane are mounted along the model’s pressure-side. Two other probes, exiting at the spanwise 75% plane and the 97.5% spanwise location (6mm away from the wingtip), are mounted along the model’s suction-side. All probes connect to a plenum fed through a common syringe, actuated by a programmable pump set to 1 mL/minute infusion volumetric rate. Dye consists approximately of 60% blue food coloring, 20% rubbing alcohol and 20% “half and half” cream, by volume. The nominal Reynolds number of the experiment was 10,000, at a tunnel free-stream speed of 85 mm/s, in water at 21°C. Test section geometric blockage at the maximum angle of attack is 6.3%, based on the model’s projected frontal area.

The wing (plate) motion in both laboratories is shown in Figure C1b. The pitching motion is a linear pitch up-pitch down sequence followed by a hold at zero angle of attack, with smoothing at the motion extrema to avoid structural excitations. For plunging motion, the functional form of the vertical displacement h of the wing was formulated such that the equivalent angle of attack θ_{eq} during plunging corresponded to the geometrical angle of attack θ during the pitching motion, neglecting the effects of pitch rate. That is:

$$\arctan \frac{\dot{h}(t)}{U_{\infty}} = \theta_{eq}(t) \quad (1)$$

Therefore, at a given value of time $t = C/U$ in the schematic of Figure C1, $\theta_{eq} = \theta$.

2. RESULTS

2.1 PATTERNS OF LEADING-EDGE VORTEX FORMATION FOR PITCH ABOUT THE QUARTER CHORD

Figure C2a directly compares the development of the flow patterns using the two different visualization techniques. Images in the left column are at $Re = 5,000$, and in the right column, at $Re = 10,000$. Each data set show side and plan views. The instantaneous angle of attack is indicated by the dot on the schematic of the pitching schedule (θ versus time t) given in the right column.

In the first row of images of Figure C2a, corresponding to $\theta = 20^\circ$ on the upstroke, both the side and plan views indicate lack of detectable formation of a leading-edge vortex. Subsequently, at $\theta = 40^\circ$, as indicated in the second row of images, a small vortex is evident in the side views. The corresponding plan views show inboard-oriented axial flow through the center of the leading-edge vortex towards the plane of symmetry of the wing. In the third row of images, at $\theta = 20^\circ$ on the downstroke, the side view of the leading-edge vortex shows a substantial increase in scale and, correspondingly, the plan view shows that the pattern of axial flow through the leading-edge vortex has reached the plane of symmetry. At the end of the downstroke, $\theta = 0^\circ$, in the fourth row of images, the three-dimensional vortex has matured to a larger scale and undergone substantial distortion, evident in both the plan and side views. Finally, in the fifth row of images, the dye marking the large-scale vortex has evolved to a confined cluster concentrated at the plane of symmetry of the wing, which suggests that vorticity marked by the dye during the earlier stages of formation now resides in that region as well. The plan view image in the fifth row, right column, shows extension of the dye marker to further upstream locations than the corresponding image in the left column, apparently due to the continuous injection of dye along the plane of symmetry and, perhaps, an influence of the sting extension from the trailing-edge. Generally speaking, however, for all of the images in the right column at $Re = 10,000$ versus the left column (at $Re = 5,000$) of Figure C2a, the patterns are quite similar, thereby suggesting an insignificant influence of Reynolds number in this range. Differences can be ascribed to the intensity of the dye injection; that is, the extent to which the dye flow itself is intrusive in the local flowfield. When the flow is instantaneously nearly attached, dye flow intrusion can be significant. But large vortical structures subsume all discernable effects of how the dye happens to be introduced.

The dye patterns of Figure C2a show distinctive stages of evolution of the flow structure, during the pitch up-pitch down motion of the wing. We now consider the extent to which these patterns persist for variations of pitching axis location and reduced pitching rate, and for plunge vs. pitch.

2.2 COMPARISON OF PITCH AND PLUNGE

The functional form of plunging generated an effective instantaneous angle of attack θ_{eq} equal to the angle of attack θ of the pitching motion of the wing. This equivalence is shown in Figure C1 and defined in eqn. (1). Figure C2b shows images associated with the equivalent pitching motion. The instantaneous vertical displacement h and the equivalent angle of attack θ_{eq} of the plunging motion are indicated respectively by filled and open dots on each of the schematics in the right column of Figure C2b. The instantaneous, effective angle of attack θ_{eq} is indicated on each plan view. Each image in Figure C2b can be directly compared with the image

at the corresponding location in Figure C2a. In an overall sense, the patterns of Figure C2b are remarkably similar to their counterparts in Figure C2a. The onset of vortex formation from the leading-edge, characterized by pronounced axial flow at $\theta = 40^\circ$ in Figure C2a and $\theta_{eq} = 40^\circ$ in Figure C2b, is nearly indistinguishable. At later times, corresponding to the third through fifth row of images, the pivot $x_p/C = 0.25$ dye patterns are displaced slightly further in the downstream direction and are somewhat distorted relative to the patterns indicated for the plunge case, as indicated in the plan views. The side views in the fourth row of images show that the elongated dye cluster is inclined at a shallower angle with respect to the surface of the wing for the pivot $x_p/C = 0.25$ case, relative to the plunge case. All of these features are discernible distinctions that occur along downstream portions of the wing, which are not accounted for in the angle of attack equivalence between these motions. Nevertheless, as shown in the fifth row of images, which represents the end state, the spatial extent and position of the dye cluster concentrated near the trailing-edge is quite similar for pivot $x_p/C = 0.25$ and plunge. In summary, the angle of attack equivalence between the pitching and plunging motions yields a strong correlation of the overall form and phase shift of the initial stage of vortex formation for these distinctively different types of wing motion.

2.3 EFFECT OF PITCH POINT LOCATION AND PITCH RATE

Figure C3 shows a comparison of pitch pivot point effects. In all cases, $Re \sim 10,000$ and $K = 0.35$. The pitch pivot point locations are $x_p/C = 0.00$ (leading edge), 0.25, 0.50, 0.75 and 1.00 (trailing edge); plunge is also compared. The leading-edge pivoting case is taken as a reference case, where we consider the flowfield snapshot at maximum angle of attack; that is, at the top of the pitch ramp. The leading-edge vortex (LEV) occupied approximately the forward third of the wing suction-side, and strong inboard flow is seen in the planform view. We assert a flowfield similarity relationship as follows: for a given pitch rate, for any two choices of pivot point location, one can find a snapshot of motion history for the one and for the other, such that the LEV development will be similar. This does not hold for late in the motion history, long after the pitch ramp peak has been passed. But as seen in, for quarter-chord pitch, the LEV development sometime along the downstroke (instantaneous incidence angle $\sim 31.5^\circ$) is much akin to that of the leading edge pivot case at $\theta = 40^\circ$. For half-chord pivot, the relevant point is 27.7° on the downstroke; for $3/4$ -chord pivot, it is 24.6° ; for trailing-edge pivot, 22.6° ; and for the plunge, it is 33.2° .

It is conceptually attractive to surmise that there is a special choice of pivot point, such that pitch about that point would be “equivalent” to plunge. To make a proper comparison of course requires force time history and quantitative flowfield history. But qualitatively, it appears that the quarter-chord is a reasonable approximation for such a “special” point.

Figure C4 compares images for a given location of the pitch pivot point $x_p/C = 0.25$, i.e., at quarter-chord, for different values of reduced pitch rate $K = c\dot{\theta}/2U_\infty = 0.1, 0.2$, and 0.35 . The reference pattern of the LEV development is taken to occur at the maximum angle of attack $\theta = 40^\circ$, i.e., at the top of the pitch motion, for $K = 0.2$. With the hypothesis that the LEV pattern exhibits similarity at different values of K , examination of movies yielded the LEV patterns at the values of angle of attack θ and reduced frequency K indicated in Figure C4. In essence, the effect of increasing K is to advance occurrence of the LEV pattern to smaller values of C/U , but to delay it along the indicated pitching schedule.

3. CONCLUDING REMARKS

The major features of the flow structure on an aspect ratio of 2 rectangular wing executing constant-rate pitch-up followed by pitch-down are remarkably similar for variations of pitch point location and reduced frequency extending over the range from $K = 0.1$ to 0.35 . Such variations simply induce a shift in time of occurrence of the sequence of three-dimensional flow separation events. This time shift is represented by a reference flow structure, i.e., the three-dimensional form of the leading-edge vortex (LEV), during the late stage of its formation. As the pitch point is moved from the leading-to the trailing-edge of the wing, the appearance of the LEV is delayed by the order of one-half convective time scale C/U . When the reduced frequency is increased by a factor of 3.5, the LEV is advanced in time by a factor of approximately $2C/U$.

Comparison of pitch and plunge, whereby the equivalent angle of attack of plunge is matched to the angle of attack of pitch, again shows that the sequence of three-dimensional flow events is well correlated at successive times. The flowfield in a plunging maneuver is very similar to that of pitch about the quarter-chord.

We find evidence, therefore, of a universality of time scale of flowfield evolution, which can generalize across a range of motion rates and type of kinematics. It remains to consider whether the history of aerodynamic forces may obey a scaling akin to that of the flowfield.

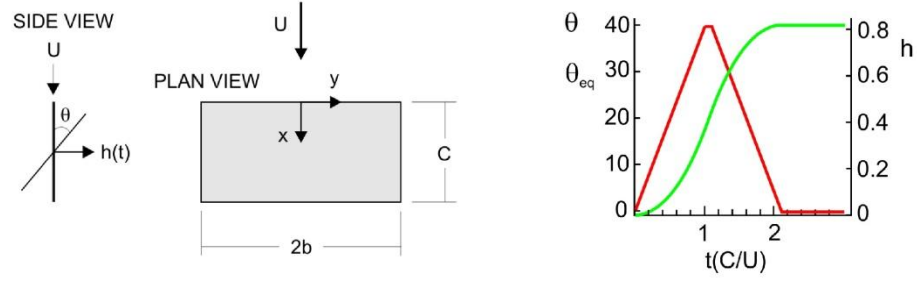
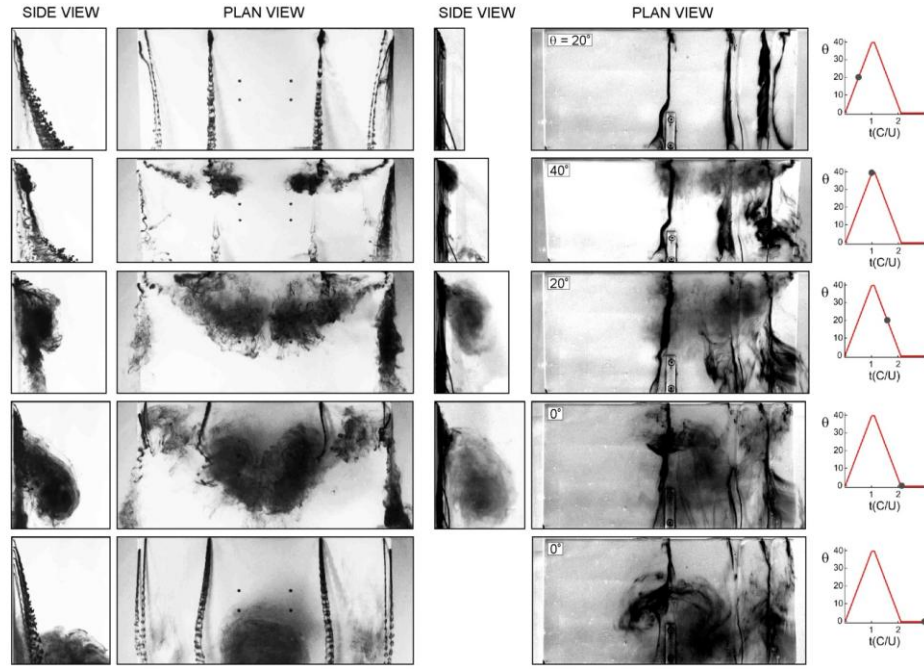


Figure C1 : (a) Schematic of wing (rectangular flat plate) and associated terminology; (b) variation of angle of attack θ of pitching motion, equivalent angle of attack θ_{eq} of plunging motion, and displacement h of plunging motion, which has been normalized by the chord C . Pitching motion corresponds to $K = 0.35$.

(a)



(b)

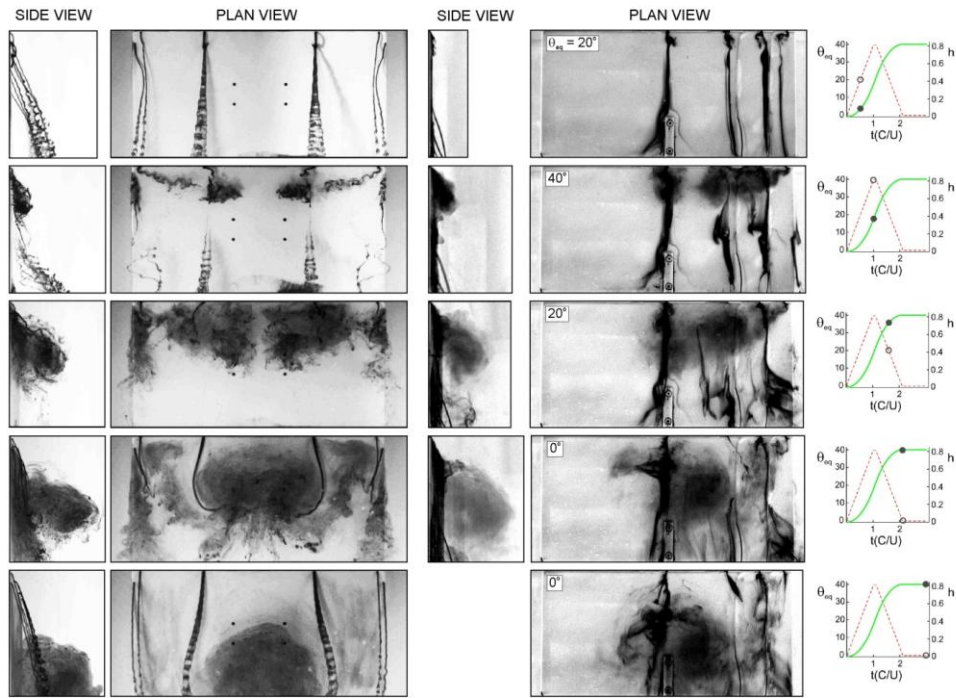


Figure C2 : (a) Side and plan views of onset and development of vortex structure during pitch up- pitch down motion using dye visualization at LU (left column, $Re = 5,000$) and AFRL (right column, $Re = 10,000$). Pitch point $x_p/C = 0.25$ and $K = 0.35$. (b) Side and plan views of onset and development of vortex structure during plunging motion using dye visualization at LU (left column, $Re = 5,000$) and at AFRL (right column, $Re = 10,000$). Pitch point $x_p/C = 0.25$ and $K = 0.35$.

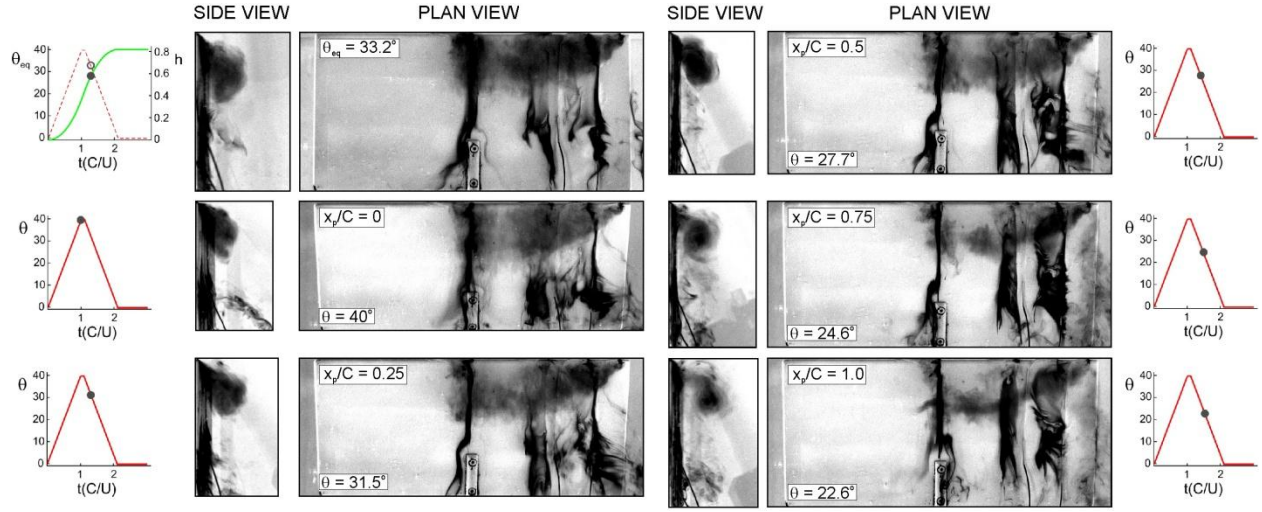


Figure C3 : Side and plan views of AFRL dye injection, $Re = 10,000$, $K = 0.35$. Plunge is represented by the set of images at the top left, followed by pitch pivoting at $x_p/C = 0, 0.25, 0.5, 0.75$, and 1.0 .

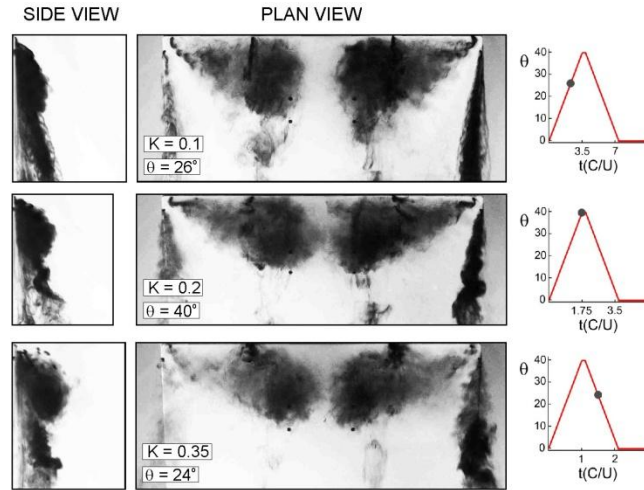


Figure C4 : Side and plan views of LU dye visualization showing effect of magnitude of reduced frequency $K = 0.1, 0.2$ and 0.35 on vortex structure. Pitch pivot point $x_p/C = 0.25$, $Re = 10,000$.

APPENDIX D

CONTROL OF VORTICAL STRUCTURES ON A FLAPPING WING VIA A SINUSOIDAL LEADING EDGE

ABSTRACT

The flow structure generated by a flapping wing in the form of a plate is fundamentally altered if the leading-edge has a sinusoidal shape. It is possible to attenuate both the positive and negative spanwise flow along the plate surface, as well as the onset and development of large-scale concentrations of positive and negative streamwise vorticity at inboard locations. These alterations of the inboard flow structure have an insignificant influence on the structure of the tip vortex.

1. EXPERIMENTAL SYSTEM AND TECHNIQUES

Experiments were performed in a free-surface water channel, which had a depth of 610 mm, a width of 927 mm and a test section length of 4877 mm. In order to maintain the turbulence intensity at a value below 0.5%, extensive conditioning of the upstream flow involved use of a honeycomb system, followed by an arrangement of five sequential screens. The freestream velocity U was maintained at a value of 25.4 mm/s. The geometry of the flapping wing is illustrated in the schematics at the top of Figure D1.

A wing in the form of a rectangular flat plate having a chord $C = 50.8$ mm and a span $b = 101.6$ mm was mounted on a body of revolution having a diameter $D = 12.7$ mm. The thickness of the wing was $d = 1.59$ mm, and all of its edges, including the sinusoidal leading-edge, were sharp with no bevel. The wing was inclined at an angle of attack of 8 (degrees) with respect to the freestream, throughout the oscillation cycle. The Reynolds number based on chord C was $Re = 1300$, which yielded highly coherent streamwise-oriented vortical structures and, furthermore, corresponded to adequate temporal resolution of the quantitative imaging.

The end view schematic at the top of Figure D1 defines the instantaneous angle ϕ during the flapping motion. This angle varied in a periodic manner between maximum positive and negative values $\phi_{max} = \pm 30^\circ$. This angular variation had a triangular (sawtooth) form, involving a succession of positive and negative ramps, as defined in Figure D1. The wing therefore had zero acceleration except at the corners of the triangular motion, where the smoothing function had a duration $0.015 \Delta t/T$; T is the period of the flapping motion. The dimensionless frequency of oscillation was $K = \pi f C/U = 0.3$. This controlled motion of the wing is intended to represent a generic wing rotation that generates the highly coherent vortical structures in presence of substantial spanwise gradients.

The leftmost schematic at the top of Figure D1 shows the plate with the straight leading-edge; the corresponding plate with the sinusoidal leading-edge is shown in the right schematic. The amplitude A of the sinusoidal leading-edge normalized by the chord C was $A/C = 0.098$, and the corresponding dimensionless wavelength between neighboring peaks was $\lambda/C = 0.246$. Optimization of these parameters has not yet been addressed. It should be noted that Darekar and Sherwin employed different scaling of the amplitude and wavelength for flow past a wavy bluff body and, coincidentally, their values are generally compatible with the present values.

A technique of particle image velocimetry(PIV) was employed to determine quantitative features of the flow structure in the crossflow plane. Filtered water was seeded with 12 μm diameter metallic-coated hollow plastic spheres. A pulsed Yag laser system, operating at an output of 50 mJ, and at a repetition rate of 14.29 Hz, generated a laser sheet of 1 mm thickness after passing the mean through a system of spherical and cylindrical lenses. Images were acquired at a rate of 14.29 image pairs per second with a camera having a CCD array of $1,600 \times 1,200$ pixels². The effective magnification was 12.4 pixels/mm. Patterns of particle images were evaluated using a frame-to-frame cross-correlation technique with a standard 50% overlap, in accord with the Nyquist criterion. Approximately 7,227 velocity vectors were generated with a spacing of 1.29 mm.

2. FLOW STRUCTURE ON FLAPPING WING

Figure D1 shows images corresponding to the flapping plate with a straight leading-edge (left column) and the sinusoidal leading-edge (right column). By examining the sequence of PIV images for the case of the straight leading-edge with time, i.e., images at sequential values of $\phi(t)$, it was found the angle $\phi = 13.3^\circ$ during the downstroke motion corresponded to the largest-scale vortical structures at inboard locations. Consequently, the value of $\phi = 13.3^\circ$ is employed for comparison of the flow structure along plates having straight and sinusoidal leading-edges. For this selected flapping angle ϕ , the effective angle-of-attack is $\alpha_e = \alpha_0 + \tan^{-1}V_t/U = 30.7^\circ$ at the tip of the wing, where $\alpha_0 = 8^\circ$ is the static angle of attack, $V_t = 10.64$ mm/s is the tangential tip velocity of the flapping wing and $U = 25.4$ mm/s is the freestream velocity.

The first row of images in Figure D1 directly compares zoomed-out images of the streamwise vorticity ω_x at a streamwise location immediately downstream of the leading-edge, i.e., $x/C = 0.1$. For the case of the straight leading-edge, represented in the left column, a very thin layer of negative vorticity is evident. For the case of the sinusoidal leading-edge, shown in the right column, an ordered pattern of small-scale streamwise vorticity ω_x is evident. That is, the nonuniform leading-edge provides an ordered array of small-scale, streamwise oriented vortical structures in the immediate vicinity of the leading-edge region.

The second row of images of Figure D1 shows patterns of streamwise vorticity ω_x at the streamwise location $x/C = 0.5$. The image in the left column corresponding to the straight leading-edge, indicates a well-defined tip vortex and, in addition, positive and negative concentrations of ω_x at an inboard location. The corresponding image for the case of the sinusoidal leading-edge at $x/C = 0.5$ indicates a very similar tip vortex as for the straight leading-edge, but the large-scale vortex system located inboard is not evident. Rather, small-scale, relatively weak streamwise vortices are detectable.

In the third row of images of Figure D1, patterns of streamlines further clarify the existence and nonexistence of the vortical structures at inboard locations for the cases of the plates with straight and sinusoidal leading-edges. That is, for the case of the straight leading-edge, two swirl patterns of streamlines are bounded on the upper and lower sides by saddle points, in accord with the positive and negative concentrations of ω_x . On the other hand, for the case of the sinusoidal leading-edge, only very mild distortions of the streamlines are evident along the upper surface of the plate.

A key feature of the flow pattern along the flapping plate with a straight leading-edge is the existence and magnitude of spanwise flow from the root to the tip of the wing, which is represented by contours of constant transverse velocity v/U in the bottom row of images of

Figure D1. For the case of the plate with the straight leading-edge, large magnitude spanwise flow, from the root towards the tip of the plate, occurs up to the location of the center of the system of vortical structures. Outboard of this location, the spanwise flow is in the opposite (negative) direction, that is, from the tip towards the root. It is associated with the flow induced by the tip vortex, in accord with the streamline pattern in that region. Thus, formation of the large-scale vortical structures, evident at $x/C = 0.5$ for the straight leading-edge, is in accord with the opposing directions of spanwise flow along the plate. In contrast, for the plate with the sinusoidal leading-edge, such pronounced regions of spanwise flow do not exist, as evident in the image at the bottom right of Figure D1. Only very low levels of small-scale concentrations of positive transverse velocity v occur.

A further, remarkable feature is the fact that the structure of the tip vortex is relatively uninfluenced by the form of the leading-edge of the plate, i.e., straight versus sinusoidal. That is, the patterns of streamwise vorticity ω_x and transverse velocity v are remarkably similar for these two extreme cases of leading-edge geometry, despite the fact that the inboard vortex system is drastically altered.

The present investigation characterizes the flow structure for a relatively low Reynolds number. For wings undergoing flapping motion at relatively high reduced frequency, it is expected that the fundamental mechanisms of three-dimensional vorticity generation and development will persist to higher Reynolds number, especially for the sharp, thin leading-edge employed herein. It would be informative, however, to consider wings having an airfoil cross-section over a wide range of Reynolds number in future investigations.

In summary, effective passive control of the flow structure at inboard locations on a flapping wing can be attained with a leading-edge having a sinusoidal shape. It is anticipated that this concept can be extended to a wider range of wing motions, including revolving or rotating wings, where spanwise flow is expected to be prevalent.

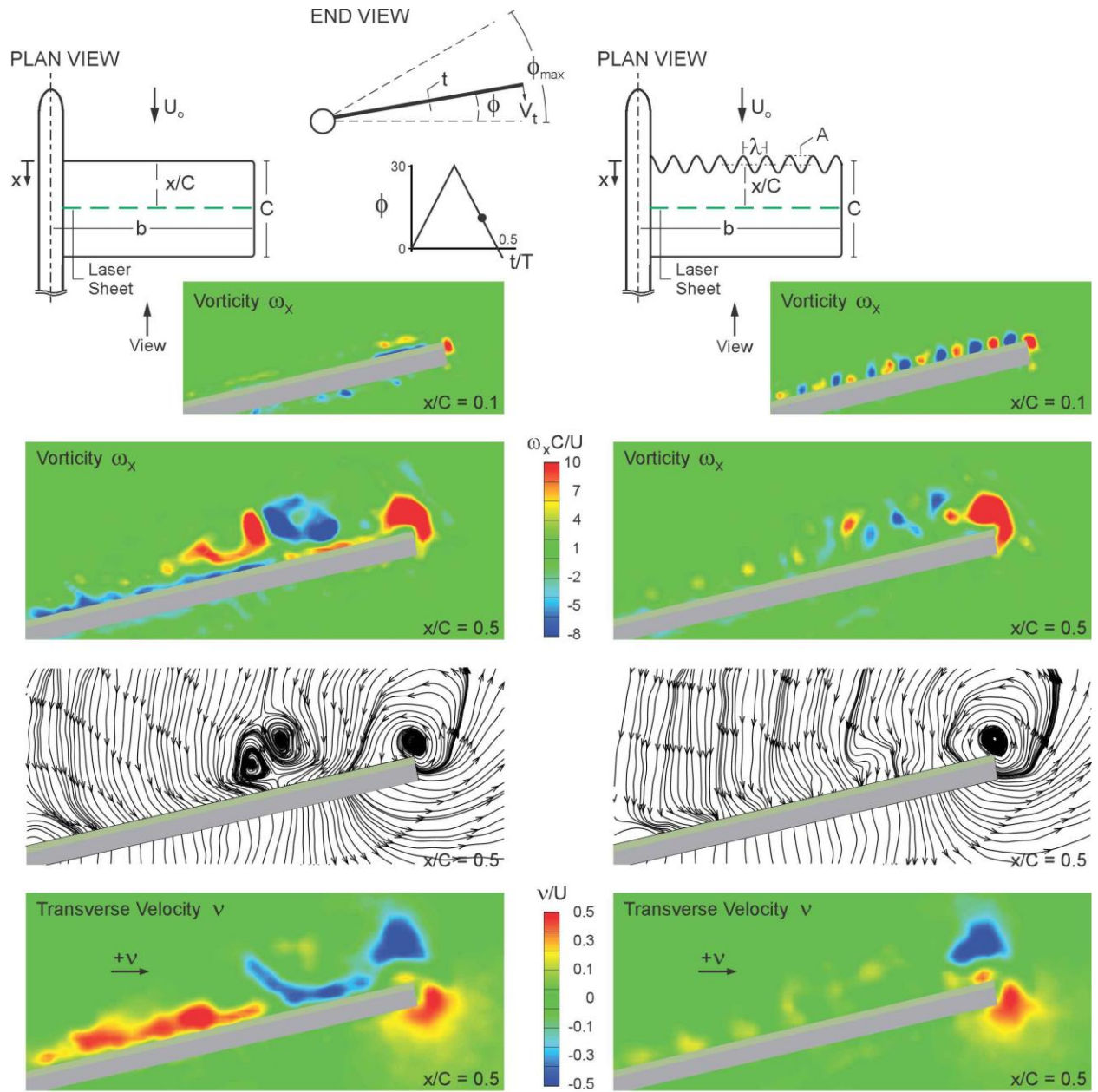


Figure D1: Comparison of flow structure on a flapping plate without and with a sinusoidal leading-edge. Flapping angle $\phi = 13.3^\circ$; angle of attack $\alpha = 8^\circ$; Reynolds number $Re = 1,300$; dimensionless frequency $k = \pi f C / U = 0.3$.

APPENDIX E

VORTICAL STRUCTURES ON A FLAPPING WING

ABSTRACT

A wing in the form of a rectangular flat plate is subjected to periodic flapping motion. Space-time imaging provides quantitative representations of the flow structure along the wing. Regions of spanwise flow exist along the wing surface, and depending on the location along the span, the flow is either towards, or away from, the tip of the wing. Onset and development of large-scale, streamwise-oriented vortical structures occur at locations inboard of the tip of the wing, and they can attain values of circulation of the order of one-half the circulation of the tip vortex. Time-shifted images indicate that these streamwise vortical structures persist over a major share of the wing chord. Space-time volume constructions define the form and duration of these structures, relative to the tip vortex.

1. EXPERIMENTAL SYSTEM AND TECHNIQUES

A free-surface water channel was employed for the present experiments. It had an overall test section length of 4877 mm, a width of 927 mm, and a depth of 610 mm. Conditioning of the upstream flow was accomplished by use of a honeycomb-screen arrangement involving a sequence of five screens, in order to maintain the turbulence intensity at a relatively low value of 0.3%. The value of free-stream velocity U was 25.4 mm/s.

Figure E1 provides a schematic of flapping wing system. The wing had the form of a flat plate, which was attached to a body of revolution undergoing controlled rotational motion. The setup was placed in the water channel such that when the wing is at horizontal location, it is at mid-height of the water level. The height of the water level was 610 mm and the wing rotated through a total angle of 60° which yielded a peak to peak displacement of the wing tip of 100 mm. Therefore the effects from the bottom wall and the upper free surface were minimal. A series of preliminary experiments involving acquisition of PIV images at different values of magnification factor were undertaken to confirm this point. The entire wing system was positioned successively closer to the side wall of the channel. The quantitative images of the vortex structure at different locations of the wing system remained the same.

The plate had a span $b = 101.6$ mm, a chord $C = 50.8$ mm, and a thickness $t = 1.59$ mm. All edges of the plate were sharp. As indicated in the plan view, the outboard corners were rounded with a radius of curvature $R = 2$ mm. The Reynolds number based on wing tip velocity was calculated using $Re = C2\Phi bf/v$ and its value is 565.

The body of revolution indicated in Figure E1 was driven by a motor control system located above the free surface of the water. Arbitrary functional forms of the flapping could be generated by programming the motor system. The periodic motion of the wing involved two basic forms: triangular motion (a succession of positive and negative ramps) and sinusoidal motion, as indicated in the schematics of Figure E1. The main body of results described herein corresponds to the triangular motion; comparisons with sinusoidal motion indicate that the basic features of vortex formation are generic to both types of motion. For the triangular motion, zero acceleration of the wing occurs, except at the corners. In this region, the effective smoothing had a duration of $\Delta t/T = 0.015$, where T is the period of the motion. The wing rotated between the

extreme values $\phi_m = 30^\circ$ and -30° . Due to the symmetry, only the positive half of the cycle is presented here. For all experiments, the geometric angle-of-attack relative to the body was maintained at $\alpha = 0^\circ$. Due to the flapping motion, an effective angle-of-attack exists. It is defined as $\alpha_e = \tan^{-1} V_t / U$ in which V_t is the local tangential velocity of the wing at a given value of spanwise distance y/b from the axis of rotation. The effective angle of attack for triangular motion is constant and has value at the tip of the wing ($y/b = 1$) of $\alpha_e = 22.7^\circ$ during the downstroke and -22.7° during the upstroke of the wing. The dimensionless frequency of the flapping motion was $k = \pi f C / U = 0.3$, and the advance ratio was $J = 2.4$. The basic elements of the unsteady flow structure described herein were also observed at additional values of k , J and angle-of-attack α .

Dye visualization was employed to determine the overall, qualitative features of the instantaneous flow structure along the wing. This was accomplished by employing a total of nine dye injection holes, equally spaced along the span. The centers of the holes were located at a distance of 1.5 mm downstream of the leading-edge of the plate.

The quantitative structure of the flow was determined using a technique of particle image velocimetry. Data acquisition and processing were performed by using TSI Insight 3G software. The location of the laser sheet and the direction of view of the camera system are indicated in the schematics of Figure E1. The results given herein correspond to crossflow planes at streamwise locations from $x/C = 0.1$ to 1.1 , at increments of $\Delta x/C = 0.1$. In order to optimize the quality of the imaging, it was necessary to filter the water with a one micron filter, then seed it with 12 micron diameter metallic-coated hollow plastic spheres. The seeding density was sufficiently high such that a minimum of 15 particle images were maintained within the interrogation window of $32 \text{ pixels} \times 32 \text{ pixels}$. A pulsed Yag laser system having a maximum output of 50 mJ was employed in conjunction with spherical and cylindrical lenses, in order to generate a laser sheet of 1 mm thickness. For all experiments, the maximum power level was 40 mJ. A laser pulse rate of 14.29 Hz was employed, allowing acquisition of 14.29 image pairs per second. An imaging camera having an array $1,600 \text{ pixels} \times 1,200 \text{ pixels}$ was employed for image acquisition. The effective magnification was 14.6 pixels/mm. Evaluation of the patterns of particle images involved a frame-to-frame cross-correlation technique with 50% overlap of interrogation areas of $32 \times 32 \text{ pixels}$. Approximately 7227 velocity vectors were determined within the field of view, with an effective grid size of 1.09 mm.

Both instantaneous and phase-averaged patterns of the flow structure are addressed herein. Preliminary experiments showed that the flow structure on the wing and in the near wake converged after the first cycle of oscillation. Therefore, image acquisition was not triggered until the wing completed two cycles of oscillation, so the initial transient does not affect either instantaneous or averaged images. For phase-averaging, a total of 12 instantaneous images were employed. In view of the controlled forcing of the flapping wing, however, the instantaneous flow structure was found to be highly repetitive from cycle to cycle, and the phase-averaged patterns showed essentially the same features as the instantaneous images. A quantitative comparison is provided herein.

2. MARKER VISUALIZATION OF FLOW STRUCTURE

Figure E2 shows dye visualization from ports located along the leading-edge of the wing. For the angle $\phi = 10.8^\circ$ represented in this image, the effective angle-of-attack is $\alpha_e = \tan^{-1} V_t / U = 22.7^\circ$ at the tip of the wing, in which $V_t = 10.64 \text{ mm/s}$ is the tangential tip velocity of the

flapping wing and U is the freestream velocity. At this value of $\alpha_e = 22.7^\circ$, a separated shear layer forms at the leading-edge of the plate.

The following details are evident from the dye visualization image. Well-defined spanwise flow is indicated by the dye marker along the surface of the plate. The corresponding fronts of the surface dye marker corresponding to this spanwise flow are designated as Q_1 , Q_2 , and Q_3 . The dye marker emanating directly from the dye visualization ports marks the separated shear layer from the leading-edge of the plate. Along this layer, small-scale concentrations of dye are evident; they correspond to Kelvin-Helmholtz vortices, designated as KH. The succession of KH vortices has a trajectory that is deflected in the outboard direction, that is, towards the tip of the wing.

An important consequence of the spanwise flow is reorientation of the vortices formed from the leading-edge of the plate, whose vorticity is nominally oriented in the spanwise direction. Tracking the small scale Kelvin-Helmholtz vortices visualized by dye provides an indication of the effects of spanwise flow and the consequent reorientation of the large scale vortical structures on the upper surface of the wing. That is, the small-scale Kelvin-Helmholtz (K-H) vortices are located about the periphery of the large-scale structures, so tracking the K-H vortices provides a direct indication of the increasing inclination, and thereby the vorticity reorientation, of the large-scale structures. For example, the small-scale KH structures designated as S_2 and T_2 are reoriented in the direction indicated by the arrow, relative to their successor W_2 . Furthermore, this process is preceded by the reoriented small-scale structures S_1 , T_1 , which are reoriented relative to their successor W_1 . This reorientation process culminates in formation of a large-scale cluster of dye A_2 and its predecessor, A_1 , which is located near the trailing-edge of the wing. Simultaneously, with the foregoing process of reorientation, the three-dimensional process of vortex shedding from the leading-corner of the wing is associated with the large-scale dye cluster B_2 and its predecessor B_1 . The foregoing features of dye visualization are intended to serve as a guide for interpretation of quantitative imaging of the flow structure in successive crossflow planes, as addressed in the following.

3. IMAGING OF FLOW STRUCTURE

Figure E3 shows images of the flow structure at two crossflow planes, located at $x/C = 0.4$ and 0.8 , with the dye visualization pattern of Figure E2 as a reference. The image at $x/C = 0.4$ shows contours of constant transverse velocity v/U . In accord with the dye marker in the vicinity of the surface of the plate, in particular, the dye fronts Q_1 , Q_2 , and Q_3 indicated in Figure E2, large values of positive $v/U = 0.5$, oriented towards the tip of the plate, occur along its boundary. This pronounced spanwise flow is evident up to approximately $y/b = 0.6$. At larger values of y/b , the concentration of v/U is deflected from the surface of the plate. In the vicinity of the tip of the plate, concentrations of positive (red) and negative (blue) magnitudes of v/U are evident, due to formation of the tip vortex.

The dye visualization image of Figure E3 shows that the large-scale, coherent clusters of dye become particularly prevalent at larger streamwise distances x/C . The representative image of vorticity in the crossflow plane, at $x/C = 0.8$, indicates the tip vortex and, in addition, coherent concentrations of positive (red) and negative (blue) vorticity, which have arisen from the aforementioned mechanisms described in conjunction with Figure E2. In the image layouts that follow, the spatial development of the representative patterns of transverse velocity v/U and vorticity $\omega_x C/U$ will be addressed.

Figure E4 shows the streamwise evolution of contours of constant transverse velocity v/U from $x/C = 0.4$ to 0.8 . In the direction of view designated by the schematic, positive transverse velocity v is from right to left, in accord with spanwise flow towards the tip of the wing. At values of y/b up to at least 0.75 , pronounced regions of positive (red) transverse velocity are evident at all values of x/C . At values of y/b in the region $0.75 < y/b < 0.9$, concentrations of positive (red) and negative (blue) v/U occur away from the surface of the plate, due to the onset and development of coherent structures of streamwise-oriented vorticity, to be addressed subsequently. Moreover, in the vicinity of the tip of the plate, the positive and negative concentrations of v/U are associated with the tip vortex. Well-defined regions of negative v/U extend a significant distance inboard of the tip of the plate, due to reattachment and extension of the streamline pattern in that region, associated with the tip vortex. This pattern is evident in the representative image of streamlines at $x/C = 0.5$ shown in the inset of Figure E4. In the visualization of Figure E2 this region is free of dye marker, due to the fact that tip vortex is not seeded with dye in this region near the tip of the plate. That is, dye was not injected into the tip vortex, and therefore its region of influence appears as an unmarked region of the plate surface in Figures E2 and E3.

Corresponding patterns of streamwise vorticity are shown in Figure E5. At $x/C = 0.4$, concentrations of ω_x are designated as a through d . The elongated region a is consistent with reorientation of vorticity in the separated shear layer, as addressed in conjunction with Figure E2. Concentration c , located immediately beneath a , is in accord with eruption of the boundary layer from the surface of the plate, driven by the spanwise velocity v along the surface of the plate, designated in Figure E4. Concentrations b and d are the counterparts of concentrations a and c . At successively larger values of x/C , these defined regions of vorticity undergo an interaction at $x/C = 0.5$, and eventually concentrations e and f become well defined at $x/C = 0.6, 0.7$, and 0.8 . Concentrations e and f are consistent with those given at $x/C = 0.8$ in Figure E3, and with the dye marker visualization, in the form of coherent clusters of dye A_I and B_I , indicated in Figures E2 and E3.

The foregoing representations of dye visualization and transverse velocity v/U and streamwise vorticity $\omega_x C/U$ are shown at a given instant, i.e., a given angle ϕ of the wing. The issue arises as to whether the well-defined concentrations of vorticity shown in Figure E5 at $x/C = 0.6, 0.7$ and 0.8 occur at other values of x/C when the flow structure is tracked at different values of angular deflection ϕ . Figure E6 shows contours of constant streamwise vorticity $\omega_x C/U$, which are shifted in time relative to each other. The value of the time shift Δt , relative to the period T of the wing oscillation, is $\Delta t/T = 0.0175$. This value, which was selected from a range of time shifts, shows the optimum degree of replication of the vortex structure over the streamwise extent of the flow. Using the freestream velocity U and the chord C of the wing, this time shift may also be represented as $\Delta t U/C = 0.175$. Furthermore, the incremental value of angular deflection of the wing corresponding to this phase shift is $\Delta\phi = 2.1^\circ$. Values of ϕ in relation to x/C are given in the table in the inset of Figure E6. Viewing the images of Figure E6, a generally similar structure of the positive (red) and negative (blue) concentrations of streamwise vorticity ω_x is present over the range $0.7 \leq x/C \leq 1.1$. At smaller values of x/C , these positive and negative contributions are generally evident, but their form and circulation differ from those at larger values of x/C , including partitioning of the negative (blue) region of ω_x into two smaller-scale concentrations at $x/C = 0.5$ and 0.6 .

Figures E7a and E7b show the time history of contours of constant streamwise vorticity $\omega_x C/U$ at the mid-chord of the plate, $x/C = 0.5$. Only positive (red) contours are shown in Figure

E7a and only negative (blue) in 7b. The images at the upper left of these figures show both positive and negative regions of $\omega_x C/U$ at two selected angles $\phi = 20^\circ$ and 13.75° , and in each figure, the lines provide a link between the designated regions of vorticity in the isometric view of the entire space-time image of $\omega_x C/U$ and the individual concentrations of positive and negative vorticity. Moreover, in Figures E7a and E7b, a rectangular region designated by a dashed line focuses on the space-time development of the patterns of vorticity at smaller values of ϕ , i.e., $25^\circ \geq \phi \geq 0^\circ$ during the downstroke motion of the plate. Zoomed-in views of the patterns of positive (red) and negative (blue) vorticity within this rectangular region are provided in Figure E7c. For the positive (red) volume of vorticity, the development and persistence of the tip vortex is clearly evident. Furthermore, the onset and degeneration of the inboard positive (red) concentration of vorticity is also indicated. Smaller scale volumes of positive vorticity extend between the tip vortex and the distributed vorticity adjacent to the surface of the plate at small values of angle ϕ . Regarding the patterns of negative (blue) vorticity shown in the bottom space-time image of Figure E7c, the tip vortex of negative sign exists over the range of angles $30^\circ \geq \phi \geq 25^\circ$ together with the tip vortex of positive sign; from then on, the tip vortex has only a positive sign. The negative concentration of the inboard vortex system is particularly evident for the range of angles $15^\circ \geq \phi \geq 5^\circ$. Viewing together the space-time images of Figure E7c, it is evident that the lifetime of the positive and negative concentrations of vorticity extends over an increment of deflection angle ϕ corresponding approximately to $\Delta\phi = 10^\circ$, whereas the tip vortex is present over a range $\Delta\phi = 30^\circ$.

Figure E8 shows comparison of the structure of the inboard vortex system and the tip vortex for both triangular motion and sinusoidal motion. This comparison is made at a streamwise distance $x/C = 0.5$. The selected images show various phases of development of the vortex system, including the initial onset of single, well defined positive (red) and negative (blue) concentrations of vorticity and, at a later stage, the complex, but highly ordered interaction of smaller-scale concentrations of vorticity. In essence, a very similar structure of the inboard vortices occurs for both types of motion, but their occurrence is shifted to lower values of the deflection angle ϕ for the sinusoidal motion relative to the triangular motion. This observation indicates that the mechanisms giving rise to the inboard vortices are robust for different classes of functional forcing of the flapping plate.

Figure E9 shows representative instantaneous images of streamwise $\omega_x C/U$, in comparison with averages of different numbers of instantaneous images, i.e., 3, 6, 9, and 12 images. All of these images are remarkably similar, and there is nearly undetectable degradation of peak vorticity levels with an increasing number of images employed for the phase-average. For a representative concentration of vorticity, located furthest inboard in the images of Figure E9, the peak vorticity was plotted as a function of the number of images employed for the phase-average. The values of the instantaneous image and the phase-average involving two images were respectively within 2.8% and 0.97% of the asymptotic value corresponding to an average of 6, 9, and 12 images.

4. CONCLUSIONS

A wing in the form of a rectangular flat plate undergoing a periodic flapping motion generates pronounced spanwise flow and coherent, streamwise-oriented vortical structures at inboard locations. The origin and development of these vortical structures have been characterized using qualitative dye visualization and quantitative imaging, which involves space-

time image acquisition and post-processing, in order to construct sectional and volume representations of the flow structure.

Spanwise flow along the surface of the plate towards its tip is a central feature. On the other hand, at locations just inboard of the tip of the plate, where the influence of the tip vortex is prevalent, the spanwise flow is oriented away from the tip, towards the root of the flapping plate. For both of these classes of spanwise flow, contours of constant transverse velocity indicate values as high as one-half the freestream velocity.

Away from the surface of the plate, along the separated shear layer formed from its leading-edge, reorientation of nominally spanwise vorticity occurs. This reorientation process is compatible with the spanwise flow towards the tip of the wing indicated in the foregoing, and it culminates in a large-scale concentration of positive streamwise vorticity. A corresponding large-scale concentration of negative streamwise vorticity occurs; it is linked to the process of three-dimensional vortex formation from the leading-corner of the flapping plate. These positive and negative inboard vortical structures have values of circulation of the order of one half the circulation of the tip vortex.

Images of streamwise vorticity, showing both spatial and temporal development, are provided over chordwise distances extending from the region near the leading-edge of the plate to the near-wake region. They show that the aforementioned features of the positive and negative large-scale vortical structures at inboard locations are persistent over this entire streamwise extent, though the detailed features of the patterns vary. Moreover, space-time volume images of the patterns of streamwise vorticity indicate that the large-scale inboard structures have a lifetime that extends over a range of flapping angle of approximately 10° , in comparison with the lifetime of the tip vortex which extends over approximately 30° . These large-scale inboard vortical structures can degenerate into smaller-scale, interacting structures during portions of the flapping cycle of the wing. Nevertheless, the degenerated patterns of smaller-scale streamwise-oriented vortices are remarkably coherent and repetitive.

Patterns of both the large-scale and small-scale structures are remarkably similar for distinctly different types of flapping motion, that is, triangular and sinusoidal variations of flapping angle with time. Certain details of the flow patterns are, however, phase-shifted when comparing the oscillation cycles of these two types of flapping motion.

The present study is distinct from previous investigations, in that it employs a thin rectangular flat plate at zero angle of attack undergoing motion in a vertical stroke plane, at a high value of advance ratio corresponding to forward flight. Comparisons with previous investigations of insect flight are difficult, due to the different wing configurations, types of motion, and parameters employed in those studies. In future investigations, it would be insightful to address basic planforms representative of insect wings, in addition to the rectangular planform addressed herein. Such efforts would define the degree of persistence of the vortical structures identified herein. Moreover, the present investigation characterizes the flow structure at a relatively low Reynolds number. It is anticipated, however, that the fundamental mechanisms of three-dimensional vorticity generation and development will persist to higher Reynolds number, especially for wing configurations having sharp, thin leading-edges. This aspect also deserves attention in future studies.

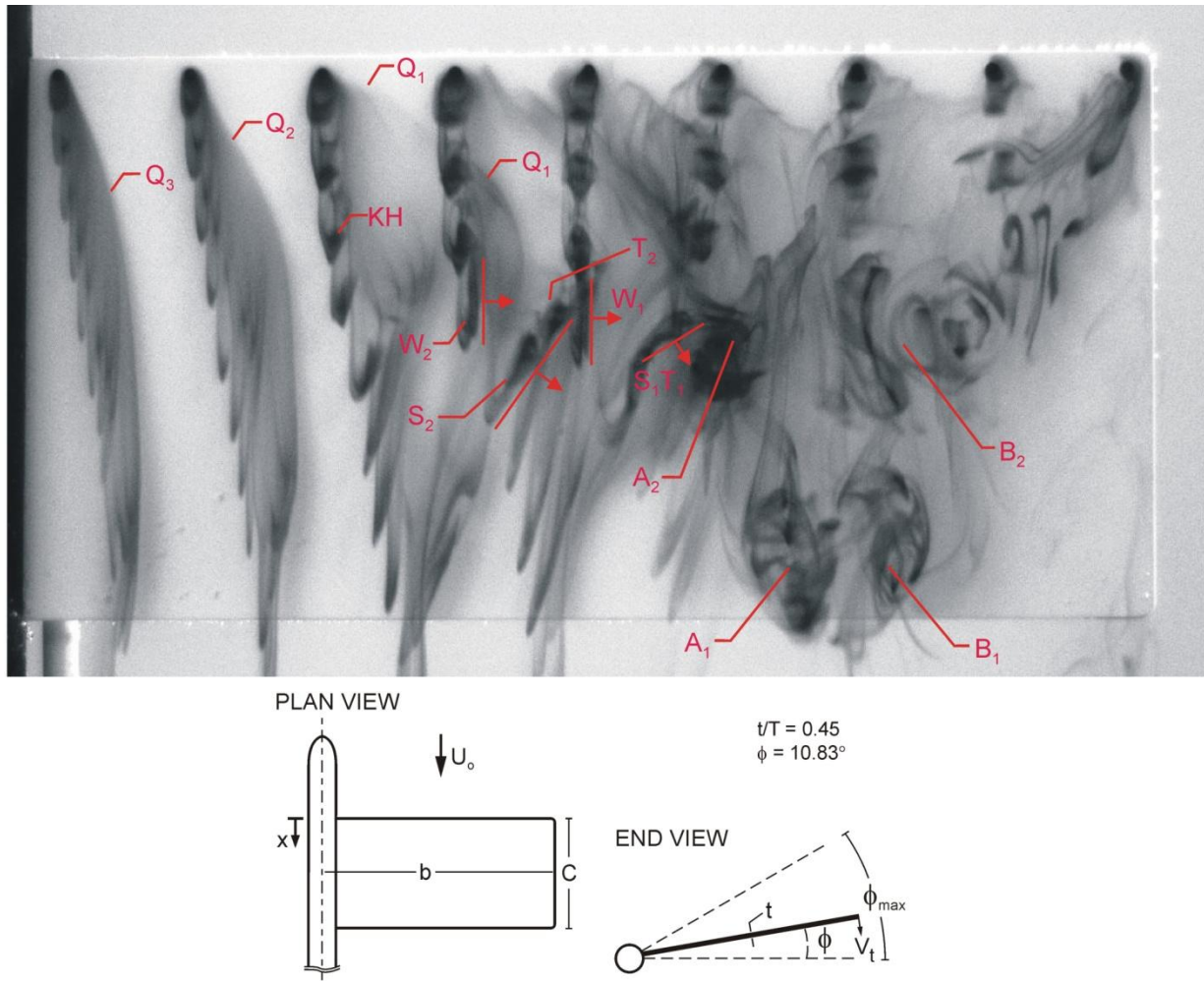


Figure E2: Plan view of flow structure on the flapping wing during its downstroke motion, visualized by dye marker.

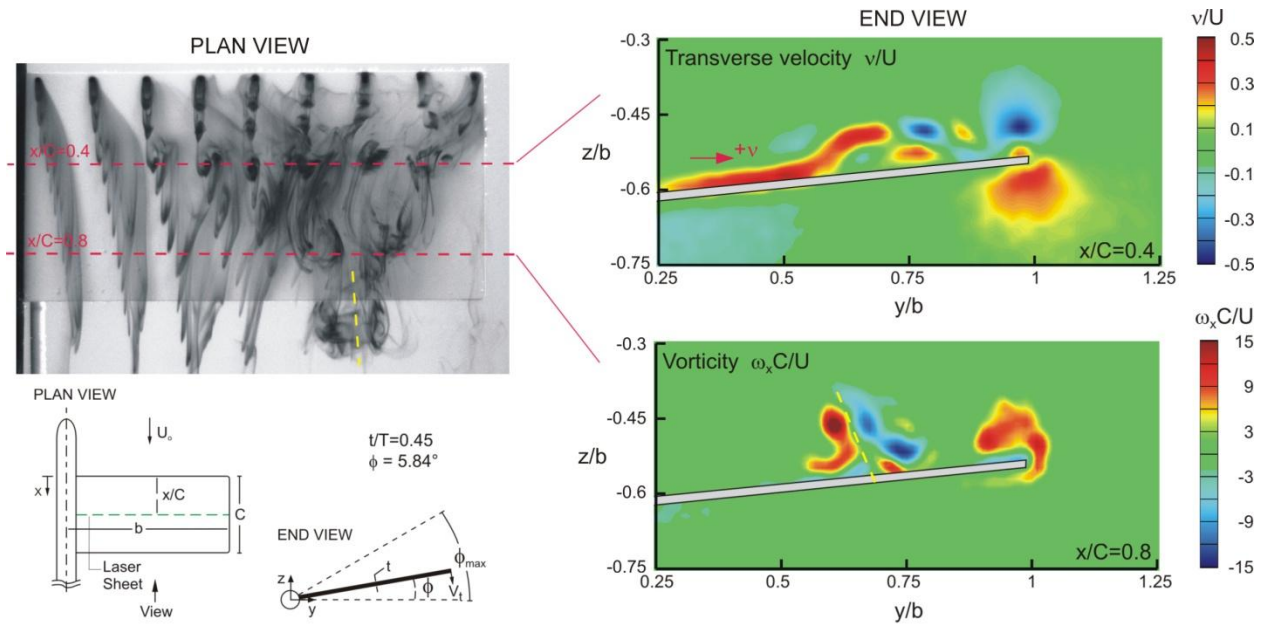


Figure E3: Flow structure on selected crossflow planes in relation to dye visualization.

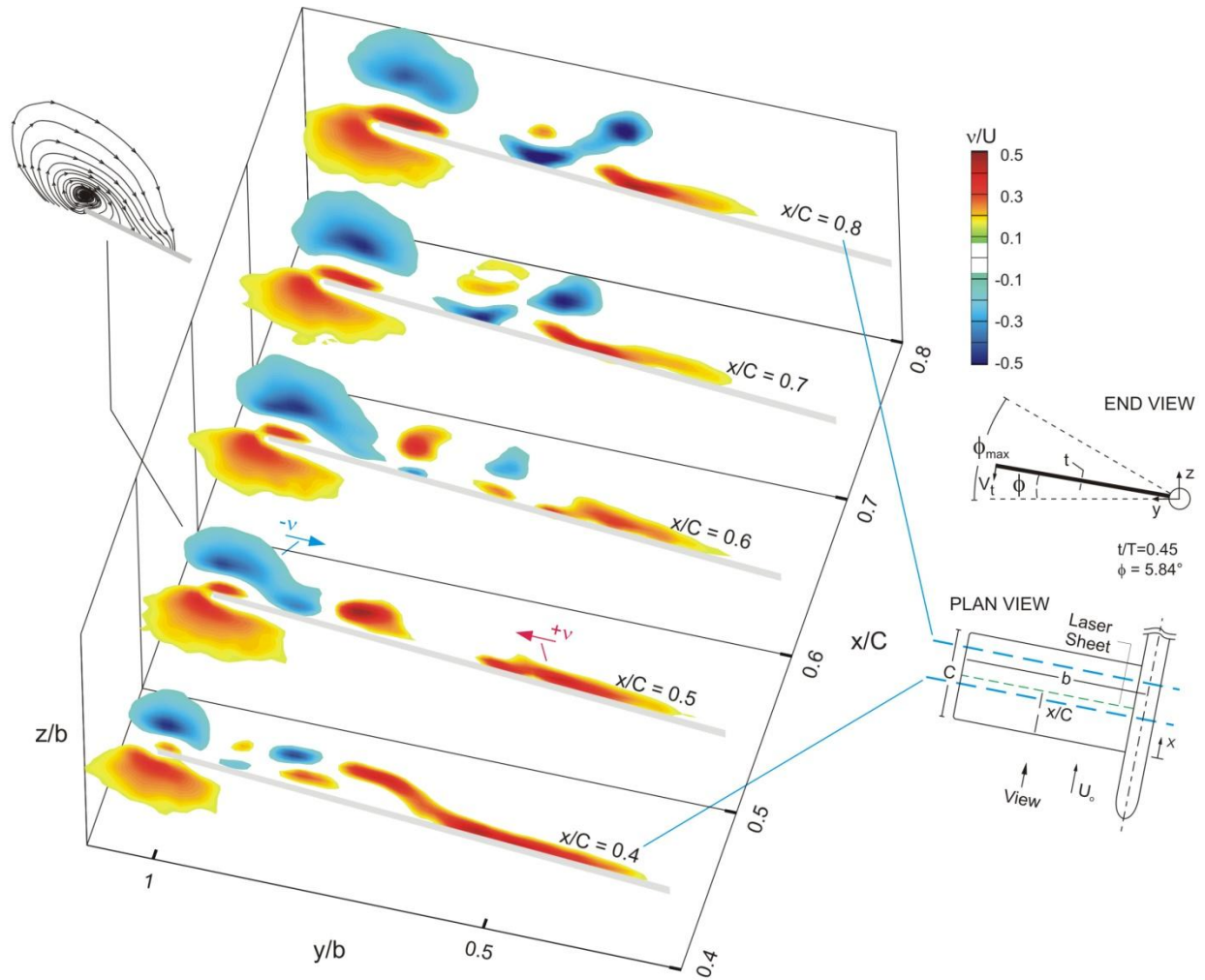


Figure E4: Contours of constant transverse velocity at successive streamwise locations along the surface of a flapping wing, at a given instant during the downstroke motion.

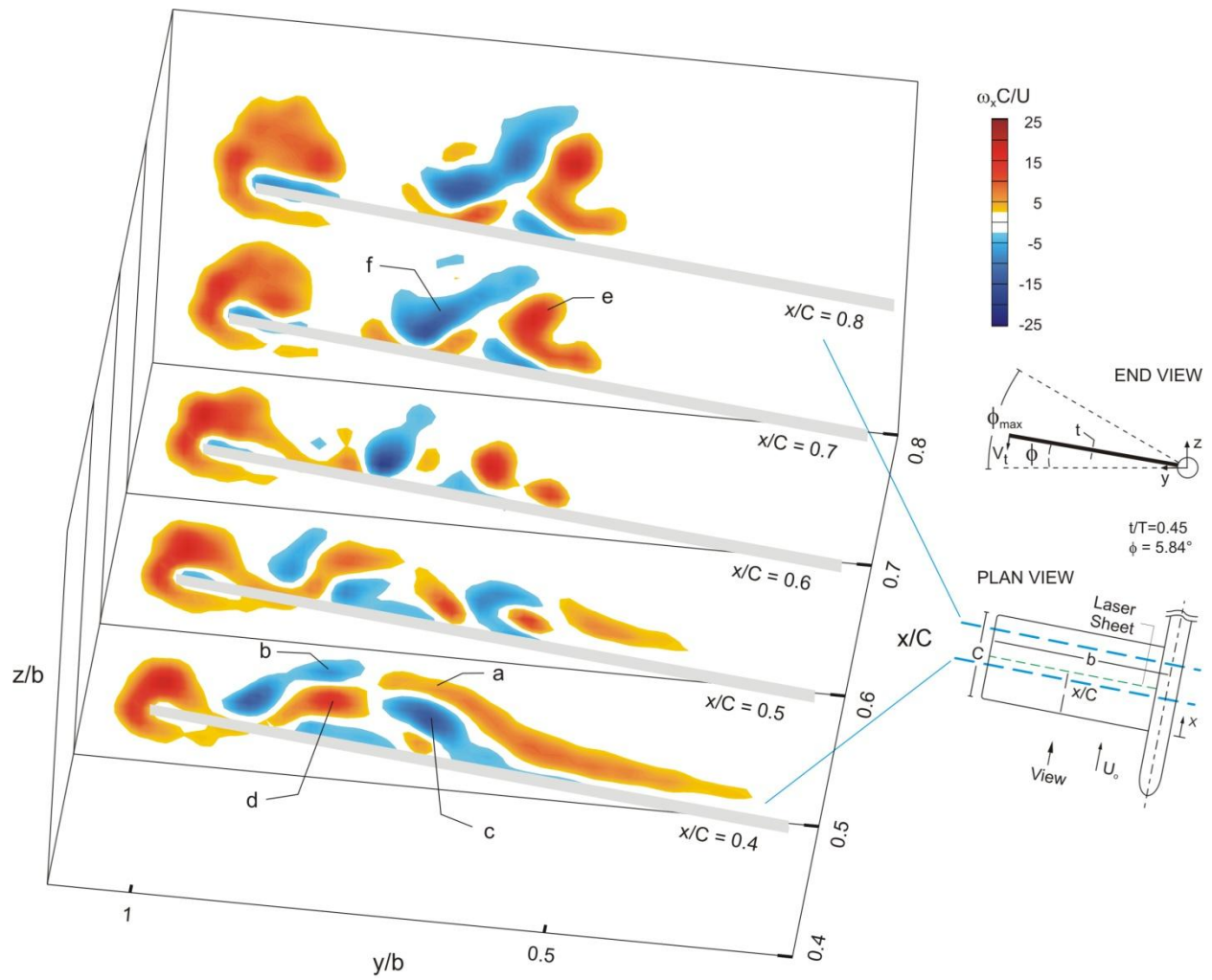


Figure E5: Contours of constant streamwise vorticity at successive streamwise locations along the surface of the wing, at a given instant during the downstroke motion.

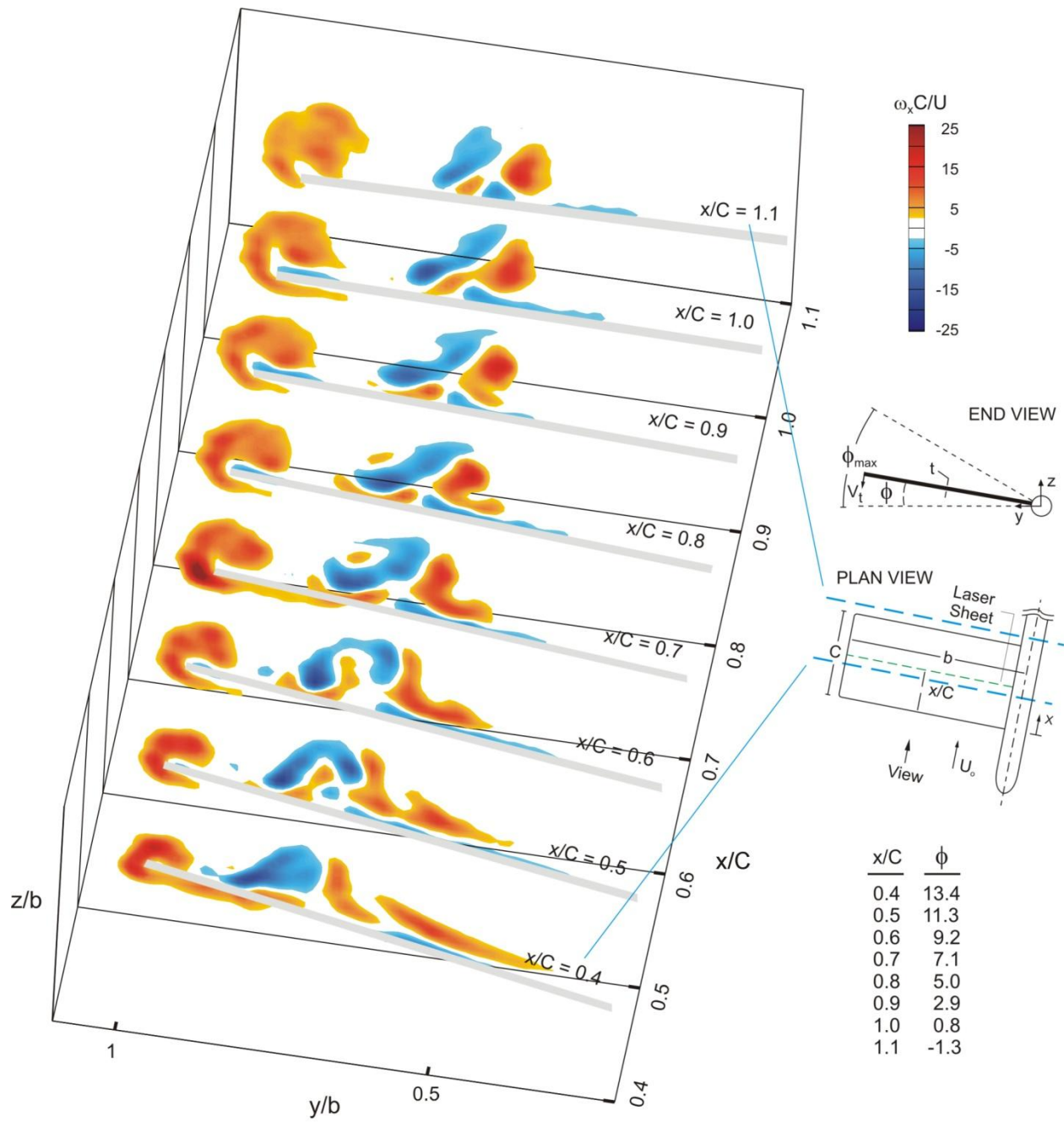


Figure E6: Time-shifted patterns of streamwise vorticity along the surface of the wing and into the near-wake, during the downstroke motion of the wing.

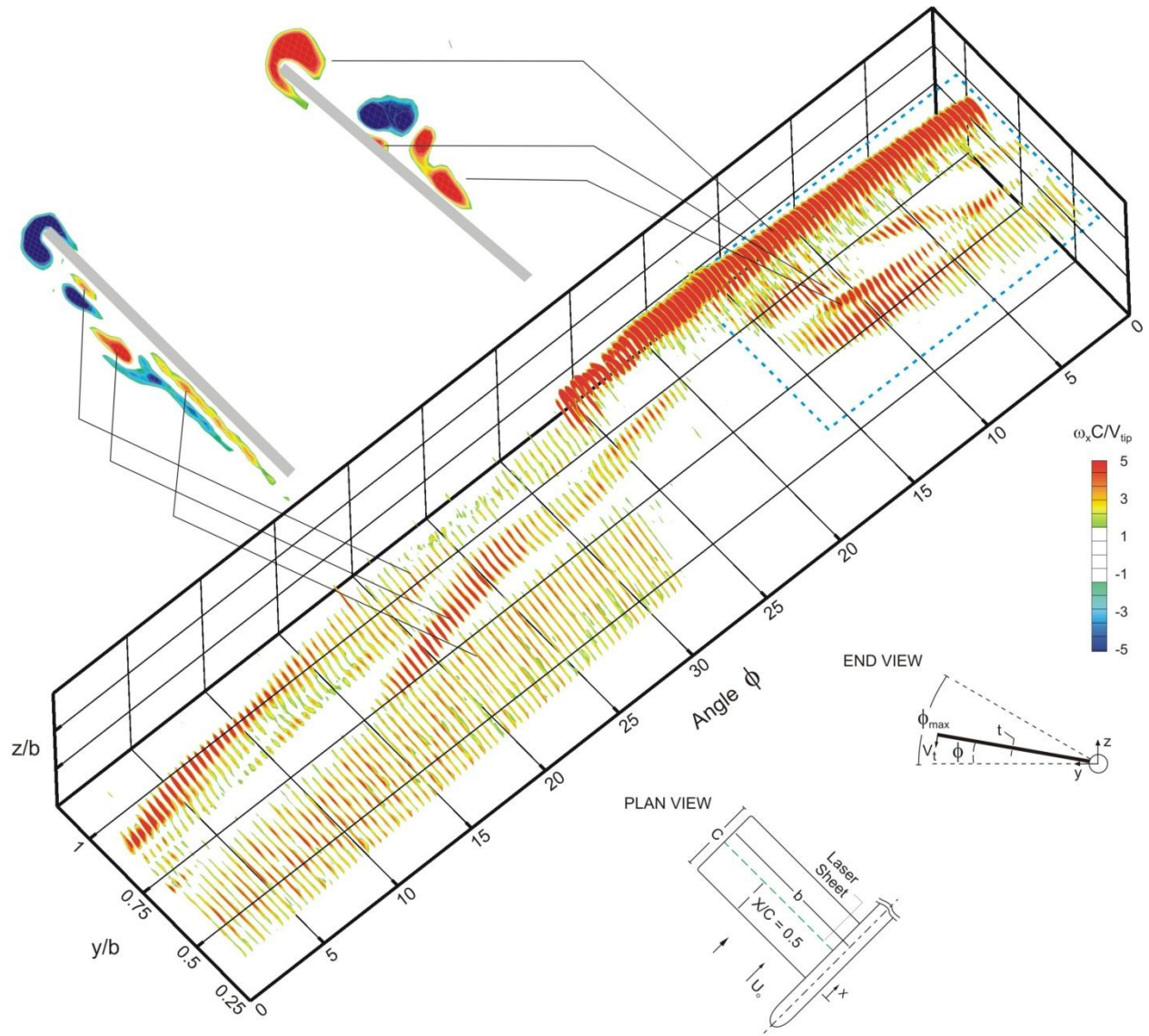


Figure E7a: Space-time volume constructed from contours of constant streamwise vorticity at the mid-chord of the wing during its downstroke and upstroke motion. The space-time volume represents only positive (red) streamwise vorticity.

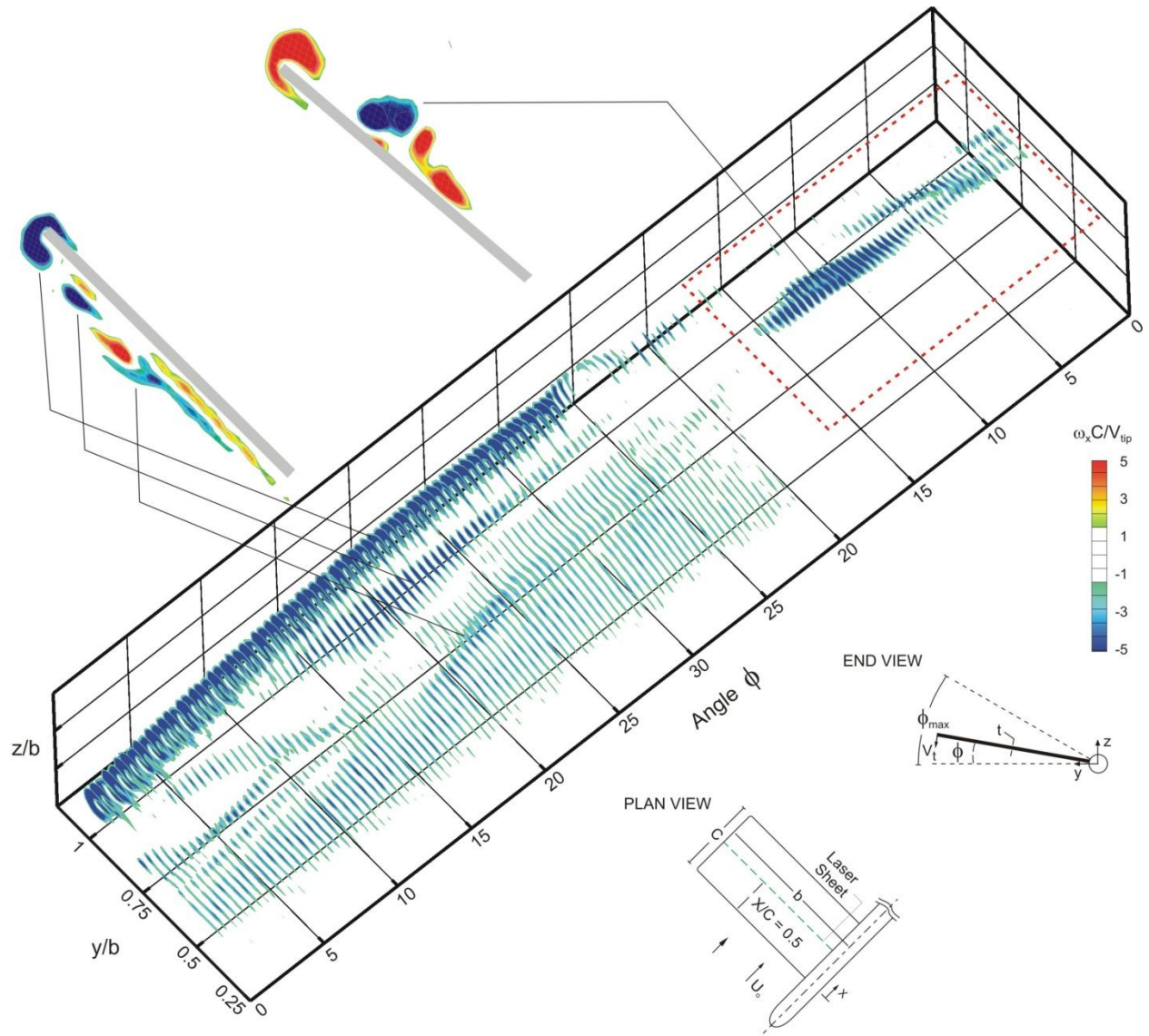


Figure E7b: Space-time volume constructed from contours of constant streamwise vorticity at the mid-chord of the wing during its downstroke and upstroke motion. The space-time volume represents only negative (blue) streamwise vorticity.

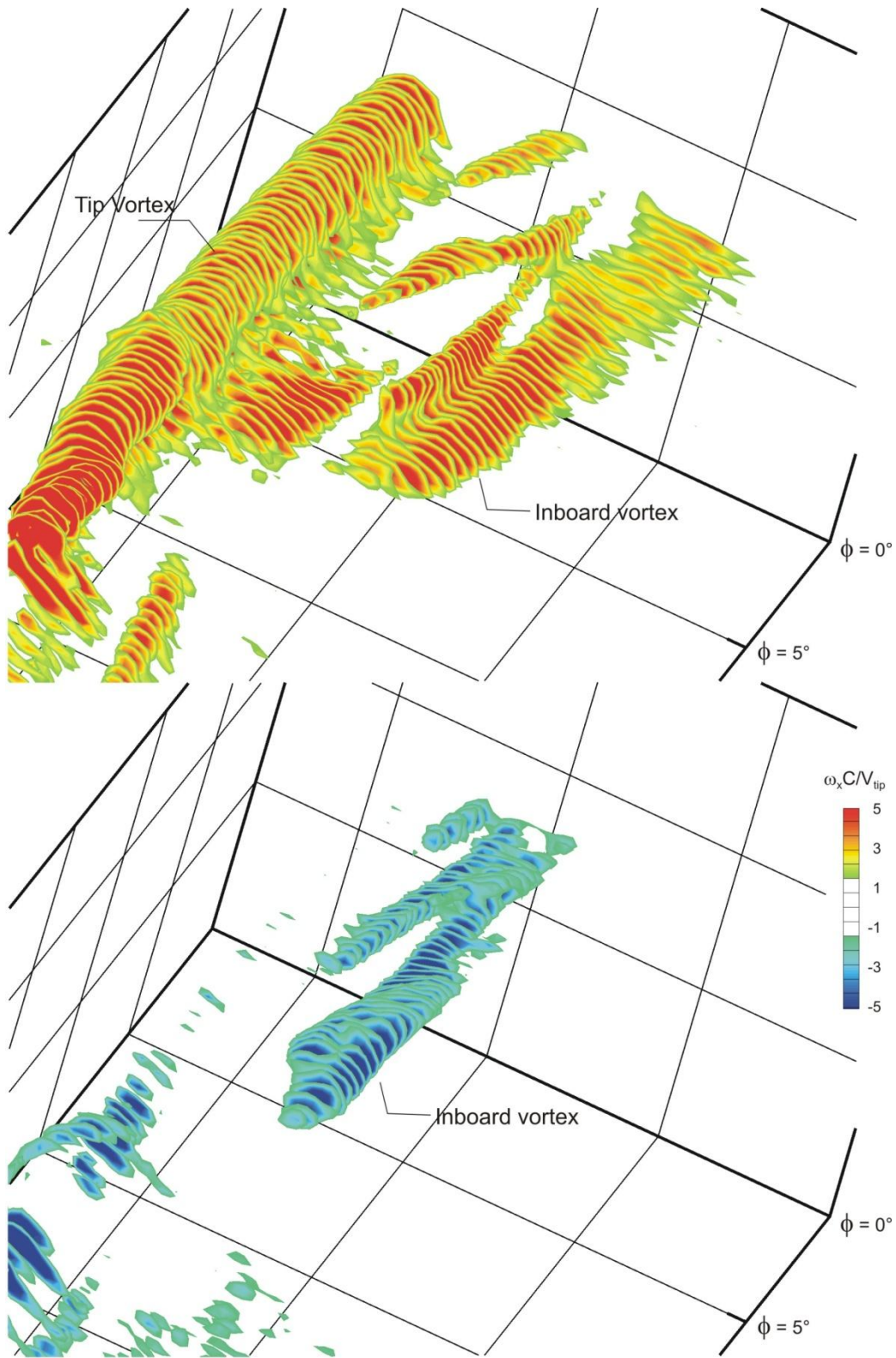


Figure E7c: Zoomed-in views of space-time volumes of positive (red) and negative (blue) vorticity corresponding to the domain within the dashed line rectangles indicated in Figures 7a and 7b.

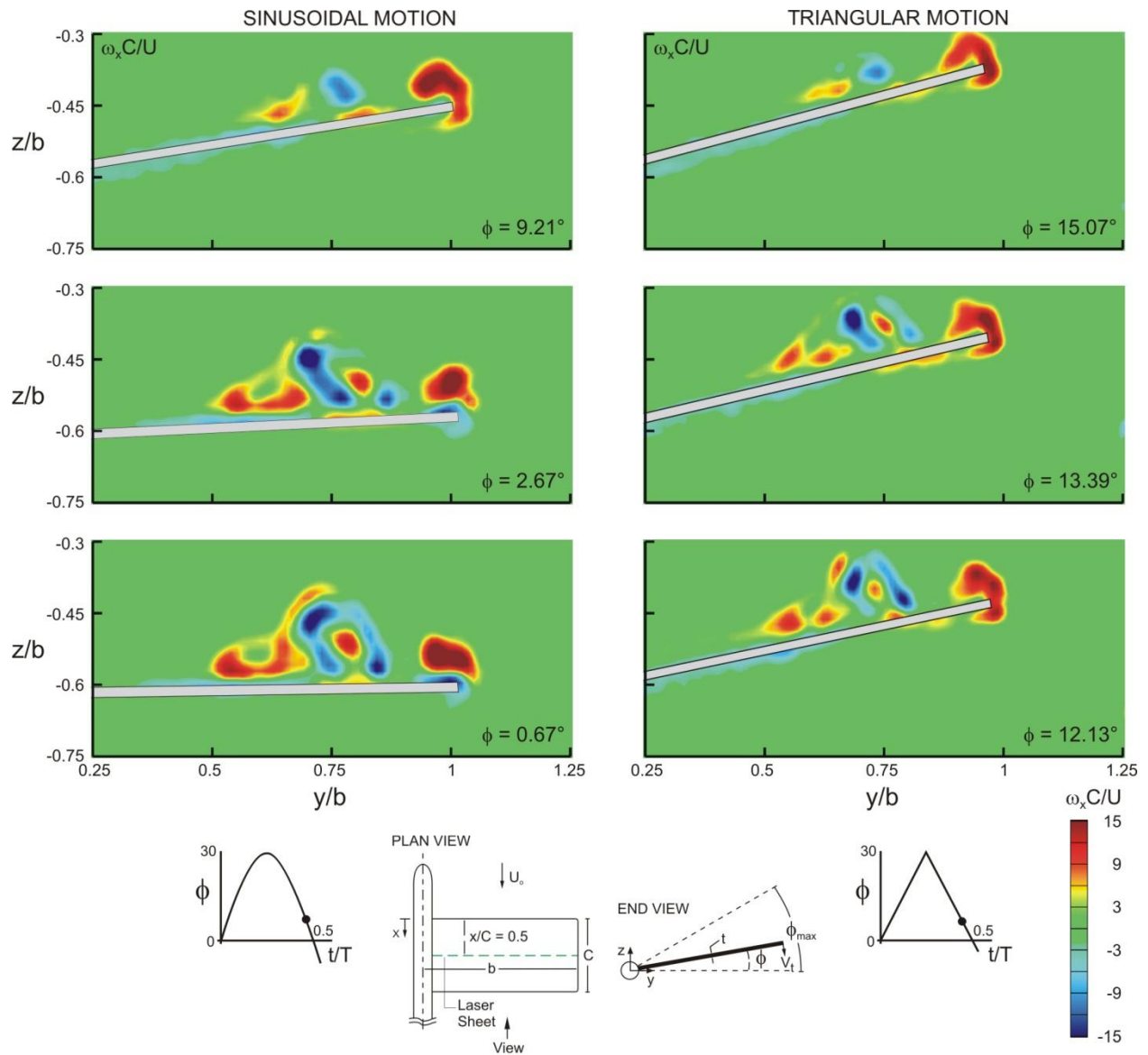


Figure E8: Comparison of representative patterns of streamwise vorticity for sinusoidal and triangular flapping motions of wing.

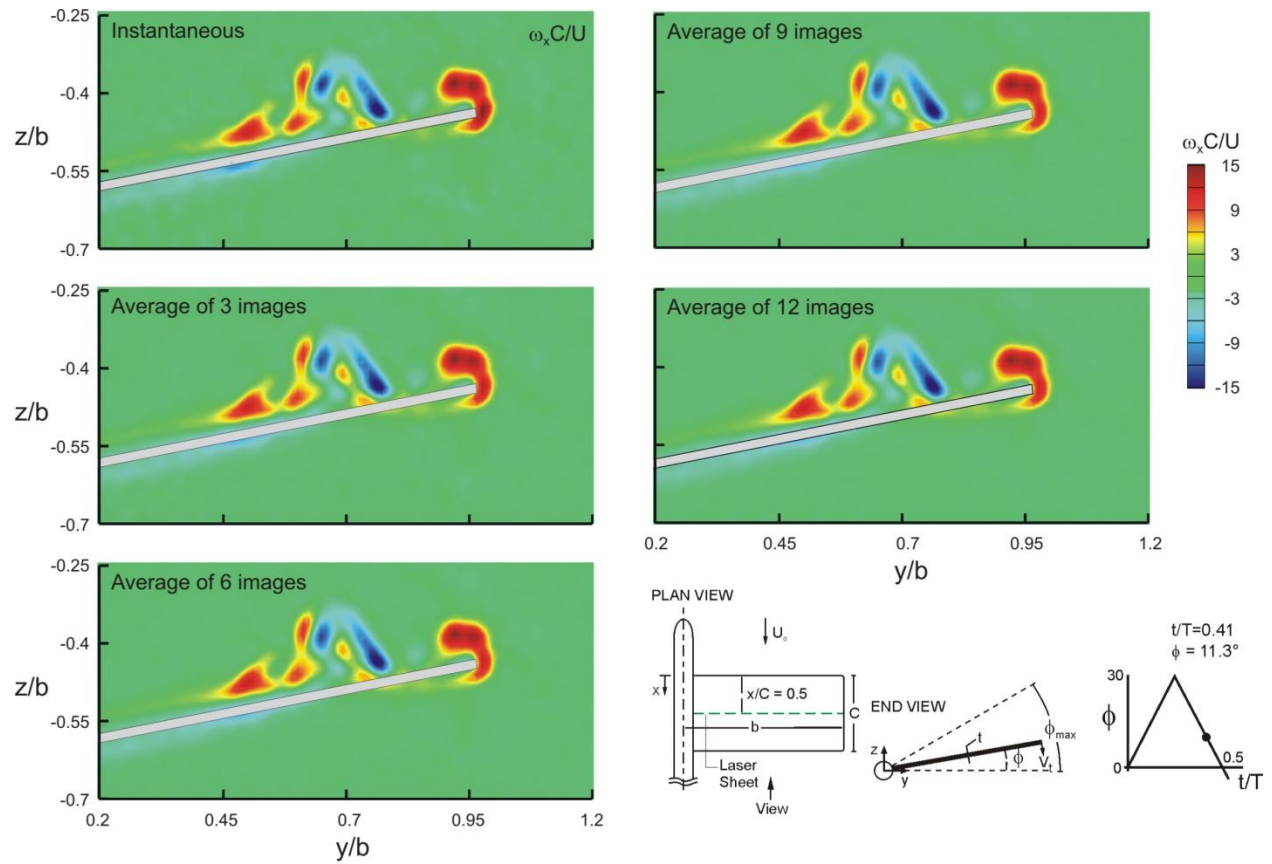


Figure E9: Comparison of instantaneous and phase-averaged images of representative pattern of streamwise vorticity.

APPENDIX F

FLOW PAST A DELTA WING WITH A SINUSOIDAL LEADING-EDGE: NEAR-SURFACE TOPOLOGY AND FLOW STRUCTURE

ABSTRACT

The near-surface flow structure and topology on a delta wing of low sweep angle, having sinusoidal leading edges of varying amplitude and wavelength, are investigated using a stereoscopic technique of high-image-density particle image velocimetry at a Reynolds number of 15,000. Identification of critical points, in conjunction with surface-normal vorticity and velocity, provide a basis for determining the effectiveness of a given leading edge. At high angle of attack, where large-scale three-dimensional separation occurs from the wing with a straight leading edge, an amplitude of the leading-edge protuberance as small as one-half of one percent of the chord of the wing can substantially alter the near-surface topology. When the amplitude reaches a value of four percent of the chord, it is possible to completely eradicate the negative focus of large-scale, three-dimensional separation, in favor of a positive focus of attachment. Moreover, alteration of the near-surface topology is most effective when the ratio of the wavelength to amplitude of the sinusoidal leading edge is maintained at a small value.

1. EXPERIMENTAL SYSTEM AND TECHNIQUES

Figure F1 shows the principal features of the experimental system. In Figure F1a, a simplified, conceptual schematic shows the coordinate system and definition of symbols related to location of the laser sheet relative to the surface of the wing. Figure F1b provides details of the experimental arrangement, and Figure F1c defines the parameters of the sinusoidal leading edge.

As shown in Figure F1a, the sweep angle of the delta wing had a value of $\Lambda = 50^\circ$, which corresponds to the nominal sweep angle of the wing with the sinusoidal leading edge. The root chord of the wing was $C = 200$ mm, and the wing thickness was 1.58 mm, with no beveling on either the leeward or windward side. The angle-of-attack of the wing was maintained at $\alpha = 25^\circ$. All experiments were performed at a Reynolds number of 15,000.

Experiments were performed in a large-scale water channel, which is shown in Figure F1b. The main test section of this facility had a width of 927 mm and a height of 610 mm; the water level was maintained at 547 mm. Upstream of this test section, a flow conditioning system involving honeycomb and a sequence of five screens provided a turbulence intensity of approximately 0.3%. The freestream velocity in the test section was maintained at 70.9 mm/sec. The water flow was seeded with 12 micron diameter metallic coated plastic spheres, with a sufficient density such that 15-20 particle images were typically attained within the interrogation window. The laser sheet was generated by a dual pulsed Yag laser system having a maximum output of 90 mJ. The pulse rate of the lasers was 30 Hz, and image pairs were acquired at a rate of 15 Hz.

The schematic of Figure F1b also shows the locations and orientations of the two cameras employed for stereo particle image velocimetry. The sensor array of each camera was 1008 x 1018 pixels. In order to minimize refraction effects, and thereby optimize the quality of the particle image patterns, a prism system was attached to the exterior of the test section of the water channel, also shown in Figure F1b. The designated prisms were constructed of 6 mm Plexiglas and filled with distilled water.

Satisfying the Scheimpflug condition in the presence a liquid-air interface does not necessarily yield optimal images due to radial distortion. Prasad and Jensen (1995) showed that the liquid prism is very efficient at reducing radial distortions arising from a liquid-air interface. Another major advantage of using the liquid prisms is that they provide paraxial recording so that no additional ray-tracing needs to be applied to reconstruct the three-dimensional displacement field.

Specifications of the parameters that define the sinusoidal leading edge are given in Figure F1c. The wavelength of the sinusoidal is λ and its peak to peak amplitude is ϕ , corresponding to an amplitude of $\phi/2$.

Images were acquired at a dimensionless distance from the surface of the wing, i.e., location of the laser sheet, at $z/C = 0.005$, defined in Figure F1a. A rigorous assessment of the effects of displacement of the laser sheet in the region close to the wing is provided by Gorunev (2008). In essence, in the very near-surface region, changes in elevation of the laser sheet yield only very small changes in the location and form of topological critical points.

Two general categories of patterns are of interest in this investigation. The primary focus is on patterns of surface topology in regions away from the leading-edge of the wing. These patterns are large-scale, and therefore relatively insensitive to grid size. The other category of patterns addresses the full structure along the sinusoidal leading-edge; in this region, the grid size must be sufficiently small relative to the wavelength of the edge. Taking into account the size of the interrogation window of 32 pixels x 32 pixels, and the standard 50% overlap in order to satisfy the Nyquist criterion, the effective grid size, i.e., the distance between velocity vectors, is $\Delta = 3.2$ mm in the present investigation, the wavelength of the leading-edge had values of 10, 20, 40, 80, and 160 mm, corresponding to the ratios of grid size to wavelength of $\Delta/\lambda = 0.32, 0.16, 0.08, 0.04$, and 0.02 . Clearly, for the largest values of $\Delta/\lambda = 0.32$ and 0.16 , patterns of velocity and vorticity will not adequately represent the flow structure along the sinusoidal leading-edge. For smaller values of $\Delta/\lambda = 0.08, 0.04$, and 0.02 , however, such patterns are reasonably approximated. Regarding the topological patterns along the surface of the link, link from the leading-edge, they scale according to the board of the wing, and the dimensionless grid size $\Delta/C = 0.016$ provides well-resolved topological patterns and critical points.

Images were evaluated using a frame-to-frame cross-correlation technique with a 32×32 pixel interrogation window and 50% overlap. The distance from the objective of each camera to the plane of the laser sheet at the center of the calibration target was 900 mm. Effective values of magnification and the grid size in the physical plane of the laser sheet were 5 pixels/mm and 0.0159 respectively. Resolution of the images of the flow field was optimized by acquiring images over half of the wing. Preliminary experiments, at the outset of this program, verified the symmetric of patterns with respect to the plane of symmetry of the wing with the straight leading edge. Time-averaged patterns of velocity vectors $\langle \mathbf{V} \rangle$ were obtained by averaging instantaneous velocity fields \mathbf{V} over the entire sequence of approximately 140 images. Other quantitative representations of the flow structure, such as time-averaged surface-normal vorticity ω , streamlines Ψ , and contours of constant out-of-plane velocity w were deduced from the time-averaged patterns of velocity vectors.

The uncertainty in the in-plane and out-of-plane velocity vectors was in the range of 1.5 to 2% and 3 to 4%, respectively. A direct comparison of the mean of the free-stream velocity obtained from previous single-camera particle image velocimetry results reveals 1.4% difference. Zang and Prasad (1997) provide a thorough error analysis for a Scheimpflug stereocamera system. The uncertainty in the surface-normal vorticity contours was within 4 to 5%. The reader

is referred to the paper by Fouras and Soria (1998) for a detailed analysis of the accuracy of the surface-normal vorticity measurements. The streamlines represent an integral of the velocity field, so the uncertainty of velocity would seem to be a conservative estimate of the uncertainty of the value of the stream function, which define the streamlines.

2. TOPOLOGICAL REPRESENTATIONS

Advancement of topological concepts, as well as topological analyses of smoke visualization of flow patterns away from a surface and oil patterns along a surface have seen remarkable advances in recent decades. These investigations include those of: Legendre (1956, 1977), Squire, Maltby, Keating and Stanbrook (1962), Perry and Fairlie (1974), Hunt, Abel, Peterka and Wu (1977), Tobak and Peake (1982), Dallman (1983), Perry and Hornung (1984), Perry and Chong (1987, 2000), Bakker and de Winkel (1990), Su, Liu and Liu (1990), Chong, Perry and Cantwell (1990), Chapman and Yates (1991), Delery (2001), Foss (2004), Gordnier and Visbal (2003), and Verhaagen and Bossuyt (2006). Particularly relevant to our present considerations is the investigation of Su, Liu and Liu (1990), who address skin friction patterns on delta wings of low and moderate sweep angles.

Recently, laser-based approaches have been employed to characterize the near-surface topology in relation to the near-surface flow structure and skin friction. Yavuz, Elkhoury and Rockwell (2004) related the near-surface topology on a delta wing at low sweep angle to surface-normal patterns of vorticity and near-surface velocity fluctuations. Depardon, Lasserre, Brizzi and Boree (2005) employed a near-surface PIV approach to characterize the patterns along four surfaces and in the wake of a surface mounted cube, and critically evaluated their findings in relation to the skin friction patterns obtained by oil visualization. An approach that employs PIV imaging as a basis for automated topology classification has been advanced by Depardon, Lasserre, Brizzi and Boree (2007).

Figure F2 shows generic categories of topological patterns involving negative and positive bifurcation lines, saddles of attachment and separation and stable and unstable foci and nodes. If the foci are located along a surface, then as indicated in the schematics, the stable focus is associated with a focus of separation, involving a streamline oriented away from the surface at the location of the focal point. Conversely, the unstable focus, is designated as a focus of attachment, whereby the streamline at the focal point is directed towards the surface. Comprehensive overviews of physical interpretations of critical points along a solid surface, in conjunction with either flow away from or towards the critical points, are provided by Bakker and de Winkel (1990) and Su, Liu and Liu (1990).

In the present investigation, these types of topological patterns will be employed to determine the effectiveness of modification of the leading edge of the delta wing. For example, in absence of edge modification, a large-scale focus of separation occurs; with a given sinusoidal leading edge, it is possible to transform the near-surface pattern to one that involves only a focus of attachment.

3. PATTERNS OF NEAR-SURFACE STREAMLINE TOPOLOGY AND FLOW STRUCTURE

Near-Surface Streamline Topology. Figure F3 shows patterns of near-surface streamline topology in relation to the dimensionless amplitude of the sinusoidal leading edge. In addition to

the amplitude ϕ/C and wavelength λ/C of the leading edge designated on each image, the ratio λ/ϕ is also indicated. The top left image in the layout of Figure F3 corresponds to the reference case of the delta wing with the straight leading edge, i.e., $\phi/C = 0$, $\lambda/C = \infty$. For subsequent images in the left column, then in the right column of Figure F3, values of increasing amplitude ϕ/C and wavelength λ/C are illustrated. For all images, at least one critical point, in the form of a positive focus F^+ , a negative focus F^- , or a node N^+ occurs. Moreover, a saddle point S is located near the intersection of the leading- and trailing edges. Furthermore, a negative bifurcation line BL^- , corresponding to the merging of streamlines, is identifiable over at least a portion of the leading edge in all images. Particularly important, however, is the manner in which the type and location of the foregoing critical points transform from one type to another as the parameters ϕ/C and λ/C are increased.

For the image with the straight leading edge $\phi/C = 0$ and $\lambda/C = \infty$, the negative bifurcation line BL^- is located along the leading edge. It represents the merging of streamlines emanating from the freestream together to form a single line along the leading edge. Immediately in-board of this BL^- , a line designated as B is indicated. Strictly speaking, it is not a classical bifurcation line BL^- ; rather the locus of extremely closely-spaced streamlines that eventually diverge in the region downstream of the apex of the wing. Moreover, the principal topological feature is a negative focus F^- , which represents the center of an inward-directed swirl pattern, also known as a stable focus. In accord with the representations of the critical points given in Figure F2, the direction of the surface-normal flow at F^- is away from the surface of the wing, and thereby represents a point of separation. Finally, a saddle point S is evident near the intersection of the leading- and trailing edges of the wing. It represents the locus of separating streamlines from the surface of the wing in the vicinity of intersection of leading- and trailing edges of the wing, and it is consistently encountered in the streamline topology of remaining configurations.

In next image, which represents $\phi/C = 0.01$ and $\lambda/C = 0.05$, the streamline topology shows a focus of separation F^- located near the apex; that is, the location of F^- has moved substantially upstream, relative to its location in the foregoing image representing $\phi/C = 0$ and $\lambda/C = \infty$. Furthermore, this F^- is located within a limit cycle L . The bifurcation line BL^- is located along the leading edge of the wing, as was the case for the preceding image $\phi/C = 0$ and $\lambda/C = \infty$. A significant distinction, however, is the negative bifurcation line BL^- in the present image is now oriented in the upstream direction, rather than in the downstream direction in the image representing $\phi/C = 0$, $\lambda/C = \infty$. The streamlines emanating from the freestream at $\phi/C = 0.01$ undergo an abrupt change in direction, as they approach the leading edge, in order to attain compatibility with the upstream-oriented bifurcation line BL^- . A saddle point S is still identifiable in the region near the intersection of the leading- and trailing edges of the wing. Taking all of the foregoing observations together, it is remarkable that such substantial changes in the near-surface streamline topology are attainable for such small amplitude $\phi/C = 0.01$ protuberances of the leading edge.

For a further increase in amplitude of the leading-edge sinusoid to a value $\phi/C = 0.02$, as indicated in the image at the bottom left of Figure F3, a dramatic change in the pattern of near-surface streamline topology occurs. The focus of separation F^- has transformed into a focus of attachment F^+ , and the limit cycle L no longer exists. This change indicates that the three-dimensional separation from the surface of the wing, associated with the presence of the focus of

separation F^- in the streamline topology, is no longer evident. The negative bifurcation line BL^- is still oriented in the upstream direction, as was the case for $\phi/C = 0.01$, and it is generally aligned with the troughs of the leading-edge sinusoid. Finally, the location of the saddle point S persists at the same position as in the foregoing images.

For the image at $\phi/C = 0.04$, shown at the top right of Figure F3, the focus of attachment F^+ has transformed into an inflected node of attachment N^+ . Regarding the negative bifurcation line BL^- , it is generally aligned with the troughs of the leading-edge sinusoid and remains oriented in the upstream direction. The location of the saddle point S is essentially the same as in preceding images.

For a still larger value of amplitude of the leading-edge sinusoid, represented by $\phi/C = 0.08$, the inflected node of attachment N^+ has transformed back into a focus of attachment F^+ , and its location is very close to the apex of the wing. The negative bifurcation line BL^- along the leading edge is well-defined only in the vicinity of the apex of the wing. At locations further downstream, it loses its distinctive character. The streamlines in those regions attempt to follow the sinusoidal undulation of the leading edge. Remarkably, a saddle point still persists near the trailing edge.

For the case of a large leading-edge sinusoid, corresponding to $\phi/C = 0.16$ and $\lambda/C = 0.4$, several foci F are evident. Close to the apex of the wing, a focus of attachment F_1^+ is evident, and, located further downstream, approximately aligned with the crests of the leading edge, are a second focus of attachment F_2^+ and a focus of separation F^- . Between these latter two foci, a saddle point S_2 occurs. Well-defined bifurcation lines BL^- are evident along sections of the leading edge. Near the trailing edge of the wing, the saddle point S_l persists.

Taken together, the images of Figure F3 indicate that the near-surface topology is highly sensitive to small values of, and small changes of, the amplitude ϕ/C of the sinusoidal undulation of the leading edge. As the amplitude ϕ/C increases, the focus of three-dimensional separation F^- moves towards the leading edge, and when ϕ/C attains a sufficiently large value, corresponding to only 2% of the chord of the wing, i.e., $\phi/C = 0.02$, the F^- is eliminated entirely; that is, it does not appear along the surface of the wing, and is replaced by a focus of attachment F^+ . With still further increases in amplitude ϕ/C , this critical point F^+ undergoes an intermediate transformation to an inflected node N^+ , which allows, for still further increases of ϕ/C , the focus of attachment F^+ to take a position very close to the apex of the wing. When ϕ/C becomes sufficiently large, however, there is a fundamental departure from the foregoing trend.

Multiple foci occur along the leading edge of the wing.

A further observation concerns the location and orientation of the negative bifurcation line BL^- along the leading edge. For even a small value of $\phi/C = 0.01$, the direction of BL^- switches to an orientation in the upstream direction, and this orientation is maintained for finite, but small values of ϕ/C . Another type of topological feature, a well-defined saddlepoint S , persists near the intersection of the leading- and trailing edges, irrespective of all of the foregoing, radical changes of the near-surface critical points.

A further point of interest is that each of the images of Figure F3 has a specified value of the ratio of the wavelength to the amplitude of the sinusoidal leading edge, λ/ϕ . This ratio has a value of 2.5 for those images that correspond to the largest alteration of the near-surface topology.

The alterations in the near-surface topology on the wing for various values of amplitude and wavelength involve either a decrease in the extent of three-dimensional separation or its elimination altogether. Considering that the lift coefficient would be relatively low in presence of the large-scale focus of separation, it is anticipated that the lift coefficient is higher for the cases at which the large-scale focus of separation is eliminated.

Miklosovic et al (2004) showed that the addition of sinusoidally-shaped leading-edge to a scale model of an idealized humpback whale flipper also decreased drag. Based on this finding, one might expect a similar decrease in the drag coefficient for the case of a delta wing of moderate sweep angle used in the present investigation.

Surface-Normal Vorticity. Patterns of near-surface vorticity ω , which is oriented normal to the surface of the wing, are given in Figure F4. For the case of the wing with the straight leading edge, $\phi/C = 0$, represented in the image at the upper left, a high vorticity gradient exists along the leading edge. This region is designated as a . Images in the left column of Figure F4, represent very small value of amplitudes $\phi/C = 0.01$ and 0.02 , and wavelength $\lambda/C = 0.05$, in accord with the image layout of Figure F3. The pattern of high gradient of vorticity remains distributed along the leading edge, keeping in mind that very small concentrations of vorticity, if they would exist, cannot be spatially resolved with the present imaging.

The top image in the right column of Figure F4 represents larger, but still small, values of amplitude $\phi/C = 0.04$ and wavelength $\lambda/C = 0.1$. Well-defined concentrations of vorticity are indeed evident. These concentrations are designated as a^* and their wavelength is the same as the wavelength of the sinusoidal leading edge. When the amplitude and wavelength of the leading edge are increased still further, to values $\phi/C = 0.08$ and $\lambda/C = 0.2$, two types of well-defined vorticity concentrations occur. The first is an elongated concentration designed as a_1^* , which forms on that portion of the sinusoidal leading edge that is approximately orthogonal to the incident free stream. The other type of concentration a_2^* forms along the troughs of the leading edge.

For large values of amplitude and wavelength, $\phi/C = 0.16$ and $\lambda/C = 0.4$, the concentration of the a_1^* is always distinguishable, whereas the concentration a_2^* is distinctly defined only at one location near the apex of the wing.

Surface-Normal Velocity. Figure F5 shows contours of constant time-averaged surface-normal (out-of-plane) velocity $\langle w/U \rangle$ corresponding to the images of Figures F3 and 4. The color red corresponds to a relatively large positive amplitude of $\langle w/U \rangle$, in a direction away from the surface of the wing, while dark blue represents a significant value of negative $\langle w/U \rangle$; that is, towards the surface of the wing. Such dark blue regions indicate the occurrence of flow reattachment to the surface of the wing. For the case of the straight leading edge $\phi/C = 0$, represented by the image at the top left of Figure F5, reattachment occurs near the plane of symmetry, and is confined to a region near the trailing edge of the wing. On the other hand, for all values of parameters of the sinusoidal leading edge, a region of dark blue contours occurs close to the plane of symmetry. It represents a relatively large magnitude of the component $\langle w/U \rangle$ towards the surface of the wing, and thereby a region of reattachment. As the value of ϕ/C increases from 0.01 to 0.04, the spatial extent of the dark blue region in the vicinity of the apex increases, and at a location further downstream, the transverse spatial extent of this region

decreases, then rapidly increases again as the trailing edge is approached. At $\phi/C = 0.08$, the transverse extent of this region is significantly large along the entire streamwise extent of the wing.

For the largest amplitude of the sinusoidal leading edge, $\phi/C = 0.16$, presented in Figure F5, a dark blue (negative) region of large extent exists near the apex of the wing, in conjunction with an elongated red (positive) region, which is indicative of a streamwise vortical flow that apparently occurs in conjunction with the reattachment process near the plane of symmetry. This interpretation is compatible with the pattern of surface-normal vorticity designated as b in Figure F4. It is aligned with the clusters of positive and negative $\langle w/U \rangle$, and corresponds to sweeping of fluid along the near-surface region, due to the streamwise vortical structure.

Viewing together all of the images of Figure F5, the existence and spatial extent of the region of negative $\langle w/U \rangle$ along the plane of symmetry of the wing may be taken as an indirect indicator of the effectiveness of the sinusoidal leading edge. That is, as already suggested by the corresponding patterns of topology given in Figure F3, very substantial changes in the topological features are induced, and these changes correspond to distinct regions of flow reattachment. In other words, the spatial extent of the region of flow reattachment near the plane of symmetry of the wing is substantially influenced by the sinusoidal leading edge.

Near-Surface Streamline Topology for Large Wavelength Leading Edges. Figure F6 shows patterns of near-surface topology for leading edges having relatively large wavelength λ/C . In all images, the streamline patterns include a focus of separation F^- located near mid-chord. It therefore appears that when the dimensionless wavelength λ/C is sufficiently large, it is not possible to eliminate the focus of separation F^- . It should be noted that the image at the upper right, which represents $\phi/C = 0.04$ and $\lambda/C = 0.8$, shows not only a focus of separation F^- , but also a focus of attachment F^+ . Furthermore, in all images of Figure F6, a negative bifurcation line BL^- is distinguishable. Furthermore, all images of Figure F6 show a saddle point S near the intersection of the leading- and trailing edges.

Viewing together all of the images of Figure F6, which are broadly similar, it appears that when the wavelength λ/C becomes sufficiently large, while the amplitude ϕ/C is maintained sufficiently small, there is not a substantial effect on the overall physics implied by the near-surface topology. It should be noted that the ratio of the wavelength to the amplitude λ/ϕ is specified for each of the sinusoidal leading edges in Figure F6. This ratio has values ranging from $\lambda/\phi = 5$ to 20, in comparison with the value of $\lambda/\phi = 2.5$, for which major changes in the surface topology were attained in Figure F3.

4. CONCLUSIONS

The near-surface flow patterns have been characterized for delta wings having sinusoidally-shaped leading edges of various values of amplitude and wavelength. The nominal value of (low) sweep angle is kept constant, and the wing is oriented at a high value of angle of attack. For the limiting case of the wing having a straight leading edge, large-scale, three-dimensional separation occurs. A technique of stereoscopic particle image velocimetry allows determination of the effect of the leading-edge geometry on the near-surface flow patterns, and in turn, the possibility of controlling the near-surface flow structure using this strictly passive technique. Patterns of streamline topology and the associated critical points are interpreted in conjunction with patterns of surface-normal vorticity and velocity. The principal findings are as follows:

1. The dimensionless ratio of wavelength to amplitude λ/ϕ of the sinusoidal leading edge was found to be a predominant parameter. The near-surface flow can be fundamentally altered for relatively small values of λ/ϕ . The largest changes were obtained by keeping the wavelength $\lambda/C = 0.16$ and the amplitude $\phi/C = 0.4$, which gives $\lambda/\phi = 2.5$.
2. For small values of λ/ϕ , as the (peak to peak) amplitude ϕ/C of the sinusoidal leading edge increases, the focus of three-dimensional separation F^- moves towards the leading edge, and when ϕ/C attains a sufficiently large value, corresponding to only 2% of the chord of the wing, i.e., $\phi/C = 0.02$, the F^- is eliminated, and replaced by a focus of attachment F^+ . At a larger value of $\phi/C = 0.08$, the focus of attachment F^+ moves to a position very close to the apex of the wing.
3. For the range of amplitude ϕ/C of the sinusoidal leading edge indicated in the foregoing, the patterns of surface-normal vorticity at the meeting-edge take on distinctive forms, ranging from distributed vorticity contours having high gradients at the leading edge, to single, then dual concentrations of vorticity at successively larger values of ϕ/C . These patterns of vorticity represent the initial conditions of the separating shear layer from the leading edge.
4. Corresponding patterns of surface-normal velocity indicate the onset of a pronounced region of flow reattachment close to the plane of symmetry of the wing, and extending over nearly the entire chord of the wing, for those cases where substantial changes in the near-surface topology are attained.

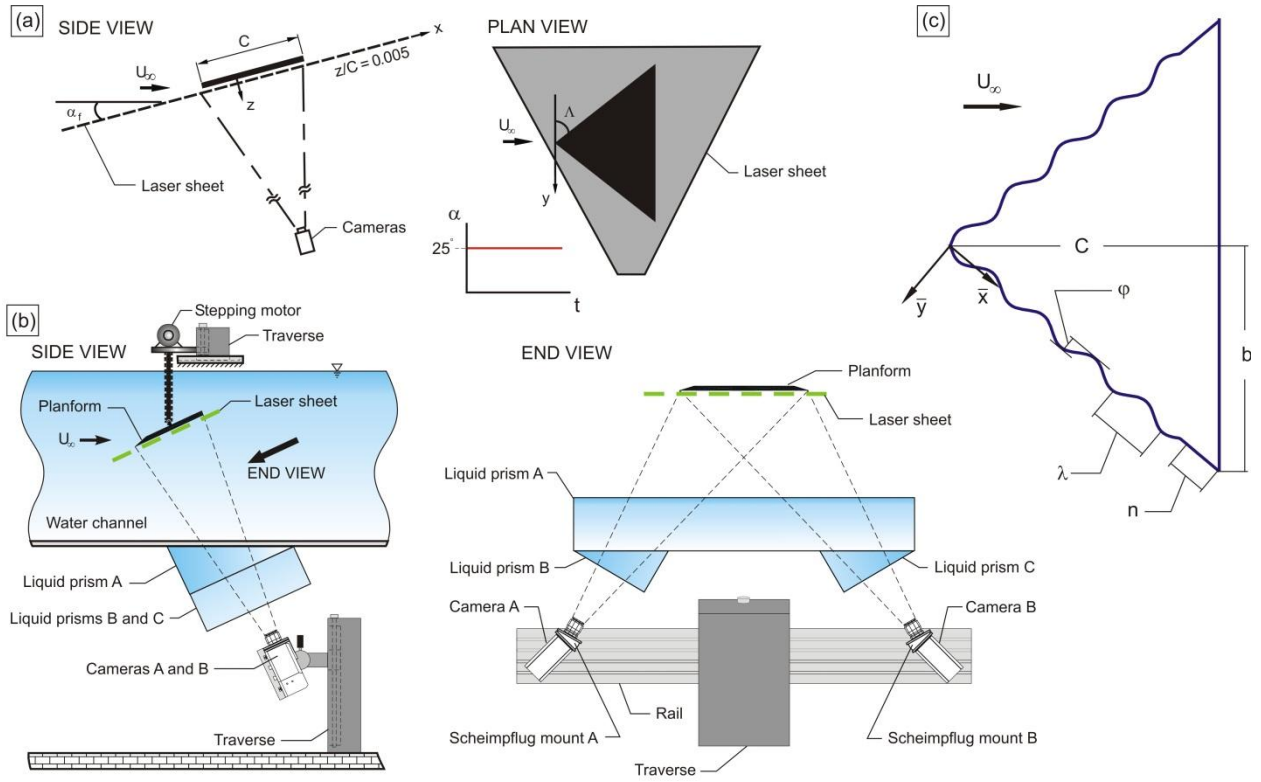


Figure F1 **a** Overview of delta wing and laser sheet orientation for stereo imaging. **b** details of stereo imaging system, and **c** definitions of parameters for sinusoidal leading-edge delta wing.

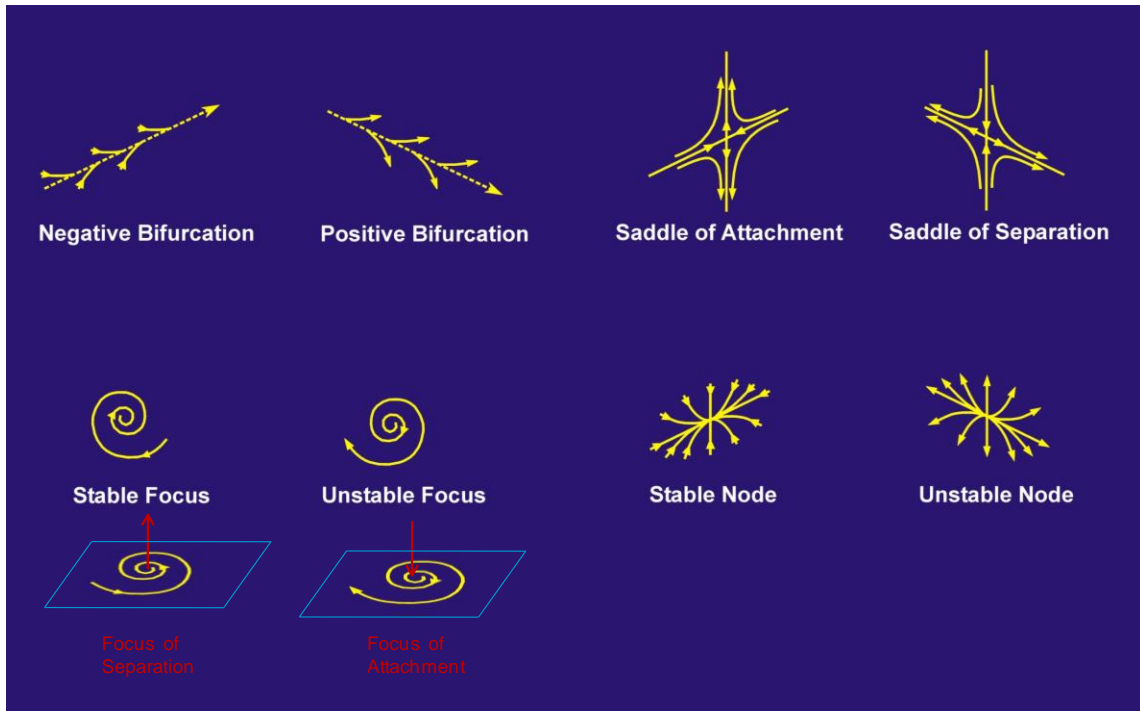


Figure F2: Overview of basic classes of critical points of flow topology

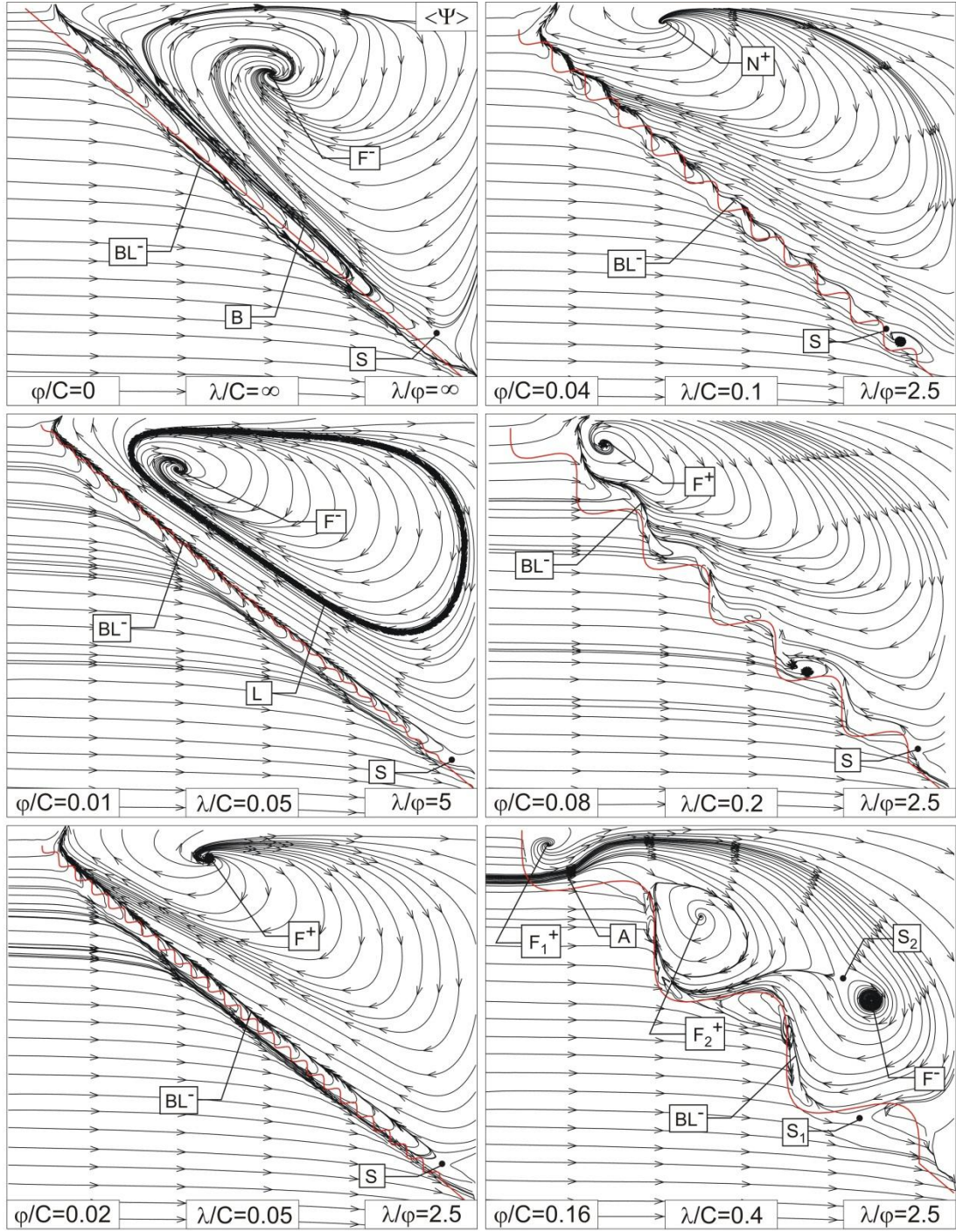


Figure F3: Patterns of time-averaged near-surface streamline topology $\langle \Psi \rangle$ on stationary wing for various values of amplitude ϕ and wavelength λ . The angle-of-attack α is 25°

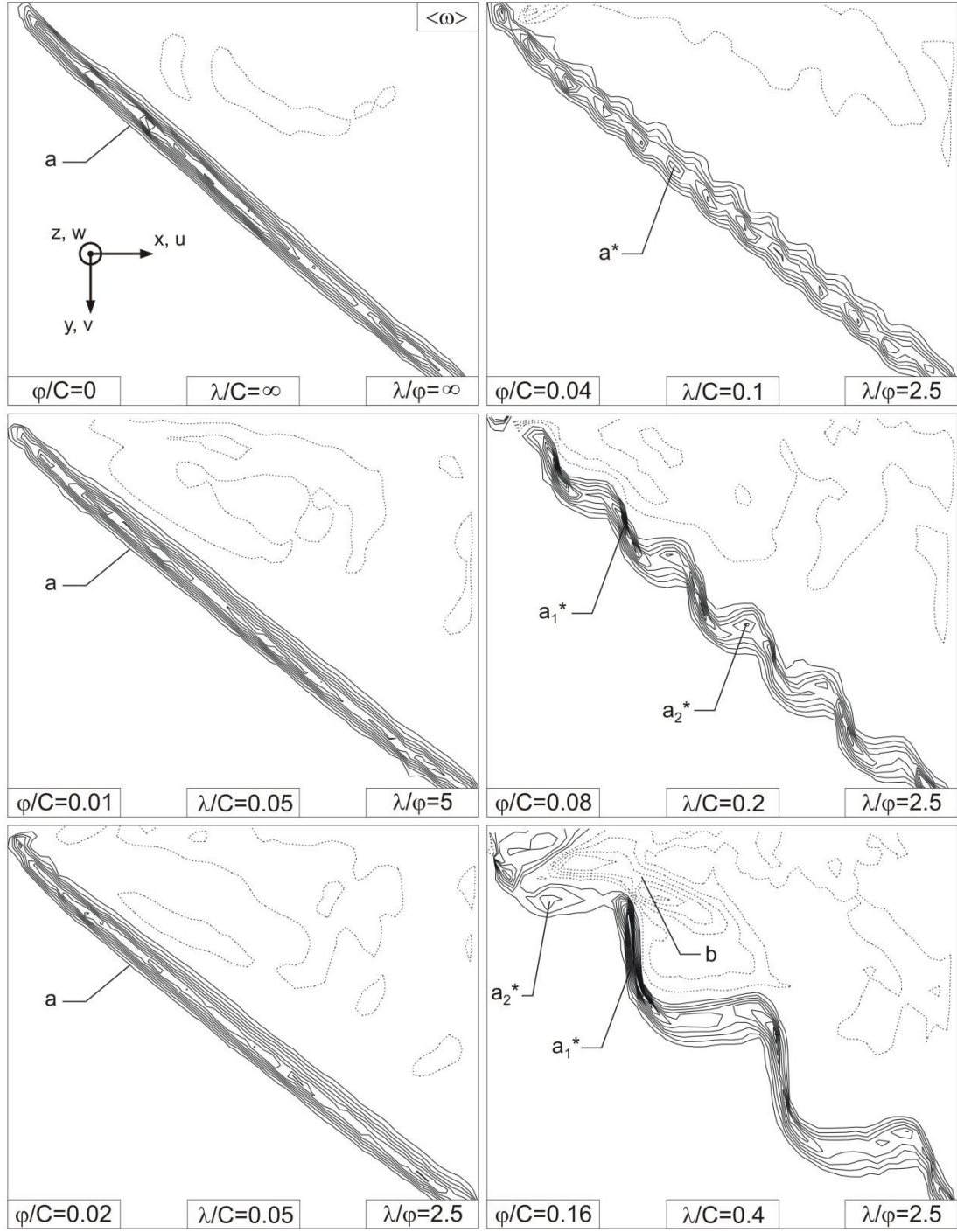


Figure F4: Patterns of time-averaged near-surface vorticity $\langle \omega \rangle$ oriented normal to the surface of the stationary wing for various values of amplitude ϕ and wavelength λ . Minimum and incremental values of vorticity are $\omega_{\min} = 1 \text{ s}^{-1}$ and $\Delta\omega = 1 \text{ s}^{-1}$, respectively. The angle-of-attack α is 25°

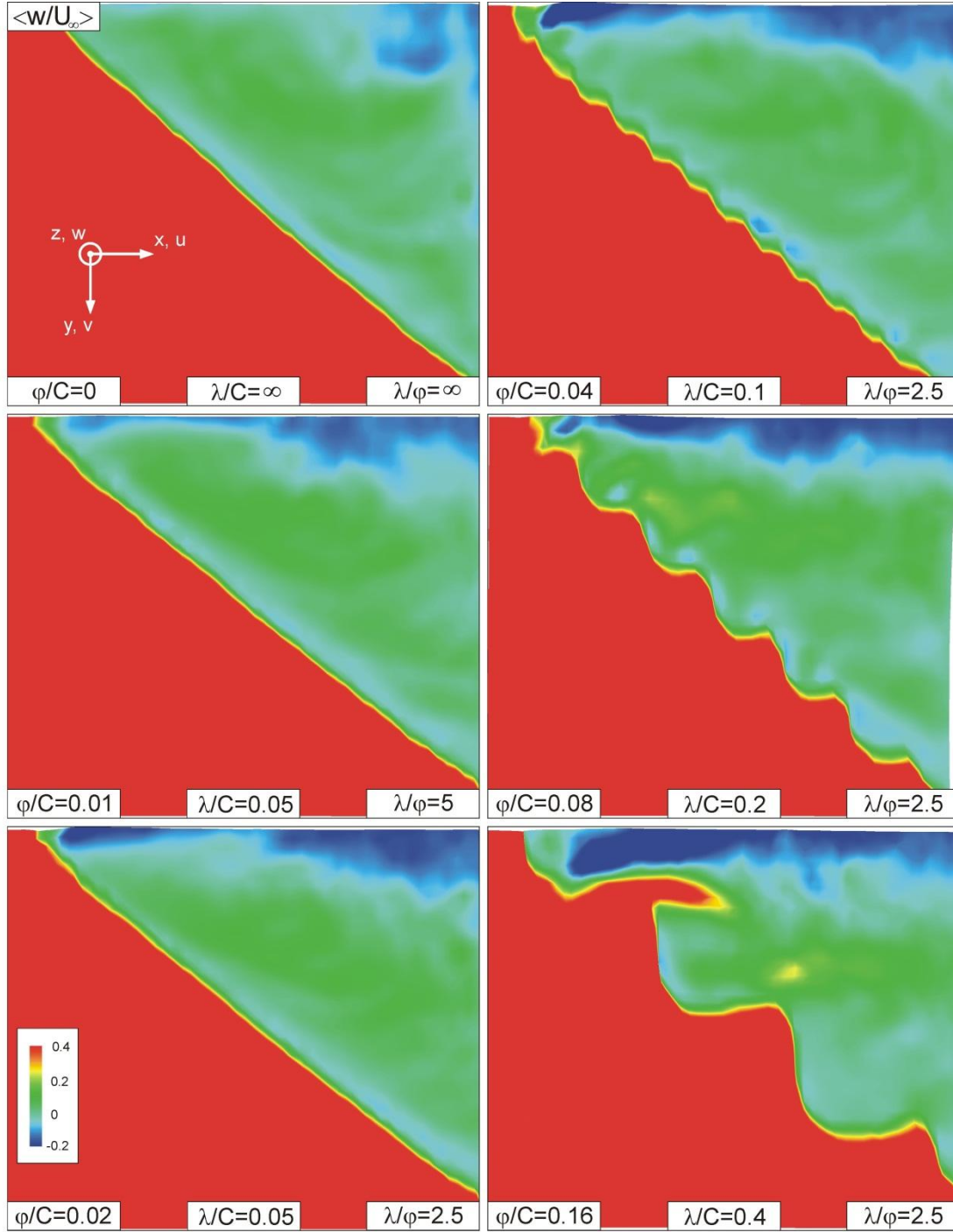


Figure F4: Constant contours of time-averaged out-of-plan velocity $\langle w/U \rangle$ on the near-surface plane of stationary wing for various values of amplitude ϕ and wavelength λ . The angle-of-attack α is 25° . Color *blue* represents flow toward surface of wing

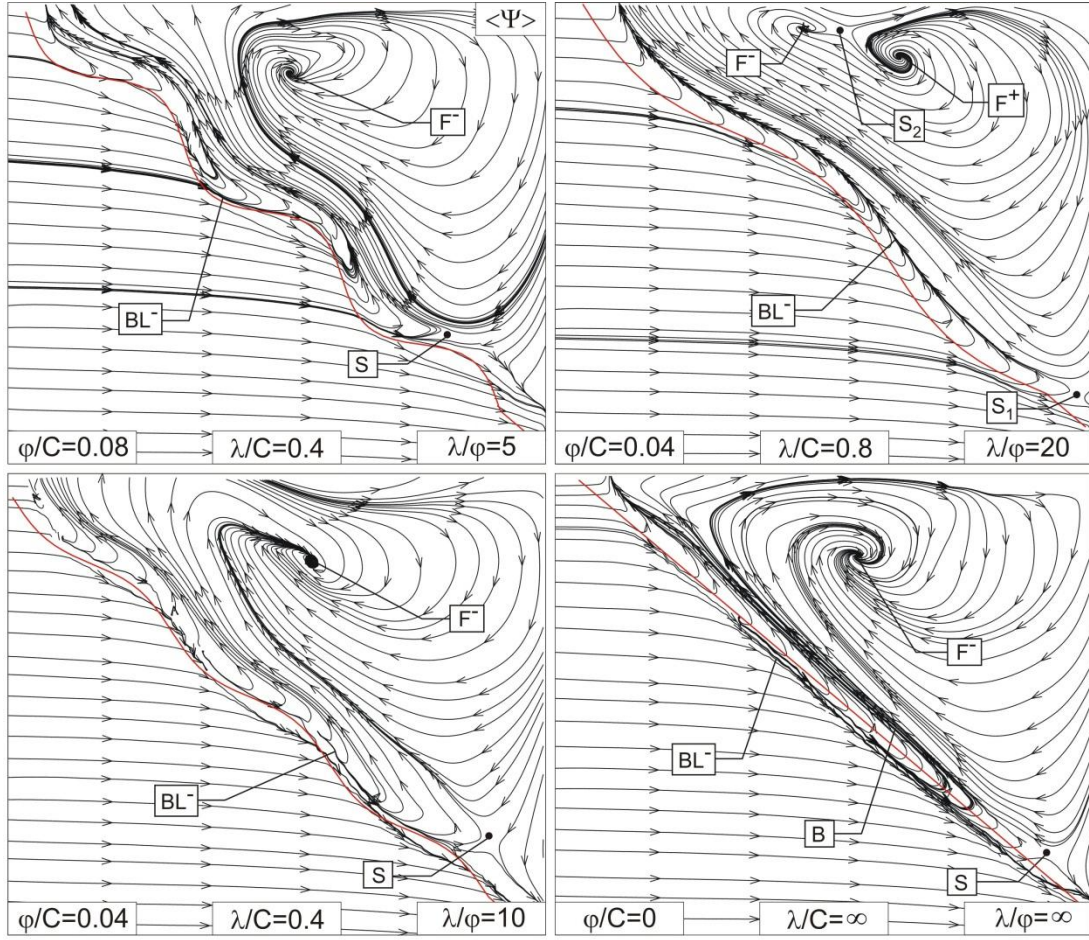


Figure F6: Patterns of time-averaged near-surface streamline topology $\langle \Psi \rangle$ on stationary wing for various values of amplitude ϕ and wavelength λ . The angle-of-attack α is 25°

APPENDIX G

EFFECT OF PITCH RATE ON NEAR-SURFACE TOPOLOGY ON A DELTA WING

ABSTRACT

The near-surface flow structure and topology on a delta wing of moderate sweep angle are investigated using a technique of high-image-density digital particle image velocimetry (DPIV). The focus is on the time evolution of the surface topology during relaxation of the flow after termination of a pitching maneuver, for a wide range of pitch rates. The near-surface patterns at the instant corresponding to termination of the maneuver are a strong function of the magnitude of pitch rate, and show substantial differences. On the other hand, irrespective of the severity of the flow distortion at the end of the pitching maneuver, the relaxation of the flow involves the same sequence of universal topological states. Furthermore, it is demonstrated that there exists a critical universal state, which marks an abrupt transformation between two distinctly different states of the near-surface topology. Moreover, it is demonstrated that the changes of the topological features observed during the early stages of the relaxation process are analogous to the alterations of the surface patterns obtained for the stationary wing at smaller angles-of-attack.

1. EXPERIMENTAL SYSTEM AND TECHNIQUES

An overview of the experimental setup is given in Figure G1. The sweep angle of the delta wing had a value of $\Lambda = 50^\circ$. The root chord of the wing was $C = 200$ mm, and the wing thickness was 6.35 mm, with 30° beveling on the windward side. All experiments were performed at a Reynolds number of 15,000.

Experiments were performed in a large-scale water channel. The main test section of this facility had a width of 927 mm and a height of 610 mm; the water level was maintained at 547 mm. Upstream of this test section, a flow conditioning system involving honeycomb and a sequence of five screens provided a turbulence intensity of approximately 0.3%. The freestream velocity in the test section was maintained at 70.9 mm/sec. The water flow was seeded with 12 micron diameter metallic coated plastic spheres, with a sufficient density such that 15-20 particle images were typically attained within the interrogation window. The laser sheet was generated by a dual pulsed Yag laser system having a maximum output of 50 mJ. The pulse rate of the lasers was 15 Hz. Images during the entire relaxation process were acquired at effective rates of 15 and 5 frames per second. Using a lower framing rate allowed sufficiently long image capture time, in order to characterize the flow during the relatively later stages of relaxation.

The schematic of Figure G1 also shows the location and orientation of the camera employed for digital particle image velocimetry. The sensor array of the camera was 1008 x 1018 pixels. In order to minimize refraction effects, and thereby optimize the quality of the particle image patterns, a prism was attached to the exterior of the test section of the water channel, also shown in Figure G1. The designated prism was constructed of 3 mm Plexiglas and filled with distilled water.

For the case of the maneuvering wing experiments, a linear ramp-like pitching motion was applied between the initial and final angles-of-attack for a wide range of pitch rate. Sequential images were recorded upon completion of the pitching maneuver at an angle-of-attack of 25° , in order to characterize the relaxation process.

The following parameter was defined for the pitch rate during pitching maneuver:

$$\frac{\dot{\alpha} C}{U_\infty} = \left(\frac{\Delta \alpha}{\Delta t} \right) \left(\frac{C}{U_\infty} \right)$$

where $\Delta \alpha = \alpha_f - \alpha_i$, and Δt is the time difference between the initial and final values of angle-of-attack, defined respectively as $\alpha_i = 5^\circ$ and $\alpha_f = 25^\circ$. Actual pitch rates of an unmanned combat air vehicle during a maneuver, $\dot{\alpha} C / U_\infty = 0.1$ and 0.2 , were considered when defining parameters of the pitching motion. Four different pitch rates were employed, $\dot{\alpha} C / U_\infty = 0.05, 0.1, 0.2$, and 0.4 . The elapsed actual time t' is normalized by U_∞ / C to obtain $t^* = t' U_\infty / C$, where $t' = 0$ or $t^* = 0$ corresponds to the termination of the pitching maneuver.

For the stationary wing experiments, images were recorded at three different values of angle-of-attack, $\alpha = 5^\circ, 15^\circ$ and 25° . An overview of the stationary wing experiments is given in Figure G1.

Images were acquired at a dimensionless distance from the surface of the wing, i.e., location of the laser sheet, at $z/C = 0.005$. In essence, in the very near-surface region, changes in elevation of the laser sheet yield only very small changes in the location and form of topological critical points.

Images were evaluated using a frame-to-frame cross-correlation technique with a 32×32 pixel interrogation window and 50% overlap. The distance from the objective of the camera to the plane of the laser sheet was 1125 mm. Effective values of magnification and the grid size in the physical plane of the laser sheet were 4 pixels/mm and 0.02 respectively. Resolution of the images of the flow field was optimized by acquiring images over half of the wing. Preliminary experiments, at the outset of this program, verified the symmetric of patterns with respect to the plane of symmetry of the wing. Time-averaged patterns of velocity vectors $\langle \underline{V} \rangle$ were obtained by averaging instantaneous velocity fields \underline{V} over the entire sequence of approximately 200 images. Other quantitative representations of the flow structure, such as instantaneous and time-averaged streamlines Ψ were deduced from the patterns of velocity vectors.

Regarding qualitative representation of the flow patterns, dye visualization was employed to complement the digital particle image velocimetry technique.

2. TIME EVOLUTION OF FLOW STRUCTURE DUE TO PITCHING MOTION

Patterns of Sequential States during Relaxation Process. Relaxation of the flow patterns after the end of the maneuver are indicated by the dye visualization of Figure G2. The time sequence of images is designated as $t' = 0$ through 17, where t' corresponds to the actual time in

seconds. The dimensionless time t^* following termination of the pitch-up maneuver is defined as $t^* = t' U_\infty / C$. Values of both t' and t^* are designated on each of the images. The red flow pattern located at the bottom right corner of Figure G2 corresponds to the stationary wing which represents the relaxed flow.

The relaxation process shows distinctive types of flow patterns. During the first stage of relaxation, the generic feature is upstream movement of the location of vortex breakdown, which ends with breakdown at the apex of the wing, indicated in the image $t' = 4$. This instant might be called a critical stage of the relaxation process, whereby the leading-edge vortex loses its characteristics. In image $t' = 11$, reverse flow is clearly evident in regions close to the leading-edge of the planform. At $t' = 17$, relaxation of the flow patterns is nearly achieved, and the flow structure closely resembles that of the stationary case. The dye marker covers nearly the entire planform, and clearly indicates the existence of large-scale stall.

The relaxation process can be defined in terms of sequential states of the quantitative near-surface patterns given in Figures G3 and G4 for a value of pitch rate $\dot{\alpha} C / U_\infty = 0.2$. The time t' elapsed after the termination of pitching motion is normalized by U_∞ / C , where U_∞ is the freestream velocity and C is the wing chord, to give $t^* = t' U_\infty / C$. The images at $t^* = 0$ in Figures G3 and G4 correspond to the time at which the pitching motion ends; these, as well as all subsequent images, are therefore acquired at the same angle-of-attack of 25° . The images at a sufficiently long time $t^* = 13.65$ after termination of the wing motion represent the relaxed state of the flow, where the flow structure closely resembles that of the stationary case shown in the bottom right corner of Figures G14 and G15. The five images at values of t^* extending from $t^* = 0$ and 13.65, shown in Figures G3 and G4, define the distinct patterns, or states, of the near-surface flow structure during the relaxation process.

Figure G3 shows the near-surface patterns of instantaneous velocity vectors. The flow direction is from left to right. Only half wing is shown due to symmetry. The apex of delta wing is located in the top left corner in all five images, and the leading-edge extends diagonally across each image.

Generally speaking, the high magnitudes of the velocity patterns at the termination of maneuver, $t^* = 0$, start to fade out as the flow relaxes, and finally, at the relaxed state, $t^* = 13.65$, the patterns of low velocity magnitude rotate in the clockwise direction, i.e., they form a low magnitude recirculation zone along the wing surface, which indicates the existence of stall.

More specifically, at $t^* = 0$, a jet like flow along the leading-edge vortex is evident, and there is no reverse flow on the wing surface. At this instant, the velocity magnitudes along the wing surface are much larger than the magnitudes in the free stream. The leading-edge vortex induces this region of large magnitude along the surface. At $t^* = 2.11$, small-scale recirculation zones start to appear close to the leading-edge, while at the location close to the plane of symmetry of the wing, velocity vectors of substantial magnitude are oriented in the streamwise direction.

At $t^* = 4.33$, however, there appears to be a well-defined reverse flow with significant velocity magnitude along the leading-edge directed towards the apex of the wing. In addition, close to the apex, a reduction in the magnitude of velocity vectors is evident, relative to the magnitudes that exist in the images at earlier times $t^* = 0$ and 2.11. At $t^* = 9.22$, the magnitude of the reverse flow along the leading-edge decreases and a recirculation pattern becomes evident at about the mid-chord. Furthermore, the velocity magnitudes have become dramatically smaller over the region of the wing inboard of the leading-edge.

Finally, the image at $t^* = 13.65$ indicates that the recirculation pattern later forms into a well-defined swirl pattern with extremely low velocity magnitudes, representative of stall.

Considering the entire set of images of Figure G3, and cross-comparing them with the dye visualization of Figure G2, it can be stated that the dramatic decrease in the near-surface velocity magnitudes, appearing after $t^* = 2.11$ (in Figure G3) and $t' = 6$ (in Figure G2), is an outcome of the leading-edge vortex losing its characteristics when breakdown occurs at the apex of the wing. In essence, the reduction of velocity magnitudes along the wing surface is the footprint of the loss of a defined structure of the leading-edge vortex.

Further insight into the flow structure during the relaxation process is provided by patterns of near-surface streamline topology and associated critical points given in Figure G4, which complement the aforementioned patterns of dye visualization and near-surface velocity vectors.

The image at $t^* = 0$ represents the first state, i.e., state 1 of the near-surface topology. A negative bifurcation line BL^- located along the leading-edge is oriented in the downstream direction, and there is a positive bifurcation line-like pattern A originating from the apex of the wing. The negative bifurcation line BL^- represents two-dimensional separation whereas the positive bifurcation-like line A indicates reattachment. The footprint of the leading-edge vortex on the wing surface is represented by the orientation of the streamlines from location A towards the leading-edge.

In state 2, at $t^* = 2.11$, a substantial number of small-scale foci F , saddles S and nodes N appear close to the leading-edge, which indicate the presence of small-scale instabilities in the flow. The positive bifurcation line-like structure A , evident at $t^* = 0$, is still detectable. This state 2 of the flow topology at $t^* = 2.11$ is believed to be the most critical one, because it corresponds to transition to the next state, which is substantially different. The small-scale distortions represented by the critical points F , S , and N along the leading-edge at $t^* = 2.11$ are associated with loss of identity of the leading-edge vortex, due to the occurrence of breakdown at the apex. State 3 corresponds to the image at $t^* = 4.33$ in Figure G4. A distinctive feature is a well-defined reverse flow along the leading-edge of the wing. Two different negative bifurcation lines, BL_A^- and BL_B^- , are visible; they indicate different regions of two-dimensional separation. Also, the positive bifurcation line-like structure A observed in states 1 and 2 at earlier times is replaced by a pattern of streamlines emanating from a single node N of attachment.

In state 4 at $t^* = 9.22$, the relatively narrow zone of reverse flow along the leading-edge, indicated in the aforementioned state 3, broadens substantially. This process is accompanied by the onset of a large-scale recirculation pattern that appears well inboard of the leading-edge. A small-scale node N of separation appears within this recirculation pattern. In addition, a saddle point S is present close to the intersection of leading- and trailing-edges.

In state 5, at $t^* = 13.65$, the recirculation pattern shown at $t^* = 9.22$ has evolved into a coherent, large-scale swirl pattern with a well-defined center, i.e., focus F of separation, which indicates the occurrence of a three-dimensional separation associated with the onset of stall along the wing surface. The location of the saddle point S remains the same as in the previous state 4. In this state 5, the flow has essentially relaxed and its structure closely resembles that of the stationary case, as shown in Figure G14.

3. EFFECT OF PITCH RATE

The effect of pitch rate on the time evolution of the flow structure was demonstrated during the relaxation process following the cessation of pitching motion. Four different pitch rates were investigated.

It turns out that, irrespective of the severity of the flow distortion at the end of the pitching maneuver, the relaxation of the flow involves the same sequence of flow states. It is demonstrated that the time delay to occurrence of the first state is very sensitive to the pitch rate. The delay between subsequent states is, however, nearly independent of pitch rate.

Patterns at Termination of Pitching Maneuver. It is known that a single leading-edge vortex, in its breakdown state, will eventually transform to a region of three-dimensional separation. This transformation starts with upstream movement of vortex breakdown towards the apex. Once it reaches the apex, the leading-edge vortex loses its characteristics. A reverse flow close to the leading-edge becomes evident, and it later transforms to large-scale separation from the surface. Then the flow relaxes, and its structure closely resembles that of the stationary case.

Figure G5 shows dye visualization at termination of the pitching maneuver for all pitch rates investigated in this study. Due to symmetry, only half of the wing is shown. At termination of the maneuver, i.e., at angle-of-attack of 25° , the flow starts to relax towards the steady state. Generally speaking, the single leading-edge vortex is evident, to varying degrees, at all pitch rates.

At the minimum pitch rate, $\dot{\alpha}_C / U_\infty = 0.05$, where the severity of the flow distortion is minimal, the vortex is evident only near the apex; the occurrence of large-scale separation generates a diffuse dye pattern. For increasing pitch rate, the onset of large-scale vortex breakdown moves towards the trailing-edge. For the case of maximum pitch rate, $\dot{\alpha}_C / U_\infty = 0.4$, the leading-edge vortex is in its early stages of formation; the relatively high level of flow distortion causes a discontinuity in the dye pattern.

Figure G6 shows corresponding patterns of instantaneous velocity vectors at termination of the pitching maneuver for all pitch rates. They are distinctly different. For example, the spatial

extent of the region of low magnitude velocity, which is located between the leading-edge and the high magnitude velocity vectors, decreases with increasing pitch rate. Also, a stagnant region is located close to the plane of symmetry at the trailing-edge, except for the case of the minimum pitch rate. In essence, a jet-like flow pattern of velocity vectors is evident for all pitch rates. It is deflected towards the leading-edge for increasing pitch rate. The aforementioned observations can be correlated with the early onset of vortex breakdown, and loss of identity of the leading-edge vortex, shown in the dye visualization of Figure G5. This phenomenon can be explained by the fact that the flow patterns at relatively high pitch rates of $\dot{\alpha}_C / U_\infty = 0.1, 0.2,$ and 0.4 , eventually converge to the pattern at $\dot{\alpha}_C / U_\infty = 0.05$ at some time during relaxation process.

Corresponding patterns of instantaneous streamline topology at the termination of the maneuver, which are given in Figure G7, show several distinctions. The angle between the plane of symmetry of the wing and the pattern of diverging streamlines, designated by the symbol A , increases, and the extent of the region enclosed by this streamline pattern and the leading-edge decreases as the magnitude of the pitch rate $\dot{\alpha}_C / U_\infty$ increases.

Figure G7 shows existence of a bifurcation line BL^- along the leading-edge of the wing for all values of pitch rate $\dot{\alpha}_C / U_\infty$. The length of this line varies, however, with pitch rate. At $\dot{\alpha}_C / U_\infty = 0.05$, it is relatively short and located close to the apex. At higher values of pitch rate $\dot{\alpha}_C / U_\infty = 0.2$ and 0.4 , it extends along the entire leading-edge of the wing. The negative bifurcation line BL^- for relatively small pitch rates $\dot{\alpha}_C / U_\infty = 0.05$ and 0.1 can be correlated with the early onset of vortex breakdown. As shown in the top two images of Figure G7, the large-scale burst region of the vortex interacts with the leading-edge separation region, and causes the bifurcation line BL^- from extending along the entire leading-edge.

Figure G7 also shows additional topological features and critical points. The number of critical points decreases with increasing pitch rate. This observation is consistent with the early onset of vortex breakdown at the two lowest values of pitch rate shown in Figure G5. As the value of $\dot{\alpha}_C / U_\infty$ becomes larger, the number of critical points decreases until, at the largest value of $\dot{\alpha}_C / U_\infty$, no saddle points S or foci F exist along the leading-edge. The highest pitch rate correlates with the dye visualization image at $\dot{\alpha}_C / U_\infty = 0.4$ in Figure G5, which involves formation of the leading-edge vortex following severe flow distortion upon cessation of the maneuver.

Patterns during Relaxation Process. Figures G5 through G7 show that variations of the pitch rate produce substantially different near-surface flow patterns and topologies, at the instant corresponding to termination of the maneuver. As the flow relaxes from these substantially different initial states, the near-surface topology may pass through a sequence of states, in a manner analogous to the relaxation process shown in Figures G3 and G4. It may be possible to identify the same states, occurring in an ordered sequence, irrespective of the different initial states produced by different pitch rates. If this can be achieved, it would be possible to define a set of universal states, which would expedite interpretation and analysis of the relaxation process. It is anticipated that such universal states would occur at different time delays after

termination of different pitch-up maneuvers. Such states would therefore provide a basis for analyzing the dimensionless time delays.

To illustrate the possibility that the same topological states can occur for different initial conditions, i.e., different states of the flow at the completion of different pitch-up maneuvers, the time sequence of topologies was examined for all of the pitch rates defined in Figure G7, and each sequence was searched for a state similar to state 3 indicated in Figure G4. Figure G8 compares the near-surface patterns of instantaneous streamline topology in state 3. The critical points and topological features are indicated. Close to the apex, a node N of attachment is evident in all cases, whereby streamlines emanate from the nodal location N . For all cases, two negative bifurcation lines BL_A^- and BL_B^- located along the leading-edge are distinguished by the subscripts A and B, which indicate two-dimensional separation zones. Again, a saddle S is evident for all pitch rates in the vicinity of the intersection of the leading-edge and the trailing-edge. The process described in the foregoing was followed for identification of the states 1, 2, 4 and 5, defined in Figure G4, and they were compared in a similar fashion as for Figure G8. Due to space limitations, these comparisons are not included herein. It was found that the types and locations of the critical points were very similar for each of the states 1, 2, 4 and 5, irrespective of the value of pitch rate, or, in other words, the patterns of near-surface topology in a given state are independent of the degree of flow distortion at the end of the maneuver. Henceforth, these very similar states are referred to as universal states.

4. DEFINITION OF UNIVERSAL STATES BASED ON CRITICAL POINTS AND THEIR TIME DELAY DURING RELAXATION

Definition of Universal States. Figure G9 shows the principal topological features and critical points of the near-surface patterns for the five different universal states described in the previous section. Their physical interpretation is the same as for the sequence of images given in Figure G4. These five universal states define the essential features of the time evolution of the flow structure on a delta wing of moderate sweep angle, for pitch rates that extend over an eightfold range.

State 1 in Figure G9 includes a positive bifurcation line-like pattern A originating from the apex, a saddle point S located close to the intersection of leading- and trailing-edges, and a negative bifurcation line BL^- along the leading-edge, having a length of approximately one third the length of the leading-edge.

State 2 involves the same positive bifurcation line-like pattern A near the plane of symmetry of the wing and a negative bifurcation line BL^- along the leading-edge, of smaller length relative to that of state 1. In addition, there are a number of small-scale foci of separation F^- and two saddle points S along the leading-edge. These patterns of critical points represent the transition between the pattern of state 1 and a fundamentally different pattern of state 3. In state 3, designated in Figure G9, the positive bifurcation line-like pattern A is no longer visible. Instead, a well-defined node of attachment N^+ is present. A radical change compared to the previous states is that the negative bifurcation line BL^- is now oriented in the upstream direction towards the apex and its length has increased.

The patterns of critical points in state 4 represent the transition between the pattern of state 3 and a fundamentally different pattern of state 5. There are two small-scale negative bifurcation lines BL_A^- and BL_B^- close to the center and the apex of the wing, indicated with subscripts A and B respectively. The well-defined node of attachment N^+ of state 3 moves further towards the center of the wing, and it is no longer well-defined. The location of the saddle point S moves closer to the intersection of leading- and trailing-edges.

State 5 is the final state. It occurs as an instant close to the completion of the relaxation process. This state closely resembles the steady state pattern, which includes a large-scale swirl pattern with a well-defined center, i.e. focus of separation F^- , located at approximately two thirds of the chord. The location of the saddle point S , present in state 4, remains the same, and there is a very small negative bifurcation line BL^- close to the apex.

Time Delays for Onset of Universal States. Although the same universal states occur in an ordered sequence for each pitch rate, the time delay from termination of the motion to their onset is expected to depend on the value of dimensionless pitch rate $\dot{\alpha}_C / U_\infty$. Figure G10 shows the angle-of-attack as function of time during and after the pitching maneuver for all pitch rates. The times of occurrence of the universal states at each value of pitch rate are indicated with a different color and a different symbol. For example, blue diamonds represent $\dot{\alpha}_C / U_\infty = 0.05$, green squares represent $\dot{\alpha}_C / U_\infty = 0.1$, orange circles represent $\dot{\alpha}_C / U_\infty = 0.2$, and red triangles represent $\dot{\alpha}_C / U_\infty = 0.4$. The time difference between two consecutive states is indicated as $(t_{i \rightarrow i+1})^{\dot{\alpha}_C / U_\infty}$, where the subscript i refers to the universal state number, and the superscript represents the pitch rate. For example, the time to go from state 2 to state 3 for the pitch rate of 0.2 is indicated as $(t_{2 \rightarrow 3})^{0.2}$.

Five different universal states, as defined previously, can be observed for each pitch rate, except for state 5 at the maximum pitch rate of $\dot{\alpha}_C / U_\infty = 0.4$, because of insufficient image capturing time. These states involve the distinct patterns defined in Figure G9.

For all values of pitch rate, at and after state 5, the flow is fully relaxed and the flow patterns have essentially converged to a steady state. For the minimum pitch rate of $\dot{\alpha}_C / U_\infty = 0.05$, the flow distortion is minimal at the end of the maneuver, and state 1 is defined to be the pattern of near-surface topology that occurs at termination of the pitching maneuver. At successively larger values of pitch rate, the time elapsed between the termination of maneuver and the occurrence of the universal state 1 increases dramatically. In order to more effectively interpret Figure G10, the following operator is applied to the time axis to convert t to t^+ :

$$t_{(n)}^+ = t_{(n)} - \frac{\sum_{i=1}^{n-1} \sum_{j=1}^{m=4} t_{(i) \rightarrow (i+1)} 2^{i-1 \cdot 0.05}}{m}$$

$$n = 2, 3, 4, 5$$

Figure G11 shows another interpretation of the information given in Figure G10, obtained from applying the aforementioned operator. As shown, all universal states tend to fall on a time band of nearly constant thickness, except for the state 4 at two values of pitch rate. These slight deviations are due to the fact that the universal state 4 is a transitional state from state 3 to 5, and there are slight discrepancies in the types and locations of its topological features and critical points.

The fact that all universal states fall on a time band of nearly constant thickness shows that the time delay between subsequent states is nearly independent of pitch rate. In other words, the time delay between universal state 1 and universal state 5, i.e. relaxation, is practically constant for all pitch rates.

The time elapsed between termination of the pitch-up maneuver and the occurrence of universal state 1 is given in Figure G12 for all values of pitch rate. It is clear that the variation of elapsed time is not linear.

In universal state 5, three-dimensional separation and stall occur on the wing. The time elapsed between the termination of the pitching maneuver and occurrence of universal state 5 can be defined as the time delay for the occurrence of large-scale, three-dimensional separation, and thereby the onset of stall, t_{stall} . The value of t_{stall} is the sum of the time between termination of the maneuver and the occurrence of universal state 1, and the time between the occurrence of universal states 1 and 5. As shown in Figure G11, the time between the occurrence of universal states 1 and 5 is constant for all pitch rates. The time between termination of the maneuver and universal state 1, however, is not constant, but can be estimated for various pitch rates with the simple curve fit shown in Figure G12. This approach is useful in predicting the time delay for the onset of stall, t_{stall} , for a wide range of pitch rate.

In conclusion, irrespective of the severity of the flow distortion at the end of the pitching maneuver, the relaxation of the flow involves the same sequence of universal states. The time delay to occurrence of the first universal state is very sensitive to the pitch rate. The delay between subsequent states is, however, nearly independent of pitch rate. An approach is introduced for predicting the time delay from termination of the maneuver to onset of three-dimensional separation and stall on delta wings of moderate sweep angle.

5. RELATION OF TIME-AVERAGED TOPOLOGY TO INSTANTANEOUS TOPOLOGY

This section focuses on the analogies between: the time-averaged patterns during the relaxation process following the pitch-up maneuver, as well as the patterns in absence of a maneuver; and the instantaneous patterns at termination of the pitching maneuver.

According to their classification, the time-averaged flow patterns on the surface of the stationary delta wing used in the present investigation, having $\Lambda = 50^\circ$ and $\alpha = 25^\circ$, fall into the general category of a spiral flow. That is, there is a spiral point (focus F of separation) on each

half of the wing, and unsteady shedding of vortices occurs from the foci F . At $\alpha = 15^\circ$, the pattern of topology along the surface of the wing was undefined, and above the surface of the wing, bursting of the leading-edge vortex occurs. That is, a leading-edge vortex is present and its breakdown location is between the apex and the trailing-edge. The flow patterns above the wing at $\alpha = 5^\circ$ had the form of a bubble vortex. In this case, the free shear layer has rolled up but no concentrated vortex core is formed. The corresponding pattern of topology along the surface of the wing was undefined.

Time Averaged Patterns during Relaxation Process. Figure G13 shows time-averaged patterns of streamline topology taken over the relaxation process for different pitch rates. It can be seen that the topology is very similar for all cases. The major critical points are as follows. An unstable focus of attachment F^+ exists near the apex of the wing, an upstream-oriented negative bifurcation line BL^- appears inboard of the leading-edge, and a saddle point S occurs near the intersection of the leading- and trailing-edges. Slight deviations of these patterns of Figure G13 are due to the fact that the time delay to occurrence of the first universal state is very sensitive to the pitch rate, while the delay between subsequent states is nearly independent of pitch rate. A remarkable observation is that these patterns closely resemble the instantaneous patterns of streamline topology in universal state 3, as shown in Figure G4. Thus, it can be stated that universal state 3 represents the time-averaged history of the flow relaxation due to a pitching delta wing. It should be noted that the case of $\dot{\alpha} C / U_\infty = 0.4$ is not given in Figure G13, due to insufficient image capture time.

Patterns during Relaxation in Comparison with Patterns at Lower Angles of Attack. Figure G14 shows, in the left column, instantaneous patterns of streamline topology as a function of normalized time t^* during relaxation for a pitch rate of $\dot{\alpha} C / U_\infty = 0.2$ and, in the right column, time-averaged patterns of streamline topology along a stationary wing at different values of angle-of-attack.

For the case of the stationary wing, the time-averaged streamline topology at an angle-of-attack $\alpha = 5^\circ$ shows a well-defined pair of positive and negative bifurcation lines BL^+ and BL^- , representative of attachment and separation respectively. This structure is the footprint of the leading-edge vortex on the wing surface. At $\alpha = 15^\circ$ of the stationary wing, a well-defined node N_1 of attachment is evident close to apex, a saddle point S_1 exists close to the intersection of the leading- and trailing-edges, a pattern of diverging streamlines A originating from the apex is present near the mid-chord, and two negative bifurcation lines BL_A^- and BL_B^- occur along the leading-edge. This combination is representative of a two dimensional separation zone along the leading-edge, and a reattachment zone near the mid-chord with a large-scale recirculation zone along the surface of the wing. The node N_2 and the saddle point S_2 represent small-scale instabilities in the flow field. At 25° , a large-scale swirl pattern with a well-defined center (focus F of separation) is evident, which indicates three-dimensional separation from the wing surface and existence of a stalled region. The negative bifurcation line BL^- along the leading-edge is representative of two-dimensional separation. There is also a saddle point S at approximately the same location as at 15° .

For the case of the maneuvering wing shown in the left column of images of Figure G14, the patterns of streamline topology in the image at $t^* = 0$, i.e., at termination of maneuver, shows a well-defined negative bifurcation line BL^- along the leading-edge, which is representative of separation. In addition, there is a positive bifurcation line-like pattern A originating from the apex of the wing, representative of reattachment. The saddle point S indicates a small-scale instability. The patterns of streamline topology at $t^* = 4.33$ indicate a well-defined node N of attachment close to the apex, a saddle point S_l close to the intersection of leading- and trailing-edges, and two negative bifurcation lines BL^- along the leading-edge, designated with subscripts A and B . The focus F and the saddle point S_2 represent small-scale instabilities. The patterns of streamline topology of image at $t^* = 13.65$, i.e., at a time close to completion of the relaxation process, shows a large-scale swirl pattern with a well-defined center (focus F of separation), a negative bifurcation line BL^- along the leading-edge close to apex, and a saddle point S close to the intersection of leading- and trailing-edges.

A direct comparison of the images corresponding to the maneuvering wing with images of the stationary wing indicates similarities in the streamline topology between two cases, in which they exhibit common topological features and critical points. For example, the streamline topology of the stationary wing at $\alpha = 5^\circ$ is very similar to that of the maneuvering wing at $t^* = 0$. They both show a pair of negative and positive bifurcation lines: BL_A^- and BL_B^- along the stationary wing image at $\alpha = 5^\circ$, and BL^- and A (positive bifurcation line-like pattern) for the maneuvering wing at $t^* = 0$. Likewise, the aforementioned patterns for the stationary wing at $\alpha = 15^\circ$ are very similar to those for the maneuvering wing at $t^* = 4.33$. Their common topological features are a well-defined node of attachment close to apex, N_l in the stationary wing at $\alpha = 15^\circ$, and N for the maneuvering wing at $t^* = 4.33$, a saddle point S_l close to the intersection of leading- and trailing-edges, and two negative bifurcation lines BL_A^- and BL_B^- . Also, the aforementioned patterns for the stationary wing at $\alpha = 25^\circ$ are very similar to those for the maneuvering wing at $t^* = 13.65$. They both include a focus F of separation, a negative bifurcation line BL^- along the leading-edge close to apex, and a saddle point S close to the intersection of leading- and trailing-edges.

In summary, the foregoing comparisons demonstrate that the near-surface topological patterns observed during the early stages of the relaxation process (following termination of a maneuver) are similar in form to the near-surface patterns on the corresponding stationary wing at smaller angles-of-attack. This similarity of patterns is due to the time lag of the flow structure following cessation of the wing maneuver.

6. CONCLUSIONS

The time evolution of the near-surface flow patterns is characterized along a delta wing of moderate sweep angle using a technique of high image density single camera particle image velocimetry. Emphasis is on the patterns following completion of a linear ramp-like pitching motion, for a wide range of pitch rate. Patterns of velocity vectors and streamline topology, including critical points and topological features allow definition of the effect of pitch rate. Dye visualization provided complementary insight. Similar investigations were performed for the

flow patterns on a stationary delta wing as function of static variation of angle-of-attack. The principal findings are as follows:

1. Five different universal states of the near-surface topology can be defined during the relaxation process that follows termination of the pitching motion. Such states can be identified over an eightfold range of pitch rate. These states involve distinct patterns that can be defined in terms of topological features and define the time evolution of flow structure on a delta wing of moderate sweep angle.
2. The near-surface patterns at the instant corresponding to termination of the maneuver are a strong function of the magnitude of pitch rate and show substantial variation. Remarkably, despite the large differences in the state of the flow at the beginning of the relaxation process, the near-surface patterns evolve in the aforementioned sequence of universal states. That is, irrespective of the severity of the flow distortion at the end of the pitching maneuver, the relaxation of the flow involves the same sequence of universal states.
3. During evolution of flow following termination of the pitching maneuver, it is demonstrated that the time delay to occurrence of the first state is very sensitive to the magnitude of the pitch rate. The delay between subsequent states is, however, nearly independent of pitch rate. The time delay to occurrence of the first universal state is not constant, but can be estimated for variations of pitch rate with a simple curve fit. The time delay between the occurrence of the first universal state and of the fifth universal state is, however, nearly constant for all pitch rates. Therefore, a stall time can be defined as the sum of: the time between termination of maneuver and occurrence of the first universal state, which is a function of pitch rate, and the time between the occurrence of the first universal state and occurrence of the fifth universal state, which is independent of pitch rate. This approach provides an indication of the onset of three-dimensional separation and stall along the surface of the wing for a wide range of pitch rate.
4. The universal states are defined in terms of near-surface topology using critical points. This approach allows identification of regions of separation and reattachment, as well as centers of large-scale and small-scale recirculation zones along the surface of the wing. During the relaxation process, these critical points undergo alterations, or, in some cases, transformation to another type of critical point. This time evolution of the patterns of critical points is complemented by dye visualization of the flow pattern along the wing, which defines the evolution of the leading-edge vortex and the onset of separation and stall. Furthermore, it is demonstrated that there exists a critical universal state, which marks an abrupt transformation between two distinctly different states of the near-surface pattern of critical points.
5. Time-averaged patterns of the near-surface topology were evaluated at various values of angle-of-attack of the corresponding stationary wing. It is demonstrated that the sequence of the topological patterns observed during the early stages of the relaxation process is similar to the patterns on the stationary wing at successively smaller angles-of-attack.

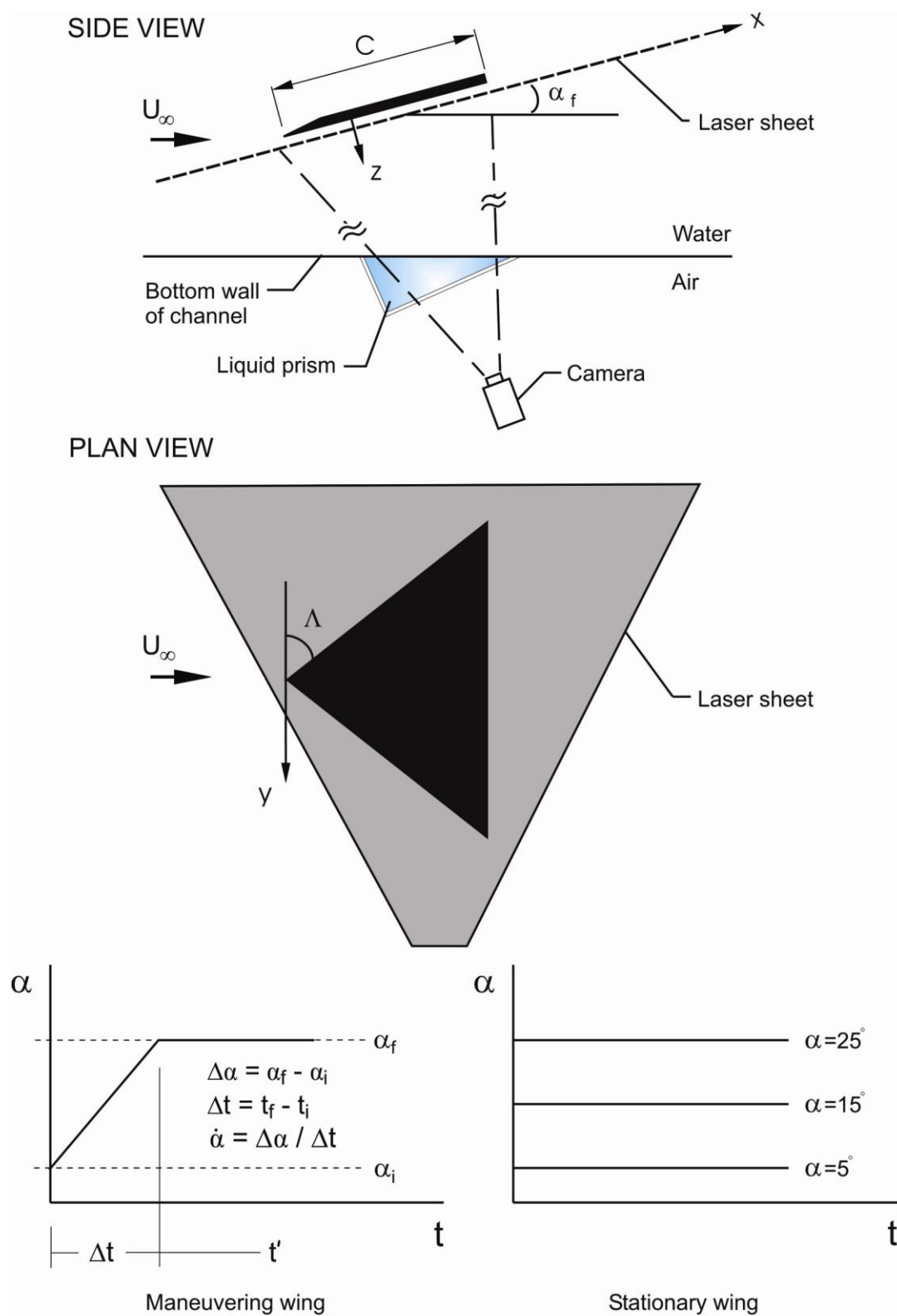


Figure G1: Overview of delta wing and laser sheet orientation for quantitative imaging.

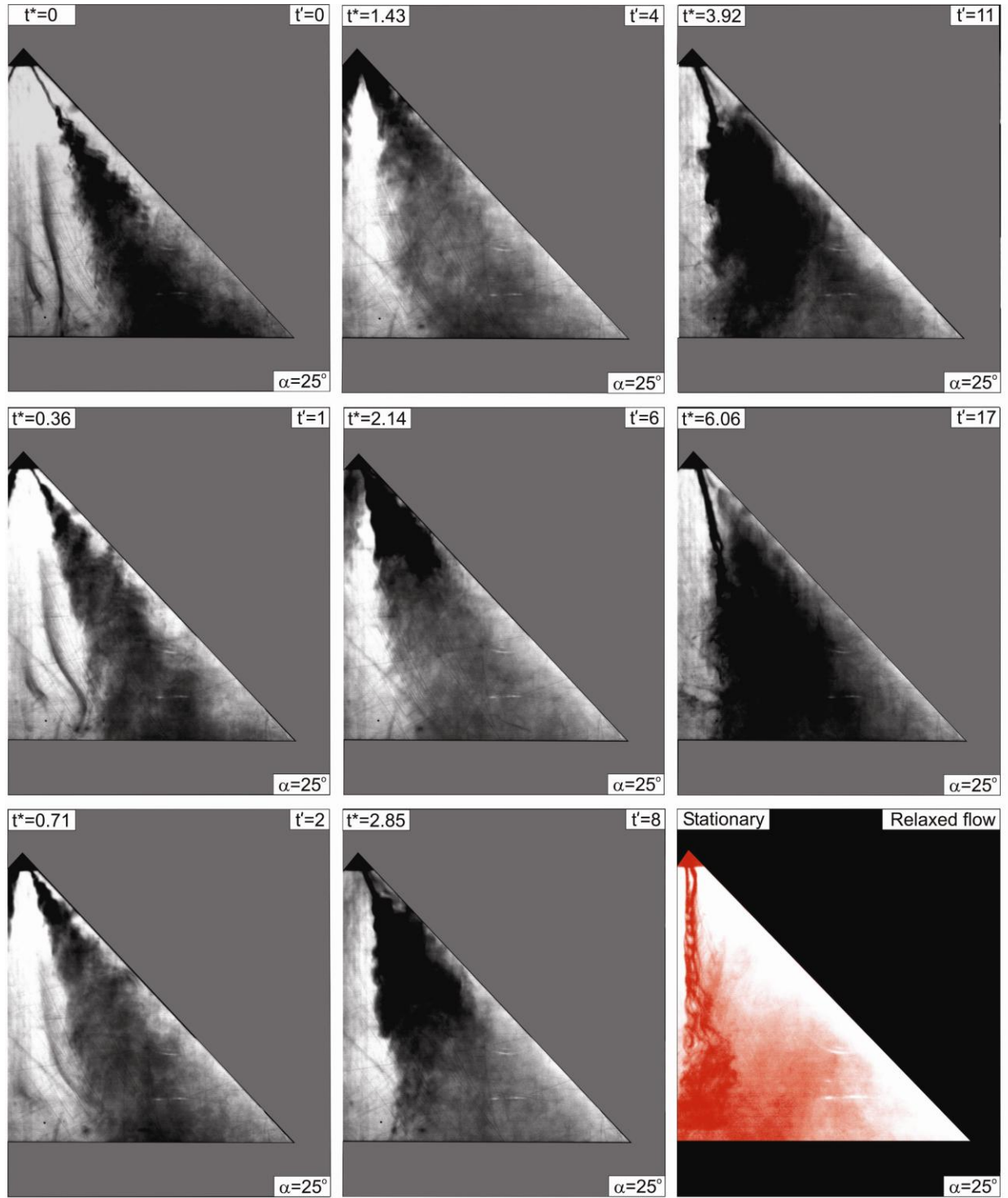


Figure G2: Dye visualization of relaxation process after cessation of maneuver, where t' is the actual time in seconds and $t^* = t'U_\infty/C$ is the dimensionless time after attainment of final angle-of-attack α_f . The pitch-up rate is $\dot{\alpha}C/U_\infty = 0.1$. (From Yavuz, 2006).

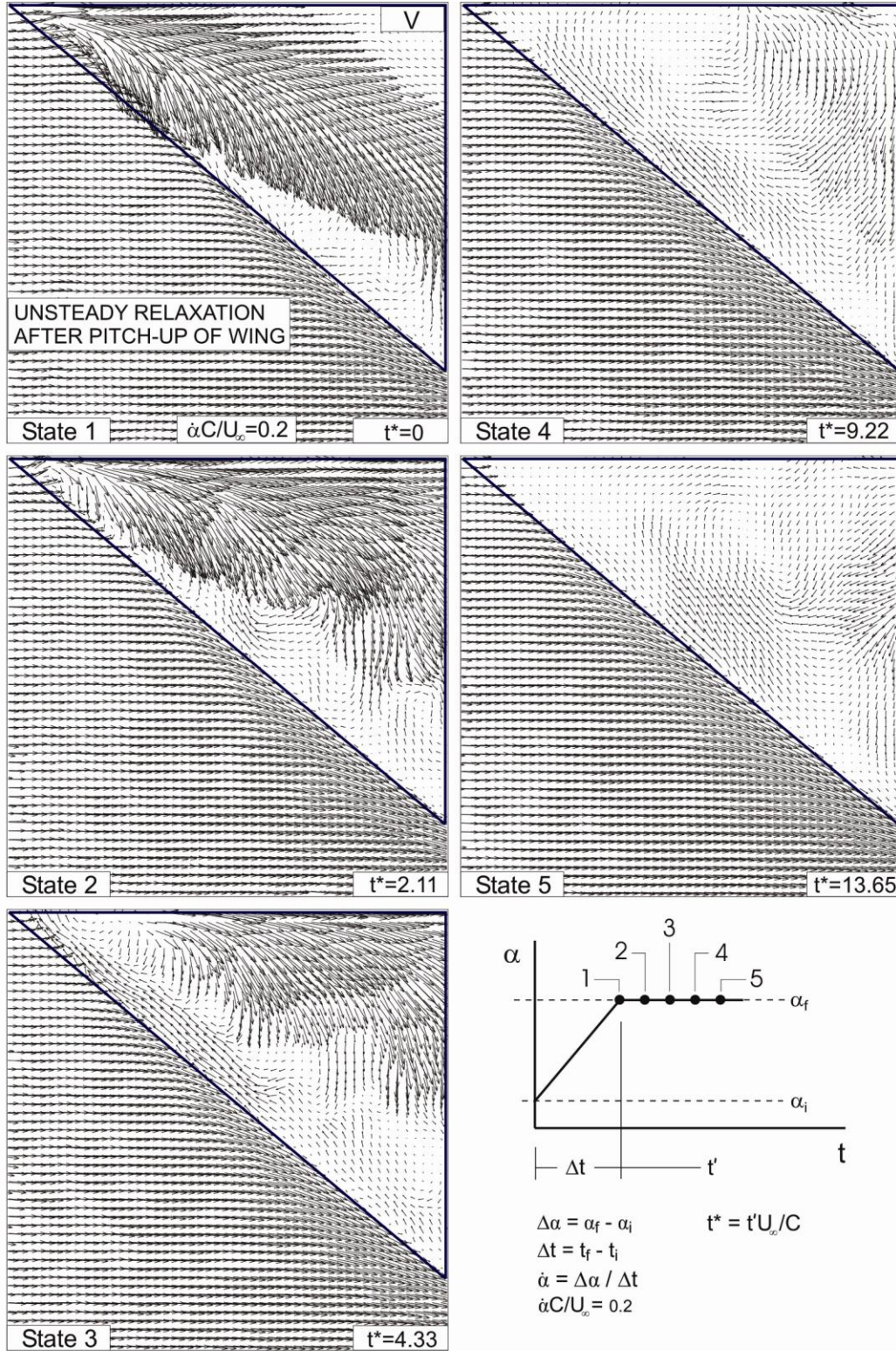


Figure G3: Patterns of instantaneous velocity vectors V during relaxation process after cessation of maneuver as a function of non-dimensional time t^* . The pitch-up rate is $\dot{\alpha}C/U_\infty = 0.2$.

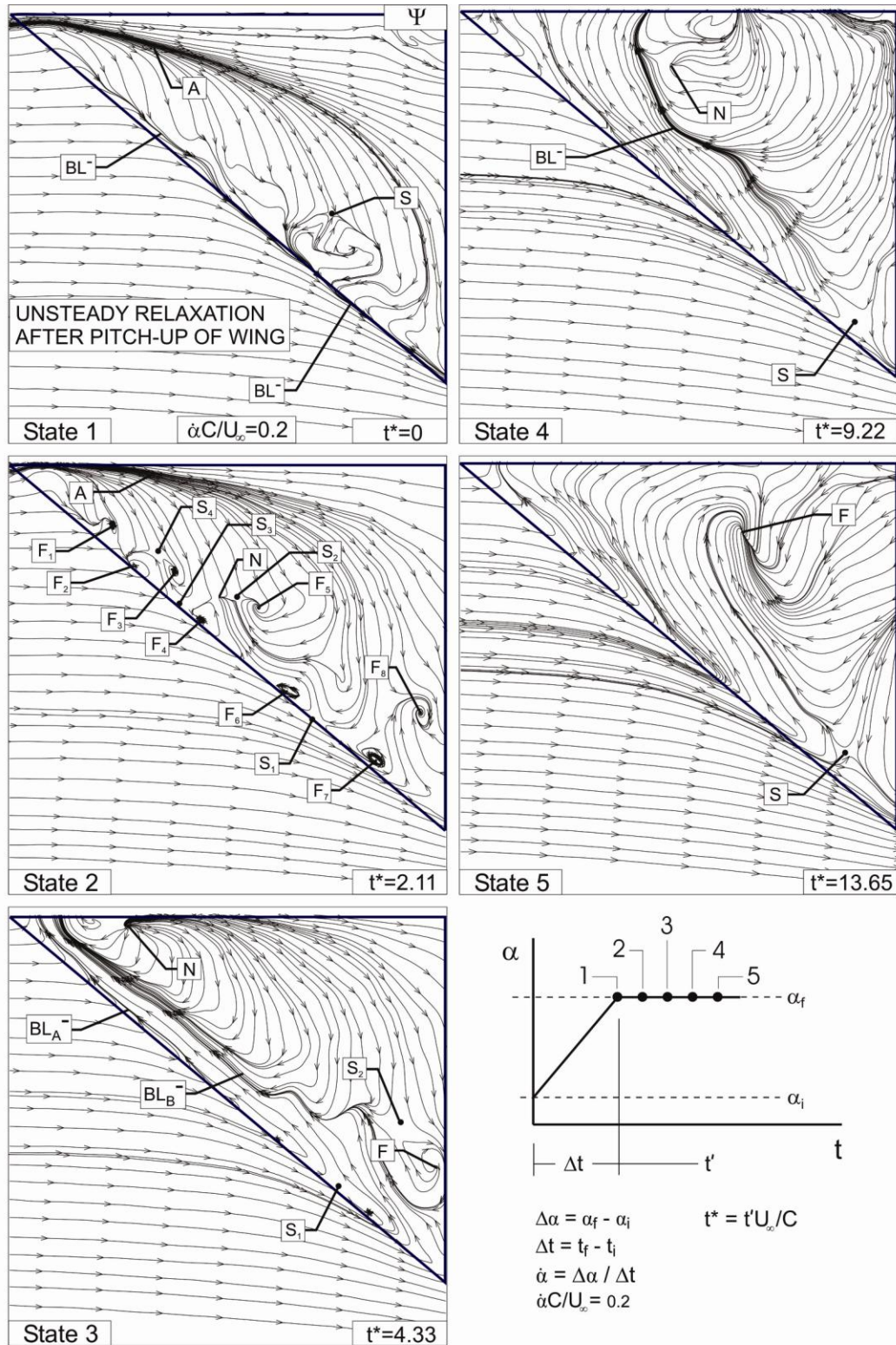


Figure G4: Patterns of instantaneous streamline topology Ψ during relaxation process after cessation of maneuver as a function of non-dimensional time t^* . The pitch-up rate is $\dot{\alpha}C/U_\infty = 0.2$.

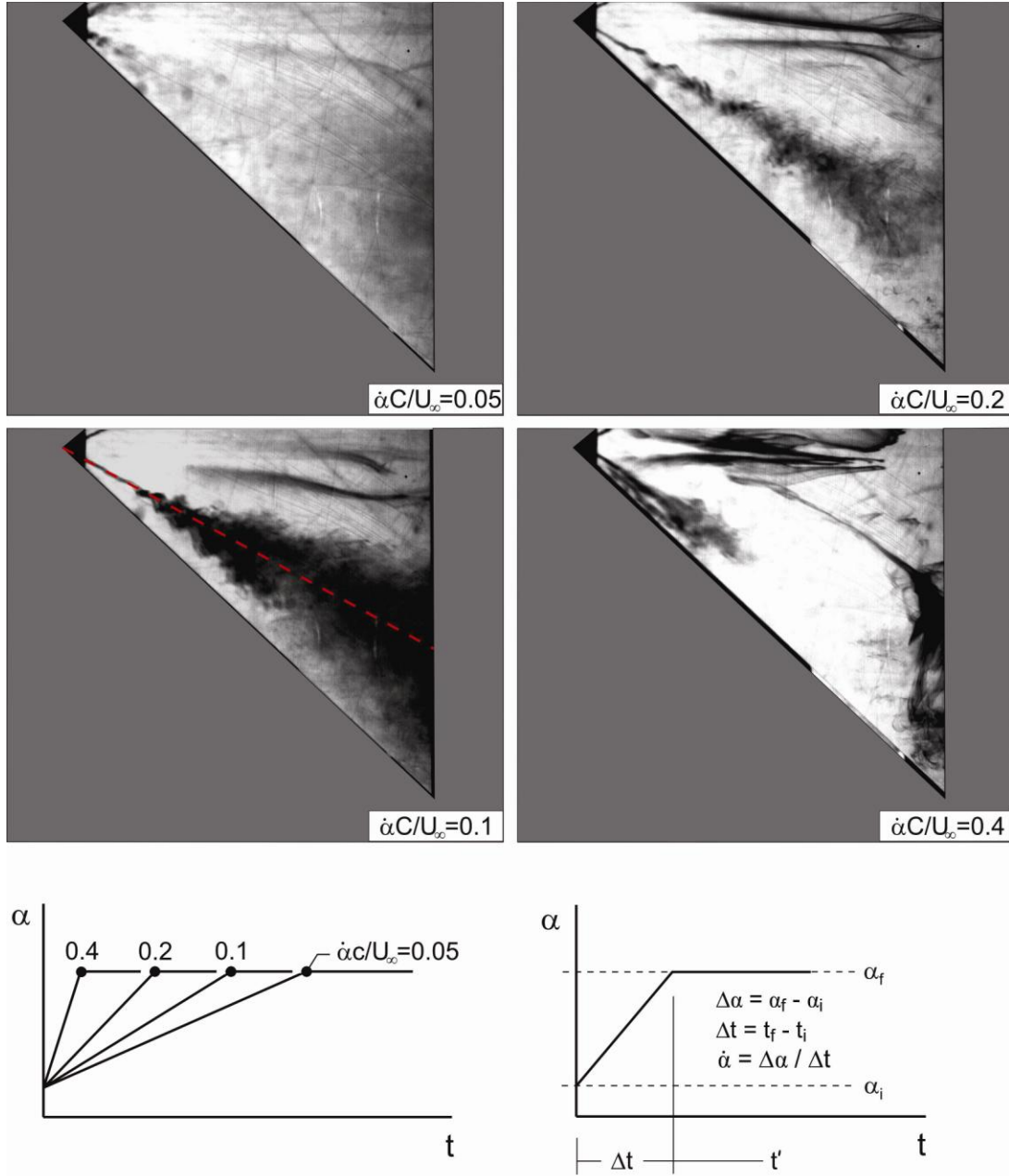


Figure G5: Dye patterns at cessation of maneuver for different pitch rates $\dot{\alpha}C/U_\infty$ (From Yavuz, 2006). The path of the leading-edge vortex is indicated with red dashed line.

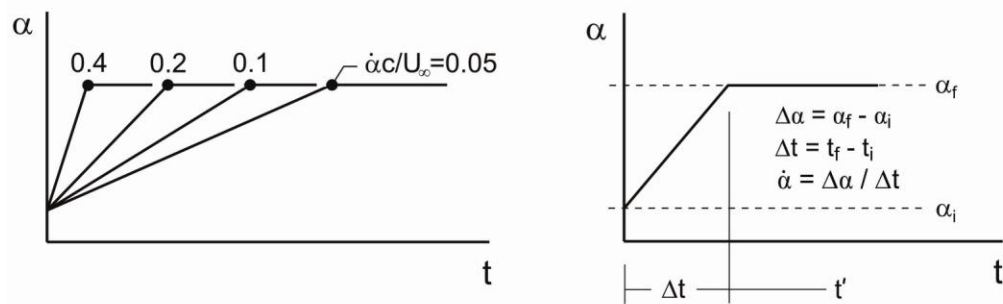
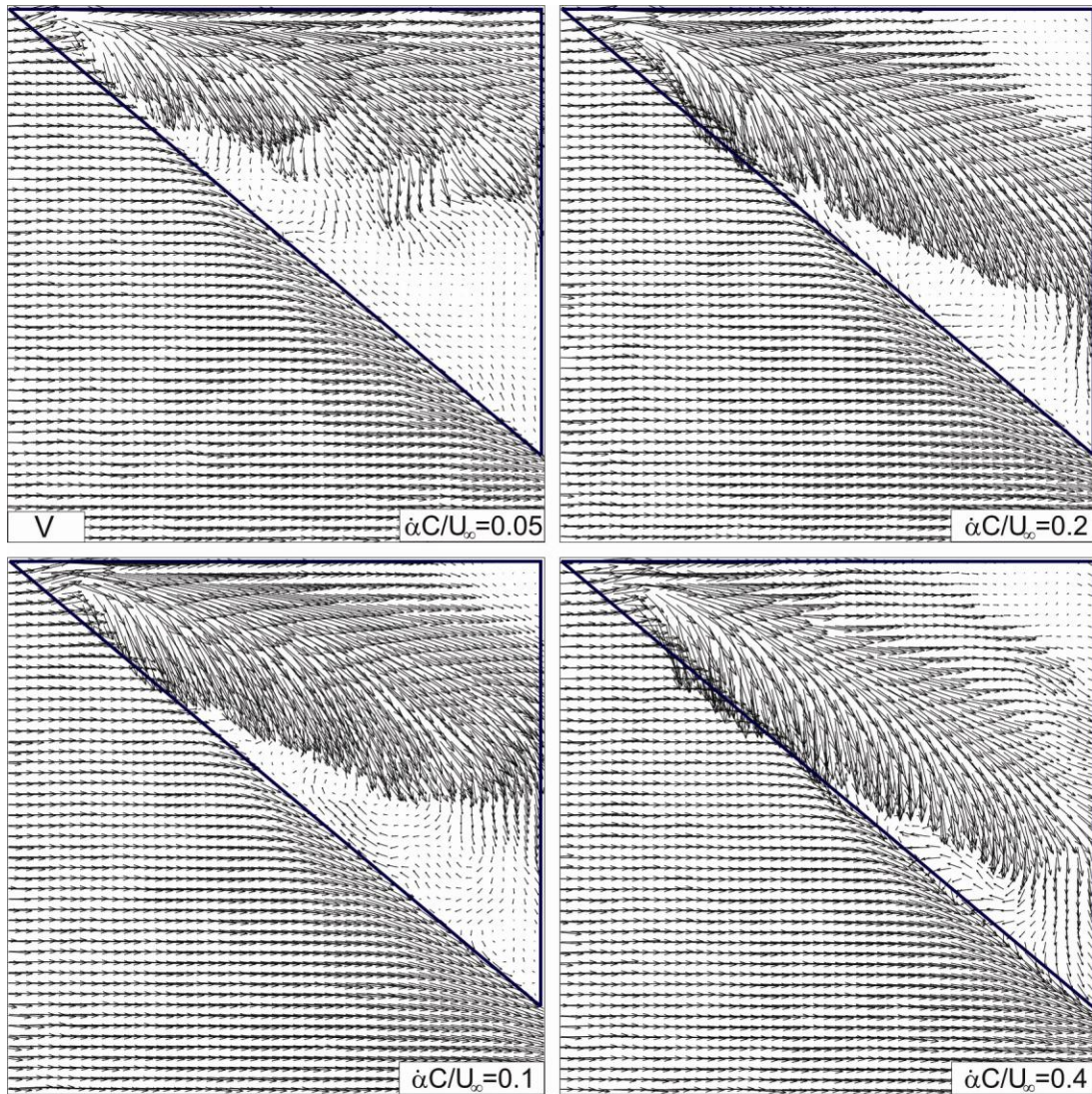


Figure G6: Patterns of instantaneous velocity vectors V at cessation of maneuver for different pitch rates $\dot{\alpha}C/U_\infty$.

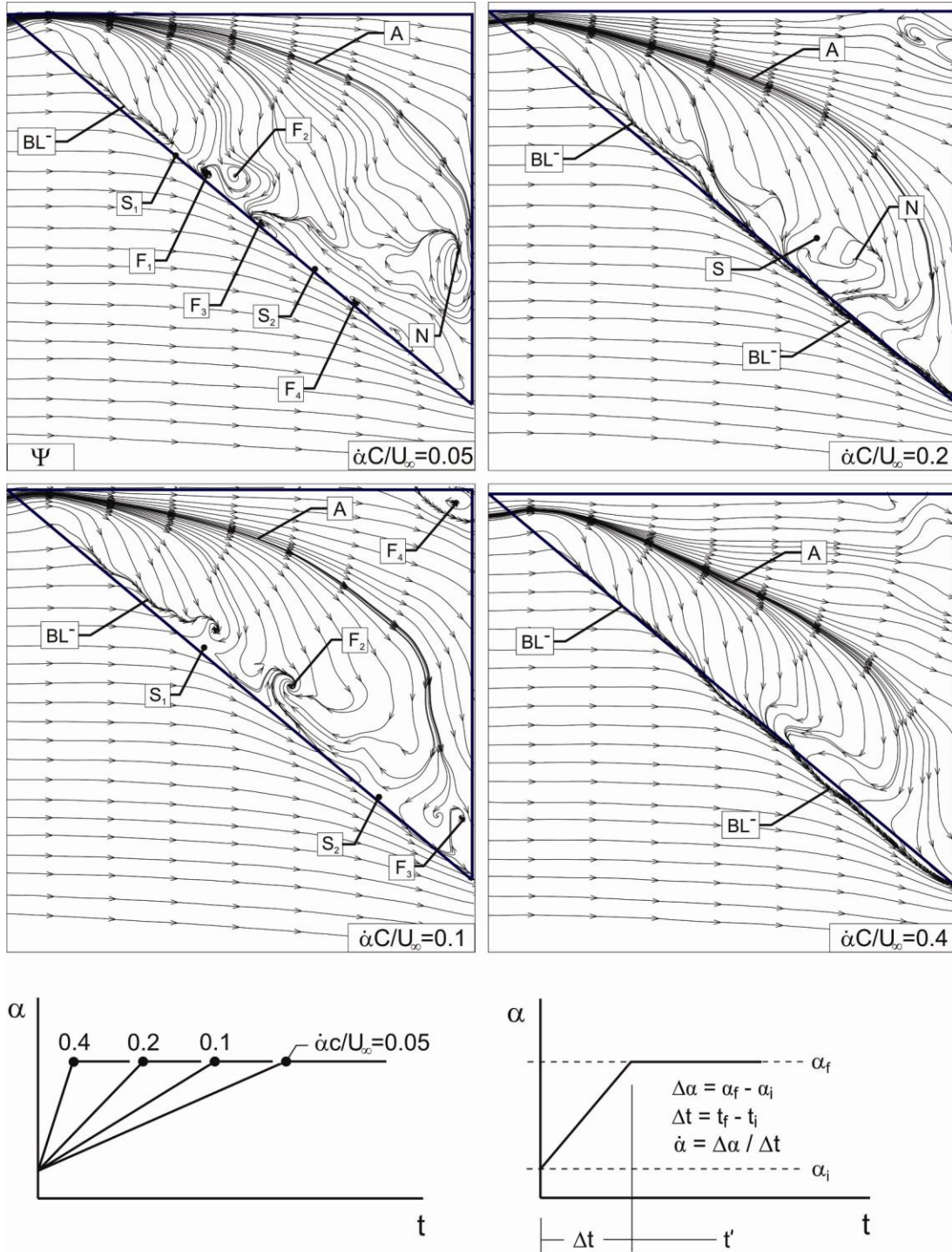


Figure G7: Patterns of instantaneous streamline topology Ψ at cessation of maneuver for different pitch rates $\dot{\alpha}C/U_\infty$.

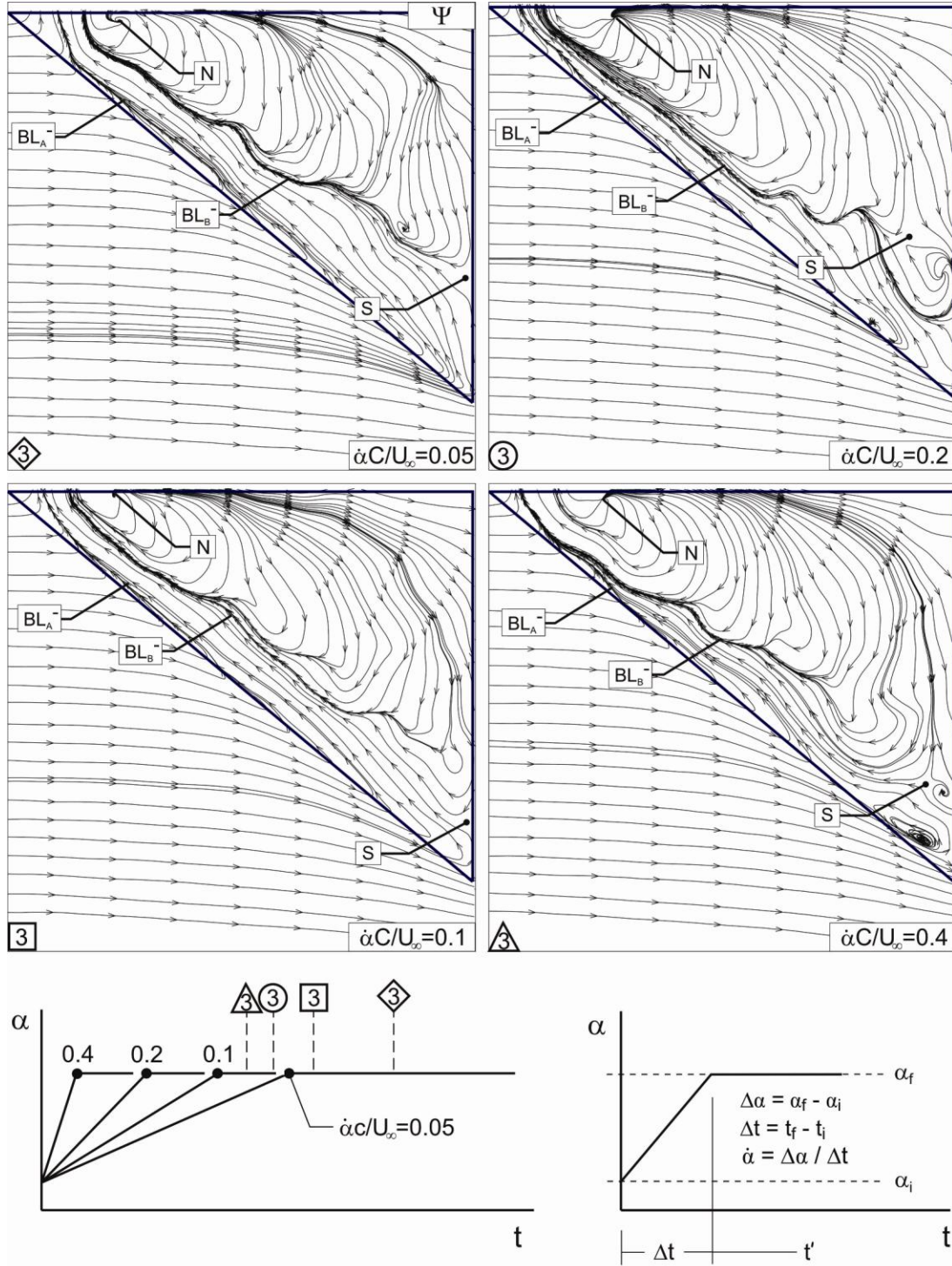


Figure G8: Patterns of instantaneous streamline topology Ψ at universal state 3 for different pitch rates $\dot{\alpha}C/U_\infty$.

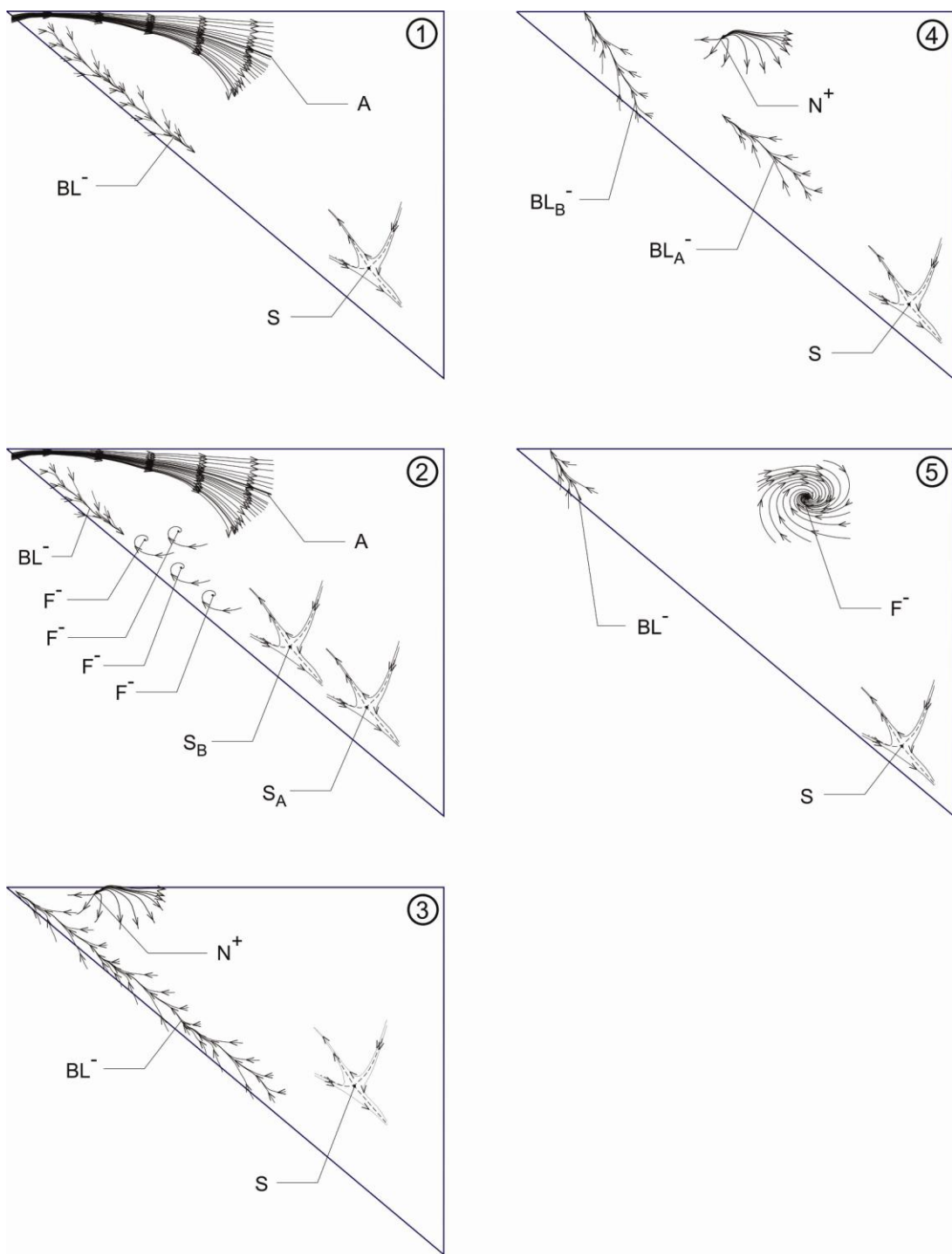


Figure G9: Definition of universal states during relaxation process, in terms of critical points and topological features.

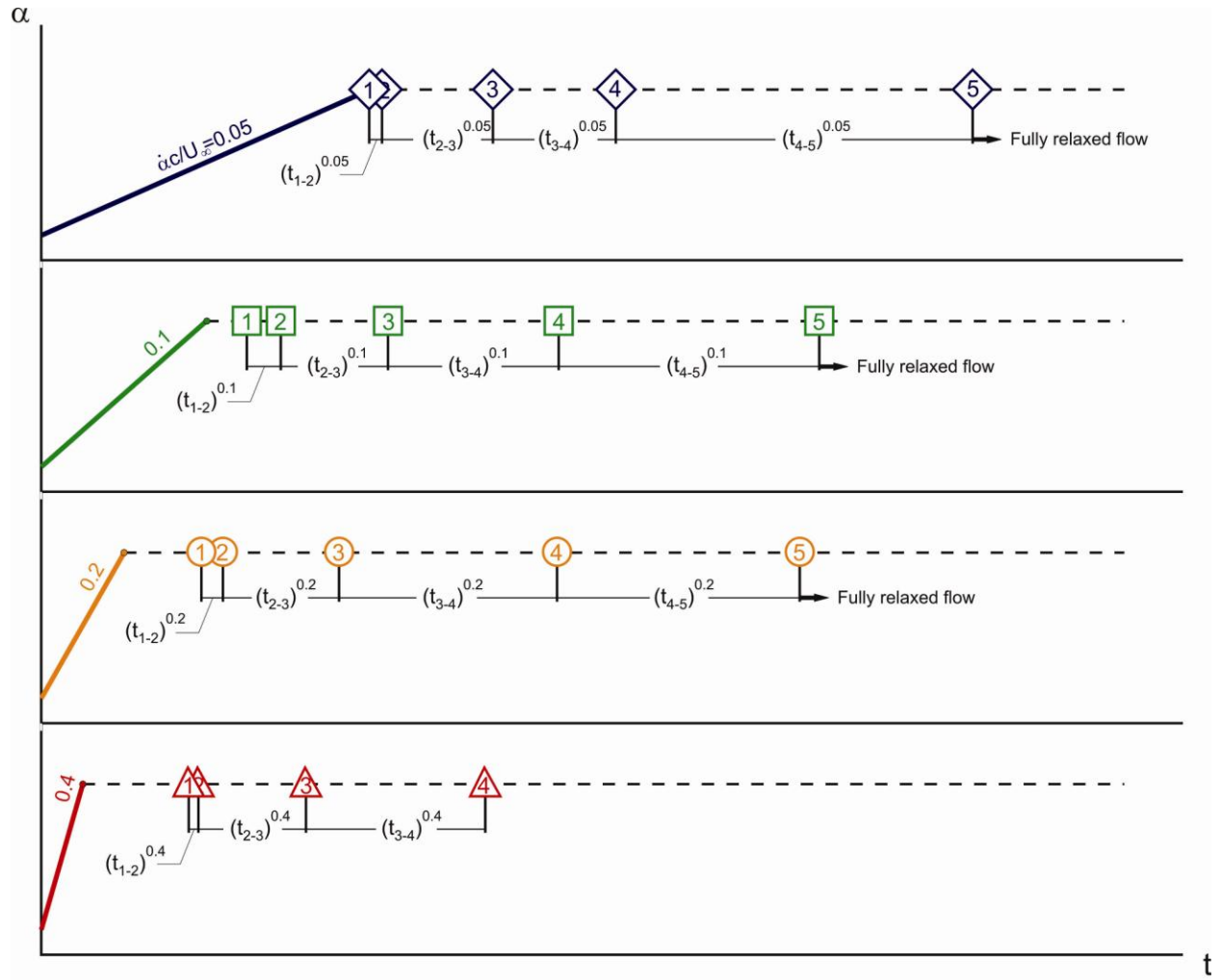


Figure G10: Times of occurrence of universal states during relaxation for different pitch rates $\dot{\alpha}C/U_\infty$.

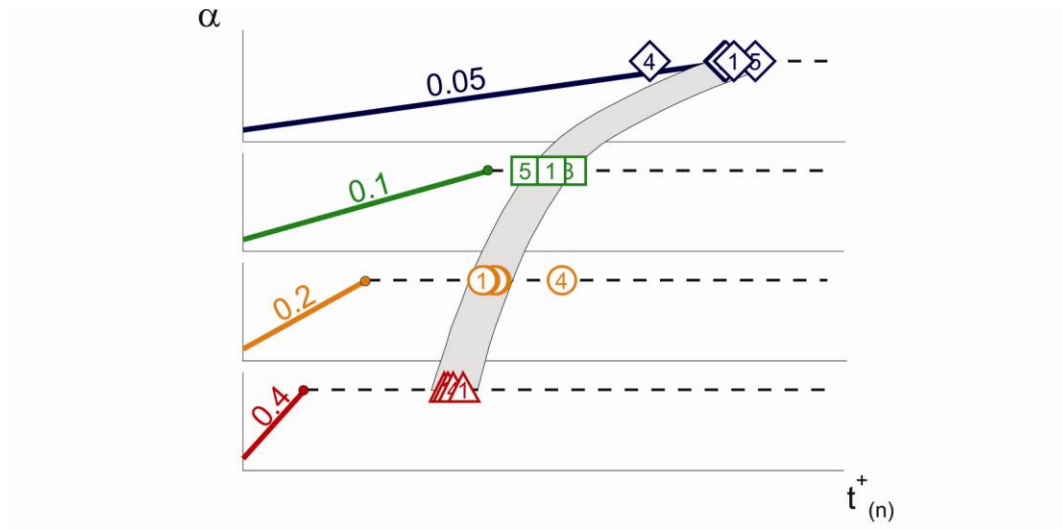


Figure G11: Times for occurrence of universal states during relaxation for different values of pitch rate $\alpha C/U_\infty$. The expression for the time axis is defined in equation (3.2).

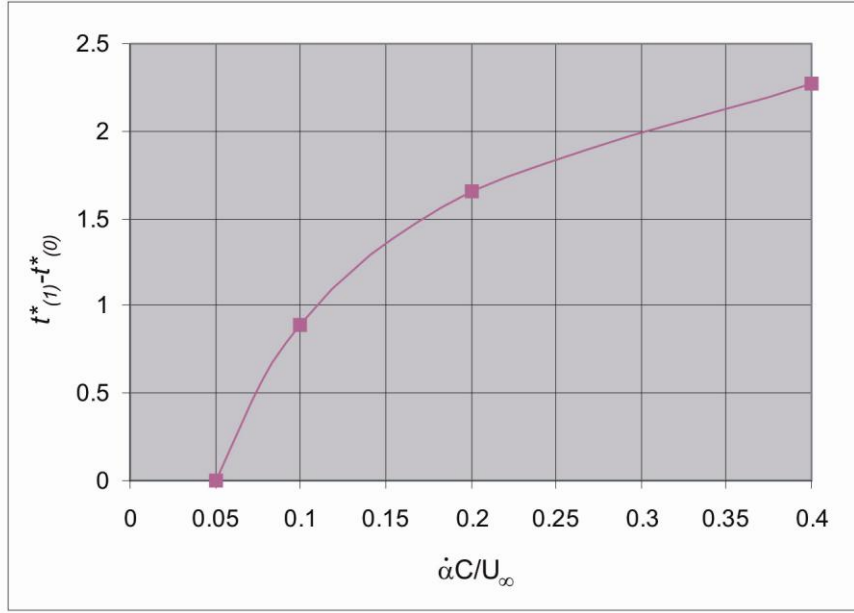


Figure G12: The time elapsed between termination of the pitch-up maneuver and the occurrence of universal state 1 as a function of pitch rate $\dot{\alpha}C/U_{\infty}$. Time t^* is defined as $t'U_{\infty}/C$.

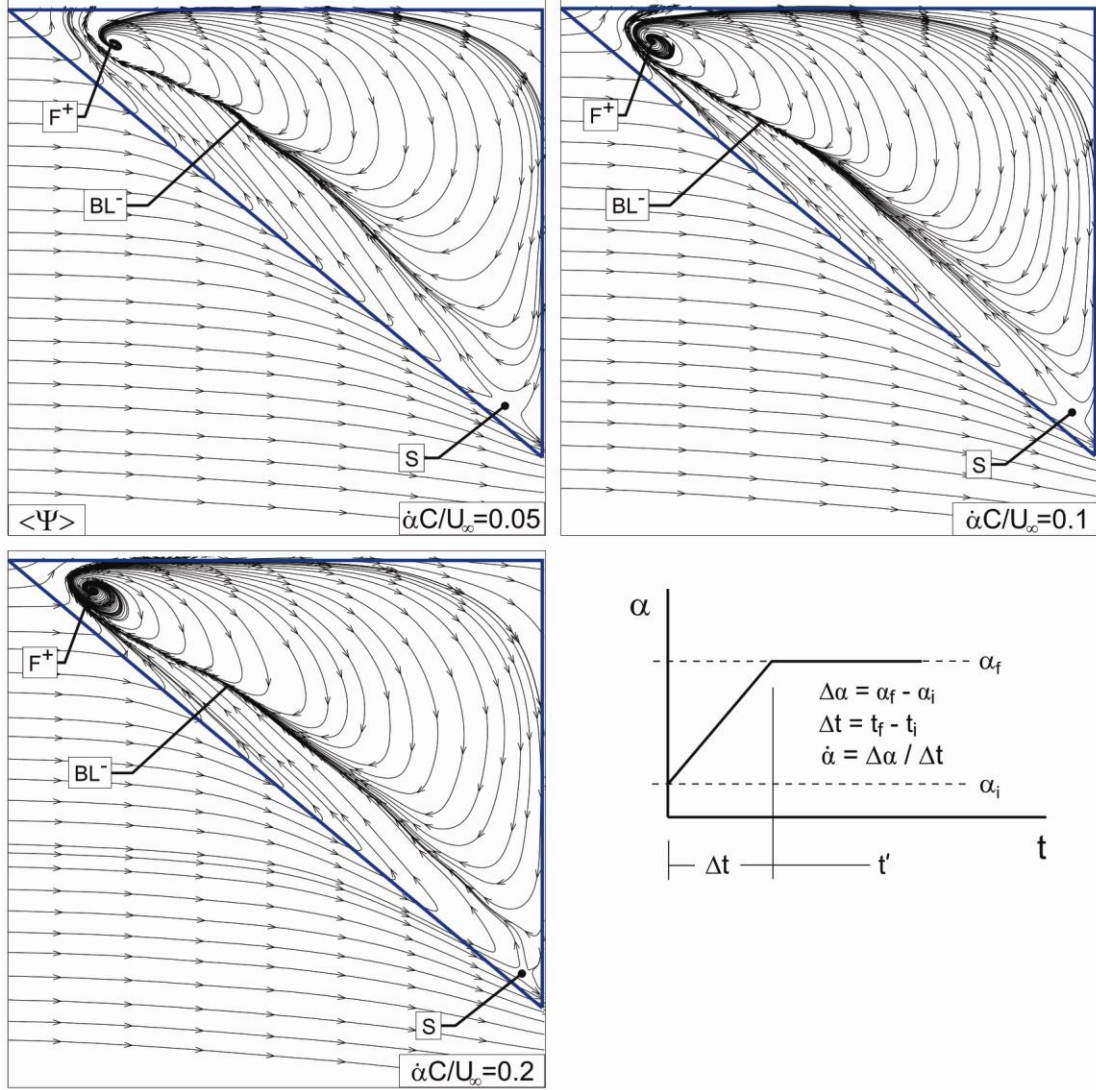


Figure G13: Time-averaged streamline topology $\langle \Psi \rangle$ taken over the interval corresponding to the relaxation process for different pitch rates $\dot{\alpha}C/U_\infty$.

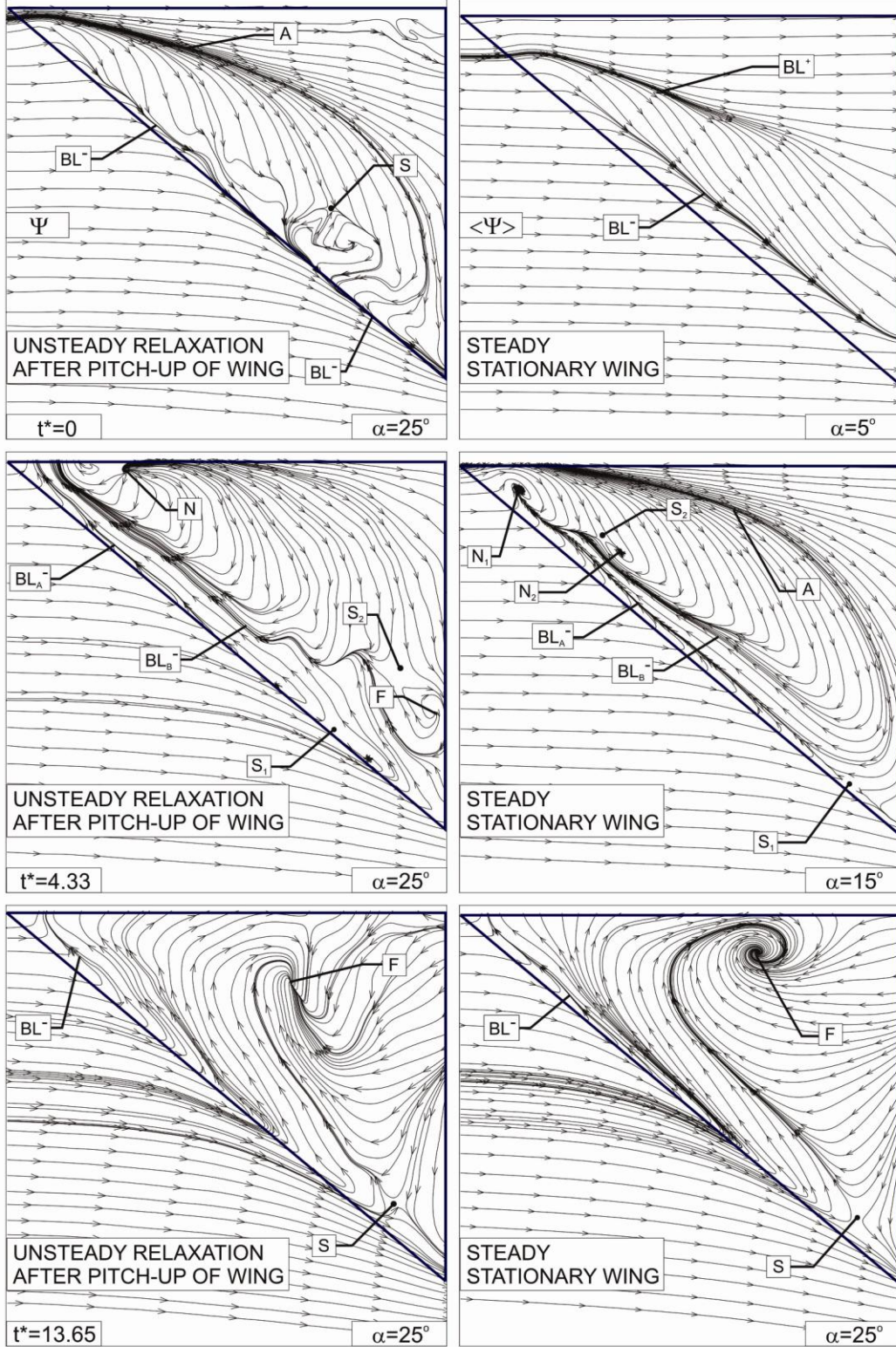


Figure G14: Comparison of instantaneous patterns of streamline topology Ψ as a function of t^* during relaxation process for a pitch rate of $\dot{\alpha}C/U_\infty=0.2$, and time-averaged patterns of streamline topology $\langle \Psi \rangle$ along a stationary wing at different values of angle-of-attack α .